Research supported by NSF under
grant #ATM-0071371, as well as a
graduate fellowship from the
American Meteorological Society.

AIRFLOW AND PRECIPITATION STRUCTURE OF TWO LEADING STRATIFORM MESOSCALE CONVECTIVE SYSTEMS

by

Crystalyne R. Pettet

Richard H. Johnson, P.I.

Colorado State University

DEPARTMENT OF ATMOSPHERIC SCIENCE

PAPER NO. 712

AIRFLOW AND PRECIPITATION STRUCTURE OF TWO LEADING STRATIFORM MESOSCALE CONVECTIVE SYSTEMS

by

Crystalyne R. Pettet

Department of Atmospheric Science
Colorado State University
Fort Collins, CO 80523-1371

Fall 2001

Atmospheric Science Paper # 712

ABSTRACT

AIRFLOW AND PRECIPITATION STRUCTURE OF TWO LEADING STRATIFORM MESOSCALE CONVECTIVE SYSTEMS

An analysis of the airflow and precipitation structure of two leading stratiform (LS) mesoscale convective systems is presented. LS systems are defined as linear MCSs that consist of a convective line with leading stratiform rain. Case studies of LS systems on 30 April 2000 and 7 May 1997 were conducted using the available operational datasets. Several of the features observed, though not all, appear as a mirror image of those seen in trailing stratiform (TS) mesoscale convective systems. Their horizontal reflectivity structure has similar aspects, with convective cells which are sometimes elongated and canted with respect to the convective line, a transition zone of lower reflectivity, and an area of enhanced stratiform rain. Cold pools are situated beneath the convective line. The 30 April case shows a leading mesolow that resembles a TS wake low, but its propagation characteristics (and presumably dynamics) differ. A descending leading inflow jet, the counterpart of a rear inflow jet in a TS system, can be detected in both cases underneath a layer of strong ascending rear-to-front flow aloft.

A few features of these LS systems are distinctive from TSs. Cells in the convective line appear to be more discontinuous, and are elongated more than those of a TS. Rear-feeding from an elevated θ_e maximum behind the system is an exclusive feature of these LSs, since TSs are typically fed from the boundary layer. Unlike the rear inflow jet in TS

systems, neither case shows a reversal in the leading inflow jet as it descends to low levels near the convective line. Both cases exhibit front-to-rear surface flow throughout the LS systems.

Finally, a schematic diagram is presented that illustrates the structure observed in the two cases, based heavily on a Doppler radar analysis of 7 May 1997.

Crystalyne R. Pettet
Department of Atmospheric Science
Colorado State University
Fort Collins, Colorado 80523-1371
Fall 2001

ACKNOWLEDGEMENTS

The research reported here was supported by the National Science Foundation under Grant ATM-0071371 as well as a one year graduate fellowship from the American Meteorological Society and Silicon Graphics, Inc.

National radar composite data were provided by the Global Hydrology Resource Center at the Global Hydrology and Climate Center, Huntsville, Alabama, satellite images by the Cooperative Institute for Research in the Atmosphere, and rawinsonde soundings by the University of Wyoming. The National Climatic Data Center provided data from the wind profiler network, NEXRAD Level II WSR-88D radar, surface stations, and the NCEP analysis charts. Eta Data Assimilation System data was provided by NOAA's Air Resources Laboratory.

I would like to thank Drs. J. Ramirez, S. Rutledge, and R. Johnson for serving as my committee members and carefully reviewing this manuscript. I especially would like to thank Dr. Johnson for serving as my advisor. His ability to mentor students, providing an optimal balance of freedom and guidance, is unsurpassed. I would like to thank my officemates, M. Parker and J. Knievel, for providing research advice, essential computer programs, and entertaining conversation. A. Williams helped me with radar questions. R. Taft and P. Ciesielski provided solutions to computer difficulties as well as programming help. G. Cordova helped with supplies, occasional travel arrangements, as well as scheduling my defense. Lastly, I would like to thank my husband, Kent, for endless support throughout the research process and for keeping life interesting.

CONTENTS

FIGURES

TABLES

Chapter 1

INTRODUCTION

The term mesoscale convective system, or MCS, was coined by Zipser (1982) to refer to "cloud and precipitation systems, together with their associated circulation systems, which include a group of cumulonimbus clouds during most of the lifetime of the system." These organized storms account for 30 to 70 percent of warm season rainfall in the central U.S. (Fritsch et al. 1986), making them of great interest to forecasters as well as farmers. MCSs can bring with them welcome rain, lightning, severe weather, or flash floods. The mystery of these storms and the desire to understand and predict them better has resulted in a great deal of study of these systems by the research community.

Zipser's definition of MCS has been modified slightly in several studies in the past 19 years. In 2000, the AMS Glossary of Meteorology defines MCS in this way: "a cloud system that occurs in connection with an ensemble of thunderstorms and produces a contiguous precipitation area on the order of 100 km or more in horizontal scale in at least one direction". This is the definition that will be used for the remainder of this study.

MCSs have lifespans of hours to days. Their organized, multicellular nature allows them to persist long past the growth and decay of an individual convective cloud by generating new cells on organized outflow boundaries and keeping much of the system from entraining dry environmental air. They modify their environment, principally through gravity waves, and often create their own forcing mechanism in the form of a cold pool. They

can also modify the height field in their vicinity: mesohighs and wake lows at the surface, mesolows in the midtroposphere, and mesohighs aloft. While most MCSs have common elements, individual systems can look very different from one another, so many classification schemes abound.

The category MCS contains many subsets, e.g., mesoscale convective complexes (MCCs), bow echoes, squall lines, and for the purpose of this study, "linear MCSs." MCCs are defined by the size of their cloud shield on satellite. To be defined as an MCC, a system must have a cloud shield that extends over 100,000 km^2 for at least six hours (Maddox 1980). Bow echoes are 60–100 km long curved lines of cells which can cause strong, damaging winds (Fujita 1978). They can be independent or part of a squall line. Squall lines, once considered to be lines of convection only *well ahead* of fronts (cf. Huschke 1959), were generalized by Bluestein and Jain (1985) to mean bands of precipitation that are at least partly convective. With this new definition, precipitation bands that occur along a front or near one are included in the squall line category. Linear MCSs are considered to be any MCS containing a convective line with contiguous or nearly contiguous chain of convective echoes sharing a nearly common leading edge and moving approximately in tandem.

Linear MCSs have been studied for quite some time. The typical linear MCS has a leading convective line and a trailing stratiform region (Houze et al. 1990), hereafter referred to as a TS MCS. The structure of this type of system has been the subject of numerous studies (Smull and Houze 1985; Rutledge and Houze 1987; Johnson and Hamilton 1988; Rotunno et al. 1988; Houze et al. 1989; Lafore and Moncrieff 1989; Houze et al. 1990; Gallus and Johnson 1992; etc.). Other organizational modes of linear MCSs exist but have received little attention, previously considered to be anomalous. Studies by Schiesser et al. (1995) and Parker and Johnson (2000), however, show that other modes of linear MCS organization occur more frequently than previously thought. The purpose of this study is to determine the structure of a previously undocumented type of linear MCS–a convective line with leading stratiform rain, hereafter referred to as an LS MCS. Parker and Johnson

(2000) presented a case study of an LS system, but due to inadequate data, the airflow and precipitation structure within the system could not be determined. This study will investigate just those aspects of LS MCSs. Moreover, there is evidence to suggest that LS MCSs, because of their slow movement, may be implicated in flash floods (Johnson and Parker 2001). This possibility further emphasizes the importance of understanding more about the characteristics of LS MCSs.

This manuscript is organized in the following manner. Chapter 2 covers the background of previous research on linear MCSs and provides the motivation for the current study. Chapter 3 discusses the different datasets utilized for this study and the method used to analyze them. Chapters 4 and 5 provide case studies of specific LS systems. Chapter 6 synthesizes the results of these two case studies. Finally, Chapter 7 states conclusions drawn from this work and provides ideas for future research.

Chapter 2

BACKGROUND AND MOTIVATION

2.1. Background

Houze et al. (1990) described in detail the structure of a linear MCS with a leading convective line and a region of trailing stratiform rain, or a trailing stratiform (TS) MCS. Their climatological survey of MCSs within the vicinity of the Oklahoma City radar for six consecutive April-May-June periods documented several features, some of which had been noted previously in individual case studies. Houze et al. (1990) compiled these features to provide a comprehensive picture of this leading-line/trailing-stratiform structure. A schematic diagram of the structure of the TS system is shown in Fig. 2.1 (Houze et al. 1989).

Trailing stratiform MCSs are fed from the front with air that has not been modified by previous rain (Moncrieff 1992). This front inflow is enhanced by the development of a surface cold pool. The cold pool is formed by the evaporatively cooled air beneath the convective cells descending to the ground and spreading out, forming a mesohigh (Fig. 2.2b). The cold pool can advance ahead of the storm, helping to initiate new cells. According to Rotunno et al. (1988), or RKW, an equal balance between the strength of the cold pool and the low-level, line-perpendicular shear vector is optimal for the development of long-lived convection, producing a straight vertical updraft which maximizes vertical momentum. However, many TS systems are very long-lived yet exist in a "less than optimal shear" state. Lafore and Moncrieff (1989) suggested that baroclinic generation of vorticity in stratiform rain regions must also be considered to find the optimal state.

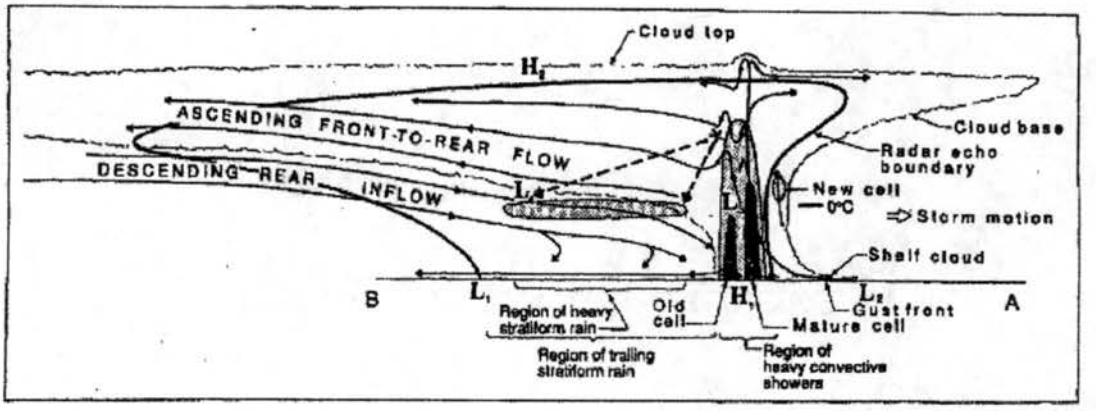

Figure 2.1: Vertical cross section oriented perpendicular to the convective line of a conceptual model of a TS MCS (Houze et al. 1989).

Trailing stratiform MCSs have a descending rear inflow jet (Smull and Houze 1987) that passes through the stratiform region and down to the surface, eventually reversing when it encounters the convective cells (Fig. 2.1). This rain-cooled air does not enter the updraft in the leading convective line, allowing the storm to continue to "feed" on warmer inflow from the front. At the surface beneath the stratiform rain a wake low is commonly observed. This wake low is caused by the rear inflow jet descending and hydrostatically reducing the surface pressure where the jet meets the surface, illustrated in Fig. 2.2a (Johnson and Hamilton 1988). In a linear context, the surface mesohigh/wake low couplet owes its existence to the gravity wave response to cooling in the stratiform region (Haertel and Johnson 2000).

There is a strong rising FTR flow behind the convective cells which carries hydrometeors to the rear of the storm (Fig. 2.1), forming the trailing stratiform rain (Smull and Houze 1985; Rutledge and Houze 1987). As the ice crystals grow they begin to fall and melt, forming a region of enhanced reflectivity just below the freezing level known as the bright band (Houze et al. 1989). Between the bright band and the convective cells is an area of lower reflectivity known as the transition zone (Houze et al. 1989). Also apparent on radar is a small leading anvil, created by the divergence of air at the top of the updraft column.

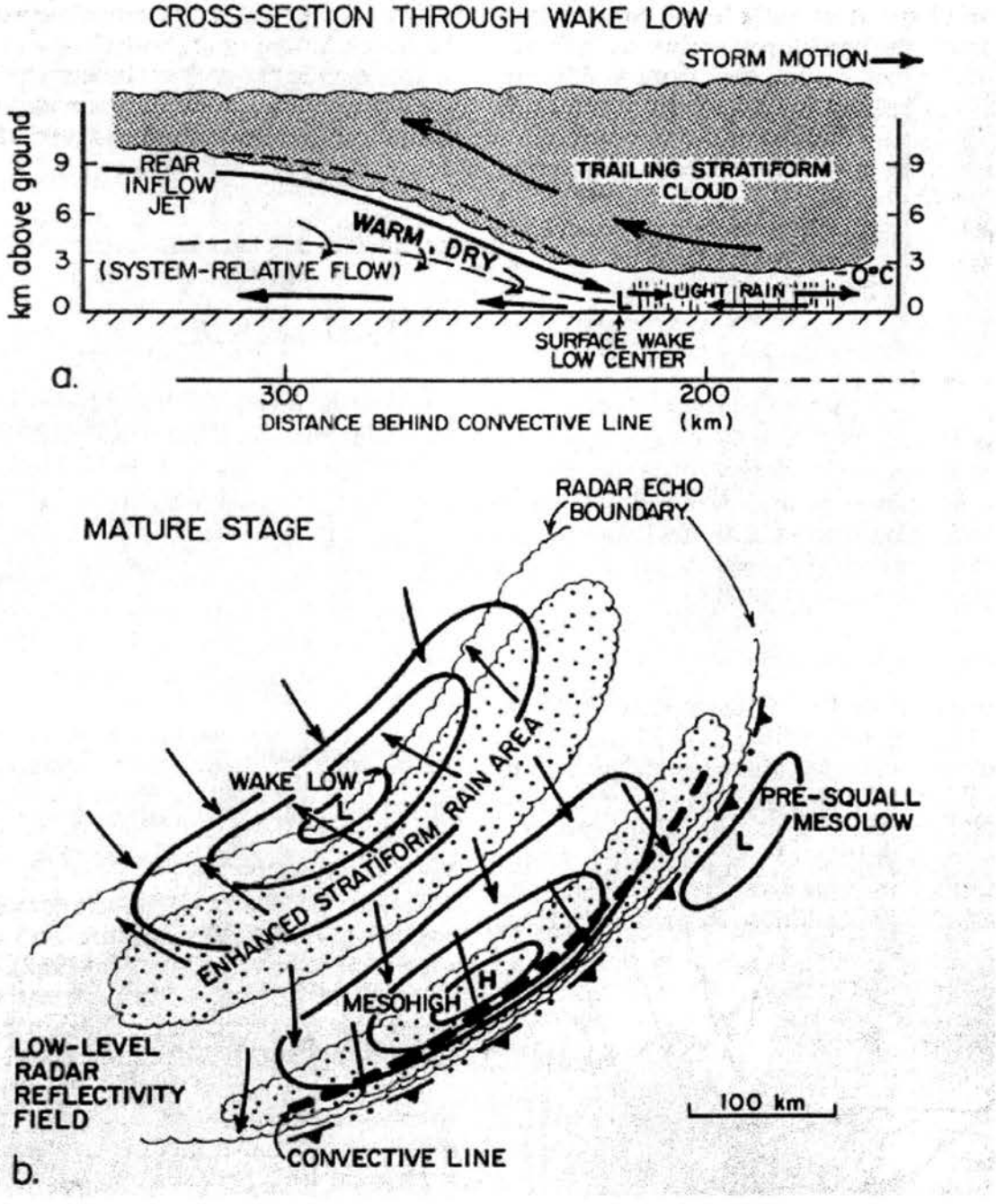

Figure 2.2: Schematic cross section through wake low (a) and surface pressure and wind fields and precipitation distribution during squall line mature stage (b). Winds in (a) are system-relative with the dashed line denoting zero relative wind. Arrows indicate streamlines, not trajectories, with those in (b) representing actual winds. Note that the horizontal scales differ in the two schematic diagrams (Johnson and Hamilton 1988).

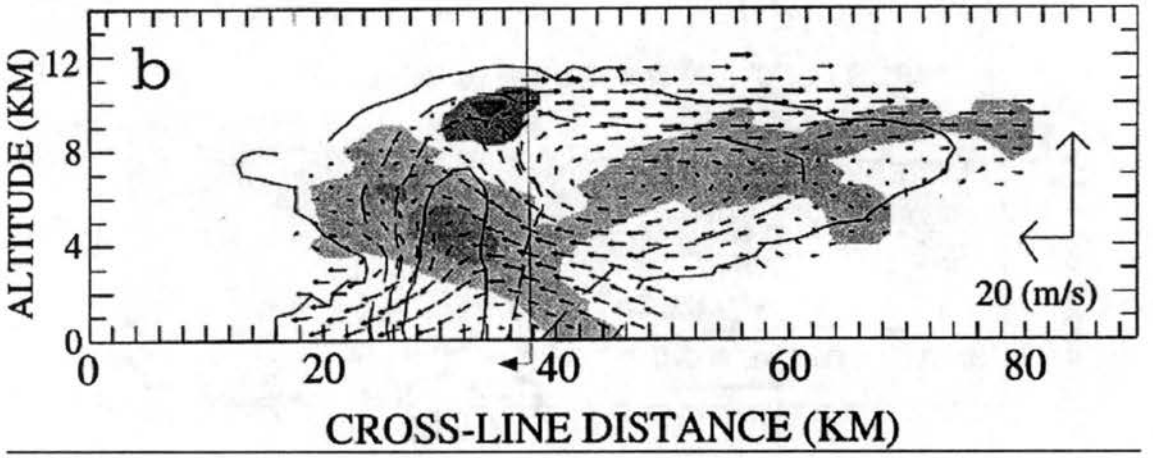

Figure 2.3: Along-line cross section of a cell at the northern end of a linear MCS. Radar reflectivity is contoured in 10 dBZ increments beginning with 10 dBZ. Cross-line distance increases toward the east. The storm is moving to the east-northeast at 7.9 m s^{-1}. Vectors depict line-relative flow. Light shading indicates convergence, contours are 0 and -10^{-4} s^{-1}. Dark shading indicates divergence, contours are 10^{-4} and 2 $\times$ 10^{-4} s^{-1}. Vertical component of the wind is unreliable to the left of the line. (Grady and Verlinde 1997).

This leading-line/trailing-stratiform structure is not the only mode of linear MCS organization, however. In documenting the mesoscale structure of "severe precipitation systems" in Switzerland, Schiesser et al. (1995) found two additional forms of organization: "ahead", in which stratiform rain is found ahead of the convective line, and "none", which had convective cells with no associated stratiform rain. In a case study by Grady and Verlinde (1997), at least part of the squall line studied had leading stratiform rain, followed by the convective line (Fig. 2.3). Convection in this case was initiated 7 to 10 km behind the gust front (not shown) with inflow from ahead of the system. In studying the vertical shear, thermodynamics, and propagation, they noted several differences between the conceptual model of a TS and the squall line they studied. The authors suggested that the TS conceptual model needed to be revised, or another model developed to address some of the differences they found.

After a survey of all linear MCSs occurring in May 1996 and 1997 in the central United States, Parker and Johnson (2000) documented three classes of linear MCS orga-

nization: a convective line with trailing stratiform (TS) (defined by Houze et al. 1990), leading stratiform (LS), and parallel stratiform (PS) precipitation (Fig. 2.4). While TS systems accounted for the majority of the cases, LS and PS MCSs each claimed 19 percent of the total number of MCSs, a greater percentage than was initially expected because few case studies of these types have been published. To determine more information about the structure of the LS and PS systems, average cross-line and along-line flows were calculated for each mode at 4 different vertical levels using sounding data ahead (to the right) of the line (Fig. 2.5). This figure shows storm-relative flow for LSs that does not seem conducive to long-lived convection (i.e., inflow that has been cooled by travelling through stratiform rain). The TS storms in the climatology did have a longer average lifetime than the other modes (12 hours), but LS and PS storms still had an impressive average lifespan of over 6 hours. A study of individual cases in Parker and Johnson (2000) suggested that some LS systems are fed from the rear (west) side of the storm. However, measurements on a scale fine enough to verify this finding were not analyzed.

Moncrieff and Liu (1999) found that the effect of shear on a squall line depends upon the direction of the propagation with respect to the shear vector (Fig. 2.6). They state that for a downshear-propagating gravity current (Fig. 2.6a), shear decreases the mean ascent because horizontal convergence decreases with height. However, the overturning branch of the updraft provides deep lifting of boundary layer air. For an upshear propagating regime (Fig. 2.6b), shear can increase the horizontal convergence and mean ascent, but no overturning branch exists to accentuate lifting and anchor the convection to the organized lifting.

In a storm-relative context, Fig. 2.6a conforms to the TS mode (but without a rear inflow jet) whereas Fig. 2.6b conforms to LS mode, assuming inflow for the LS system is from the rear. Moncrieff and Liu (1999) also note that if the low-level shear is opposite to the surface wind (Fig. 2.6a) and the surface wind opposes the density current, the density current head is enhanced. Such a situation would favor enhanced dynamic lifting at the

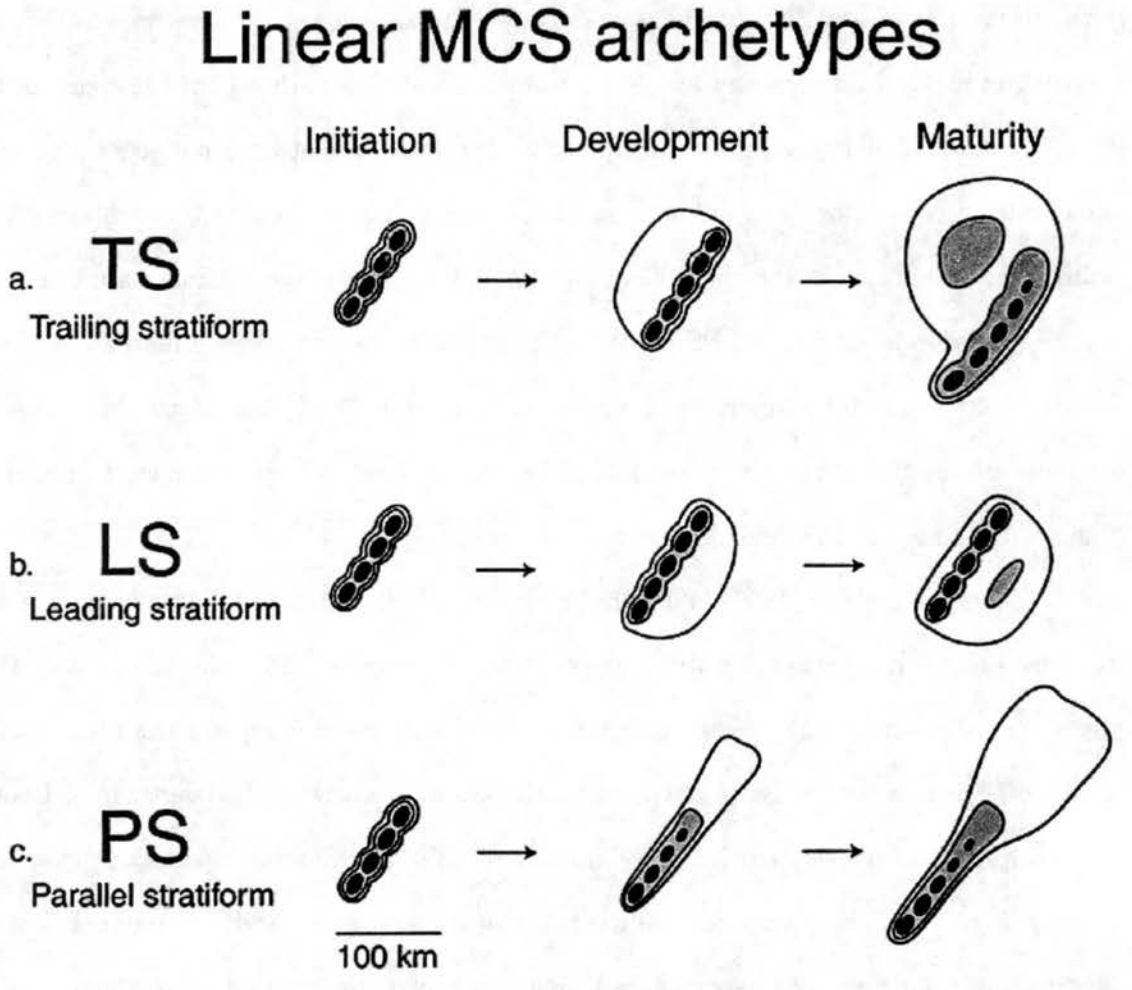

Figure 2.4: Linear MCS modes of organization (Parker and Johnson 2000).

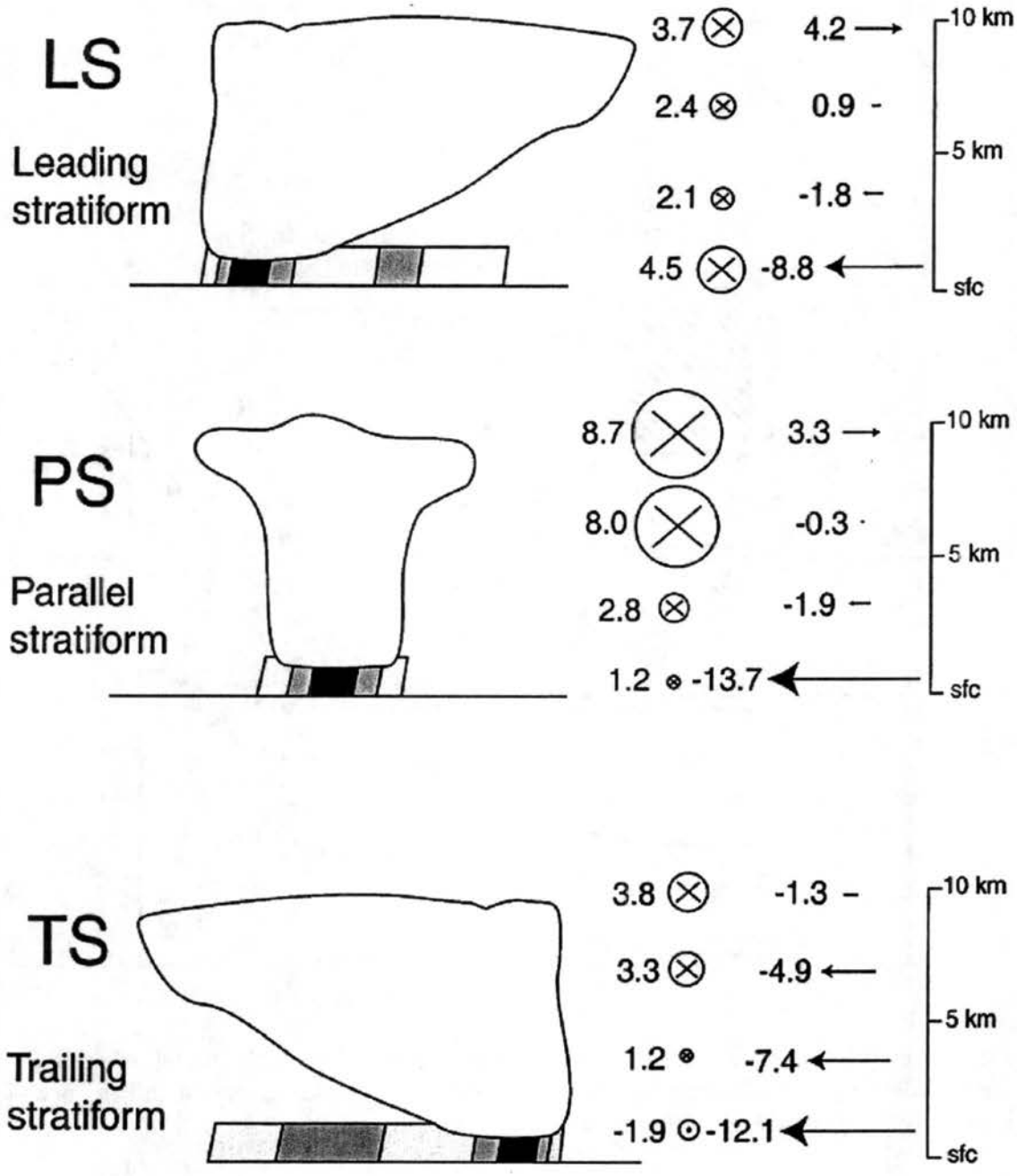

Figure 2.5: Vertical profiles of layer-mean storm-relative pre-MCS winds for linear MCS classes. Wind vectors depicted as line-parallel ($\otimes$) and line-perpendicular ($\longrightarrow$) components in m s^{-1}. Layers depicted are 0–1, 2–4, 5–8, and 9–10 km. Typical base-scan reflectivity patterns (shading) and hypothetical cloud outlines are drawn schematically for reference. MCSs' leading edges are to the right. (Parker and Johnson 2000).

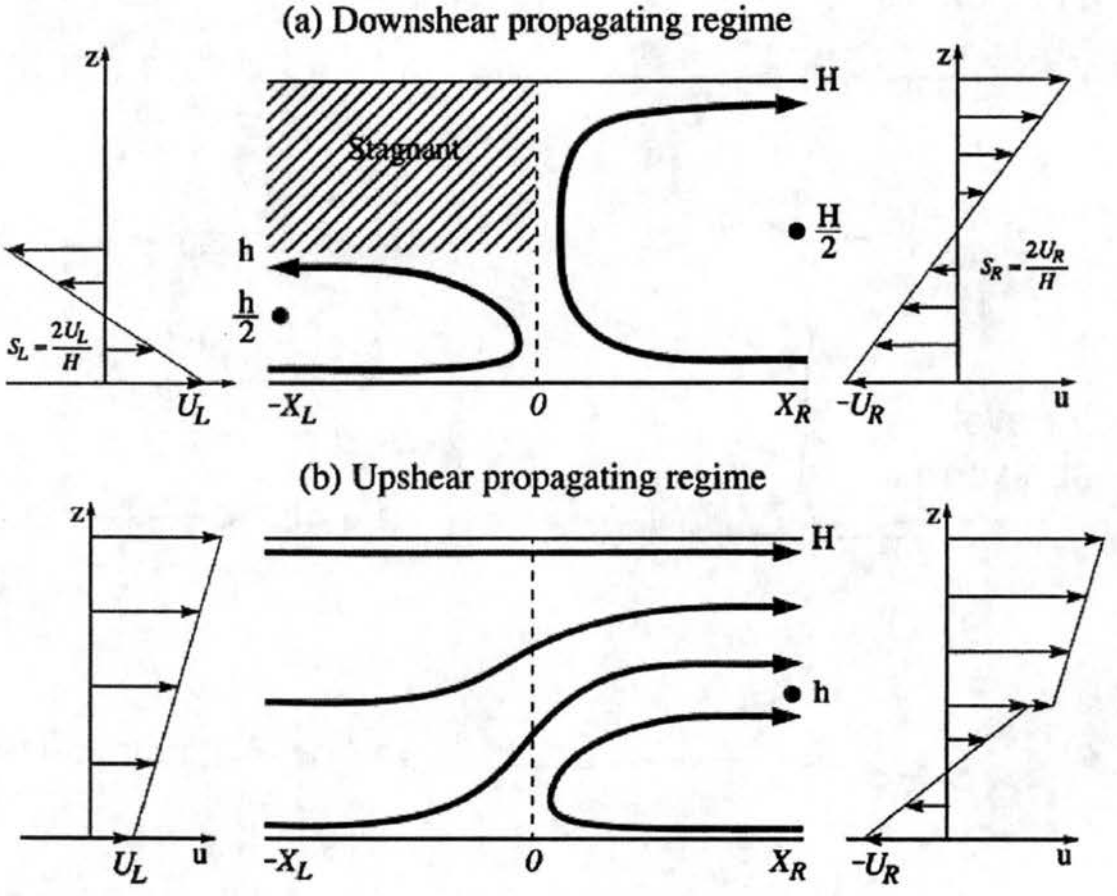

Figure 2.6: Schematic of the relative flow in the idealized dynamical model, where h is the far-field depth of the density current. (a) Downshear-propagating regime and (b) upshear-propagating regime (Moncrieff and Liu 1999).

leading edge of TS systems, but not rear-fed LS systems (Fig. 2.6b). Moreover, vorticity balance arguments per RKW theory do not support optimal lifting at the cold pool edge for rear-fed LS systems since the vorticity of the cold pool and the low-level shear are of the same sign (Fritsch et al. 1994). This suggests further study of LS MCSs is needed to understand their evolution and dynamics.

2.2. Motivation

While numerous studies have documented the structure of TS MCSs, LS and PS storms have received little attention. Both LS and PS storms move more slowly than TS systems (7.3, 10.9, and 13.0 m s^{-1}, respectively), making them potential flash flood producers. Because of the significant differences between PS and LS systems and the large number of cases studied, however, it was not considered feasible to conduct a meaningful study of both modes. The LS systems were chosen for this study because they were the slowest of the three modes, thus implicating them for flash floods (Chappell 1986; Doswell et al. 1996). Some LS systems have been observed to form in an environment similar to the "mesohigh-type" flash flood environment described by Maddox et al. (1979). Also, some individual case studies of LSs by Parker and Johnson (2000) indicated possible rear-feeding while the average did not, suggesting the need for a study of individual LSs with high resolution datasets.

Although the reflectivity structure of LS MCSs appears to be somewhat of a mirror image of TS systems (Fig. 2.4), it is not known if the circulation features are similarly related. The objective of this work is to conduct case studies of at least two LS MCSs within the operational network to document LS structure in detail. Unfortunately, unlike for TS MCSs, field experiments to study LS MCSs have not yet been conducted, so at this time we must rely on operational datasets for their study. Some key questions to be addressed by the research include:

- What are the airflow characteristics for LS storms?

- Are some LS systems fed from the back (west) side of the storm? If so, how does such a flow pattern enhance the potential for heavy rainfall?
- What are the surface features associated with LS systems, e.g., are mesohighs and mesolows present?

The case studies were chosen to answer these questions. The 7 May 1997 case was identified as an LS in Parker and Johnson (2000). Doppler radar data were available for this case, giving it a high resolution dataset that proves to be invaluable for this study. The radial velocities from this dataset can address the first two questions proposed.

The 30 April 2000 case was identified in real-time through the operational network. The storm spent a good deal of its lifetime over the Oklahoma mesonet and the NOAA Wind Profiler Network. The profiler network provides coarse data for answering the first two questions. High resolution mesonet data provide information to address the third question posed. Although the LS passed directly over the Frederick, Oklahoma radar site, the data were not archived, making them unavailable for this study.

Chapter 3

DATA UTILIZED AND METHODS OF ANALYSIS

3.1. Oklahoma mesonet

The Oklahoma mesonet consists of 108 automated surface stations located throughout Oklahoma. A map of station locations can be seen in Fig. 3.1. These stations, with an average spacing of 35 km, measure dry bulb temperature, relative humidity, solar radiation, station pressure, precipitation, average wind speed and direction, maximum wind gust, leaf wetness, and soil temperature (Brock et al. 1995). Five minute averages of most of these data (soil temperatures are averaged over 15 minutes) are reported every 15 minutes and relayed to a central site in Norman, Oklahoma. This central site runs the data through quality assurance tests, detailed in Brock et al. (1995), before archiving it.

Mesonet sites vary in elevation, making a conversion to a single elevation necessary for determining pressure patterns. Pressures were hydrostatically adjusted to an elevation of 366 m, the average elevation of all mesonet stations. Following the example of Loehrer and Johnson (1995), the virtual temperature at a station was assumed to represent the virtual temperature of a column either up to or down to 366 m. The observed station pressure was converted to a 366 m adjusted station pressure by

$$P_{366} = P_s \exp[\tfrac{g(z_s-366)}{R_d \overline{T}_v}]$$

where P_{366} is the pressure adjusted to 366 m, P_s is the observed station pressure, g is gravity's acceleration of 9.8 m s^{-2}, z_s is the station elevation in meters, R_d is the dry-air gas constant of 287 J kg^{-1} K^{-1}, and $\overline{T}_v$ is the mean virtual temperature of the previously

Figure 3.1: Locations of Oklahoma mesonet sites (Brock et al. 1995).

mentioned column.

Mesonet data were gridded to a 10 km × 10 km grid using a Barnes objective analysis technique (Barnes 1973; Koch et al. 1983) with a 350 km radius of influence. This Gaussian weighted-averaging scheme assigns a weight to each observation based on the distance between the datum and the grid point, with the weight asymptoting to zero as the distance approaches the radius of influence. The chosen grid spacing yields a ratio between the grid spacing and the data spacing of 0.29, very close to the recommended range of 0.3–0.5 (Barnes, 1973; Doswell, 1977; Maddox, 1980). The small end of the range is set to avoid unrealistically noisy derivative fields; since the Oklahoma mesonet stations are well maintained and calibrated the value of 0.29 was considered acceptable.

Time-to-space conversions were also performed on the mesonet data to convert dense temporal observations into dense spatial observations (Fujita, 1955; Pedgley, 1962). Assuming a steady-state of 30 minutes, observations from a station 15 minutes prior to the current time are advected downstream of the station by a distance equal to the storm motion times the difference in time between the observation and the current time. An observation taken 15 minutes after the current time would be advected upstream from the station in the same manner. This is done in five minute increments around the current time.

Fujita (1955) quantified this method with the following equation

$$\frac{DA}{Dt} = \frac{\partial A}{\partial t} + (-\mathbf{V} \cdot \nabla A),$$

where A is a property of the complex (any of the measured atmospheric variables), $\frac{DA}{Dt}$ is the total change in property A, $\frac{\partial A}{\partial t}$ is the local temporal change of property A, $-\mathbf{V}$ is the velocity at which the observing stations are moving beneath the MCS (from the perspective of the MCS), and ∇A is the horizontal gradient of the property A. Assuming a steady state of 30 minutes as previously mentioned, the local temporal change becomes negligible and the equation simplifies to

$$\frac{DA}{Dt} = (-\mathbf{V} \cdot \nabla A).$$

Using this equation, changes in property A in time (the left term) can be converted to changes in property A in space (the right part of the right term). The results of this analysis improved the analyses of tight gradients and eliminated some "jumping" of features that occurred in the raw data, but did not significantly change any results.

Perturbation pressure and wind were calculated to track and examine disturbances that appeared to have gravity wave-like features, i.e., have positive surface pressure–wind correlations ($\overline{p'u^{*\prime}} > 0$, where u^* is the wind component in the direction of motion of the gravity wave front) (e.g., Koch and Golus 1988). To calculate perturbation pressure, first the diurnal pressure tide was subtracted from the station pressures (Stumpf et al. 1991). Then each individual station's u wind and pressure adjusted for the diurnal tide were averaged. These average adjusted pressure and u wind values were then subtracted from each adjusted five-minute value to determine the perturbation wind and pressure.

All atmospheric variables, after being gridded with the Barnes technique, were plotted with NCAR Graphics version 4.1.1. NCAR graphics uses cubic splines under tension to draw its isolines. This smoothed the data one more time as it was contoured. Winds were not contoured, but were represented by vectors and displayed in many of the contour plots. Once contour plots were made of a particular variable for each five minute observation period,

the plots were animated using NCAR Graphics 4.1.1 X-Window Interactive Image Display Tool (IDT). These animations were viewed to detect and track transient features such as mesolows or cold pools and to determine the airflow near them. Fifteen minute images of 2 km radar data were overlaid on some plots, and animations of 15 minute observations were used to determine where features formed and propagated in relation to the storm.

3.2. NOAA Wind Profiler Network

The NOAA Wind Profiler Network (NPN) is a set of 32 vertically oriented 404 MHz profiling radars that are irregularly spaced throughout the central United States (with three in Alaska). A list of the 29 sites used for this study, as well as a map of their locations, can be found in Table 3.1 and Fig. 3.2. These profilers measure radial velocities on three different antenna beams (one vertically pointed and two tilted 16.3° from the vertical) at two different modes, taking measurements every 250 m from 0.5 km to 16.25 km above ground level (AGL). The measurement cycle is completed every 6 minutes, and the 6 minute measurements are quality controlled by methods detailed in Weber et al. (1993). The measurements that pass the quality check are averaged over an hour (10 measurements).

The profiler data used for this study were retrieved from an archive maintained by the Data Support Section (DSS) of the National Center for Atmospheric Research (NCAR). The data were accepted a priori because of the strict quality control routines used by NCAR to process the data. Comparisons were made between profiler data and local radiosonde soundings to check for consistency.

NPN data were gridded to a 75 km × 75 km × 250 m grid using a Barnes filter. Vertical slices were taken perpendicular to the MCS to analyze cross-line flow. A storm motion vector was subtracted from the profiler data to determine storm-relative flow. Vorticity and divergence were calculated using centered finite differencing of the gridded data. Vertical motion was then calculated using the kinematic method with the O'Brien (1970) correction.

Table 3.1: Location of NOAA Profiler Network wind profilers utilized in this study.

Identifier	Location
AZC	Aztec, New Mexico
BLM	Bloomfield, Missouri
BLR	Blue River, Wisconsin
CNW	Conway, Missouri
DQU	Dequeen, Arkansas
FBY	Fairbury, Nebraska
GDA	Grenada, Colorado
HBR	Hillsboro, Kansas
HKL	Haskell, Oklahoma
HVL	Haviland, Kansas
JTN	Jayton, Texas
LMN	Lamont, Oklahoma
LTH	Lathrop, Missouri
MBW	Medicine Bow, Wyoming
MRR	Merriman, Nebraska
NDS	Neodosha, Kansas
NLG	Neligh, Nebraska
OKO	Okolona, Missouri
PAT	Palestine, Texas
PLT	Platteville, Colorado
PRC	Purcell, Oklahoma
RWD	McCook, Nebraska
SLA	Slater, Iowa
TCU	Tucumcari, New Mexico
VCI	Vici, Oklahoma
WDL	Wood Lake, Minnesota
WNC	Winchester, Illinois
WNF	Winnfield, Louisiana
WSM	White Sands, New Mexico

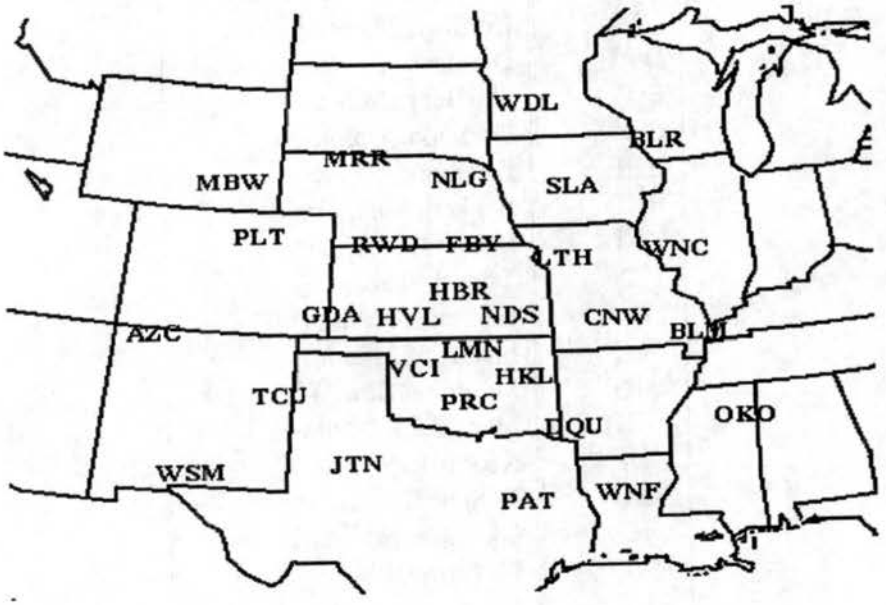

Figure 3.2: Locations of NOAA NPN sites.

3.3. National radar base scan summaries

National radar base scan summaries were provided by the Global Hydrology Resource Center (GHRC) at the Global Hydrology and Climate Center, Huntsville, Alabama. The GHRC receives national composite images from WSI every 15 minutes. These images are instantaneous snapshots from the combined NWS radar data, consisting of the currently operational network of 10 cm and 5 cm NWS radars in the continental U. S. The pixel resolution of the composite images is 2 km × 2 km. The radar data comprises 16 levels of reflectivity, every 5 dBZ, beginning at level 1 (0–5 dBZ).

3.4. Doppler radar

The NEXRAD WSR-88D provides a high resolution tool for both operational and research use. Each radar provides data in real time for operational purposes, and many of them archive Level II (full volume scan) data for research purposes. This dataset provides reflectivity, radial velocity, and spectral width out to 230 km from the radar. In this study reflectivity is used to investigate the LS nature of the storm and examine vertical storm structure. Radial velocities are used to determine the vertical structure of the flow normal to the long axis of the storm as in Houze et al. (1989).

WSR-88D Nexrad Level II Doppler radar data were obtained from the National Climatic Data Center (NCDC). Level II data are saved to exabyte tapes at each individual radar site, and the tapes are sent to NCDC for archiving. The radar data used in this study was obtained in this way. Recently a pilot program, Project CRAFT (http://geosciences.ou.edu/~kkd/c
has been introduced to electronically archive the data, but this electronic archive was not available for the cases studied here.

Radial velocities were unfolded using a manual forced unfolding. The data were gridded to a 1 km × 1 km × 0.5 km grid using a Cressman filter. These gridded data were analyzed using Interactive Data Language (IDL) version 5.4, a data analysis and visualization tool. Vertical cross sections were taken along the line of storm motion so

that storm motion could be subtracted out, yielding storm-relative radial velocities along the cross section. Other cross-sections were examined as well to further investigate the reflectivity structure, but storm-relative values were not calculated for these because they would be ambiguous. Because the gridding process tends to smooth out some reflectivity features, cross sections of ungridded reflectivity were also analyzed in radial coordinates using WSR-88D Algorithm Testing and Display System (WATADS), a system designed by NOAA.

3.5. RUC analyses

Two different versions of the Rapid Update Cycle (RUC) model are used in this study because changes were made to the RUC model between the two case studies. The 7 May 1997 case uses the first version of the RUC, hereafter referred to as RUC-1. The 30 April 2000 case uses the improved version of the RUC, hereafter referred to as RUC-2.

3.5..1 RUC-1

The RUC-1 has 60 km grid spacing, with 25 levels in the vertical. The vertical levels are isentropic-sigma hybrid vertical coordinates. The data are made available with isobaric vertical coordinates with 25 mb vertical spacing. Temperature, height, relative humidity, and u and v wind are available at all isobaric levels, while variables such as the level of maximum winds are at a specific pressure. RUC-1 ingests data from rawinsondes, commercial aircraft, wind profilers, and surface stations (over land and buoys). The only aircraft data used are those with automated digital reporting through ACARS (ARINC [Aeronautical Radio, Inc.] Communications, Addressing, and Reporting System) (Benjamin et al. 1994).

3.5..2 RUC-2

The RUC-2 has 40 km grid spacing, with 40 vertical levels. Isentropic-sigma hybrid vertical coordinates are used. The data are made available with isobaric vertical coordinates with 25 mb spacing. Geopotential height, temperature, u wind, v wind, and relative humidity are available at all levels. Other variables, such as mean sea level pressure, are available only for the surface. RUC-2 ingests VAD wind profiles, high-resolution ascent-descent aircraft reports, ship reports, both GOES and SSM/I integrated precipitable water retrievals, GOES high-density cloud drift winds, and tropical storm dropwindsonde data, in addition to all the data ingested by RUC-1 (Benjamin et al. 1998).

3.6. National Weather Service rawinsonde soundings

Rawinsonde soundings are taken twice daily, at 0000 UTC and 1200 UTC, by the National Weather Service, at irregularly spaced locations throughout the country. A map of sounding locations relevant to the two case studies can be found in Fig. 3.3. These soundings measure temperature, dew point, wind speed and direction, pressure, and height. A detailed description of the sounding network can be found in Golden et al. (1986). Nearby soundings were examined for each case to determine storm environment and to check other datasets for consistency. The soundings were examined to determine the general environment in which the LS formed.

3.7. National Center for Environmental Prediction analysis charts

The National Center for Environmental Prediction (NCEP) upper air analysis maps were obtained from NCDC. These maps are produced twice daily at 0000 and 1200 UTC using data from the radiosonde sounding network. The electronic archive for these maps dates back to January 1998, however, so another source needed to be used to produce upper air charts for the 7 May 1997 case.

Figure 3.3: Locations of NWS rawinsonde sounding sites in the central U.S.

3.8. Eta Data Assimilation System analysis charts

The Eta Data Assimilation System (EDAS) maps were obtained from NOAA's Air Resources Laboratory. EDAS is an intermittent assimilation and optimum interpolation analysis. It has a 3 hourly archive, and the 3 hour analysis updates allow for the use of high frequency observations such as wind profiler, NEXRAD, and aircraft data (for more information on EDAS, see http://www.arl.noaa.gov/ready-bin/edas.pl). A comparison was made between EDAS and NCEP maps for the 30 April 2000 case to ensure the quality of the EDAS upper air analyses. EDAS produced similar maps to those from NCEP for the 30 April 2000 case, instilling confidence in its use for the 7 May 1997 case.

3.9. Surface data

Data to produce surface maps were obtained from NCDC's National Virtual Data System. This dataset provides temperature, precipitation, wind, and pressure data for over 300 surface stations nationwide. These data were obtained for stations in the area of interest and plotted using the Grid Analysis and Display System (GrADS) version 1.7Beta9. The placement of frontal positions was aided by analyses of potential temperature.

3.10. Satellite data

Satellite images were obtained from the Cooperative Institute for Research in the Atmosphere (CIRA). The 1 km resolution visible satellite images were taken from the geostationary satellite GOES-10 (GOES East). The times used were chosen because they had sun angles high enough to provide good contrast in the images.

Chapter 4

CASE I: A SLOW-MOVING, FLASH FLOOD-PRODUCING LS MCS OVER TEXAS AND OKLAHOMA

On 30 April 2000, the first convective cells of what would be an LS MCS initiated around 0700 UTC just south of the southwest corner of Oklahoma. This storm produced flash floods from southwestern to central Oklahoma, with cooperative station rainfall totals of over 4 inches in some areas (Fig. 4.1).

4.1. Synoptic environment

At 1200 UTC on the morning of 30 April 2000, the upper level flow pattern across the U.S. was fairly meridional (Fig. 4.2). There was a ridge over the west coast and the midwest, with a trough located over the Rocky Mountain region. The center of what appears to be a cut-off low was located in northern New Mexico. The southwestern corner of Oklahoma and the Texas panhandle, where the MCS formed, was located in the right entrance region of a jet streak (Fig. 4.3). This was also an area of upper level diffluence, which assisted in the formation of the convection over this region.

Surface conditions were complex. Potential temperature maps aided in determining frontal positions, but with sparse surface observations, positioning the surface low was somewhat subjective. At 0900 UTC there were two surface lows in Texas (Fig. 4.4a). One was just north of Amarillo and had a stationary front extending southeastward from it. Convective cells of the LS MCS were forming just ahead of this stationary front with a NW–SE orientation. A more detailed description of the evolution of the reflectivity will

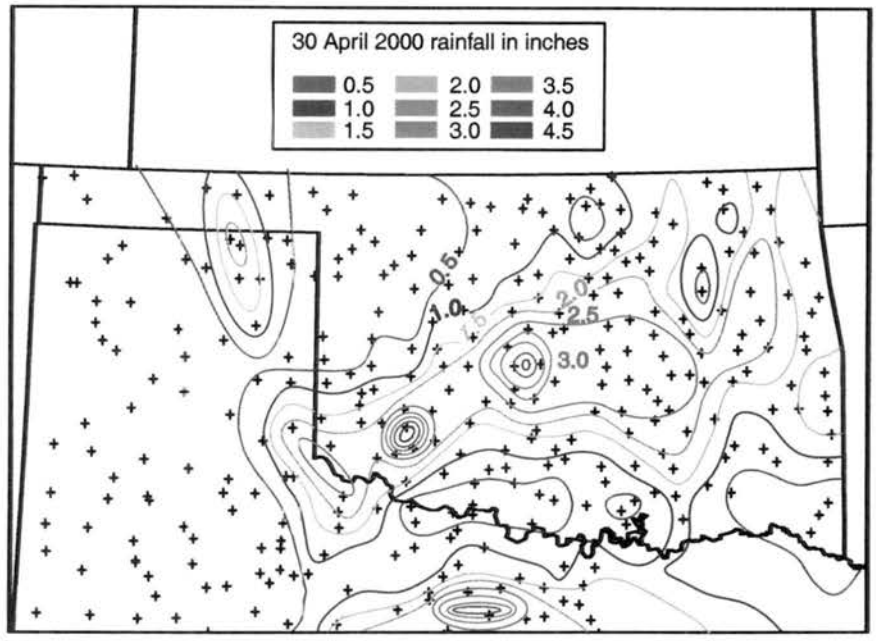

Figure 4.1: Total rainfall (in inches) gathered from 313 cooperative stations for 30 April 2000. Station locations are indicated by +. Two maxima in Oklahoma were the locations of flash floods.

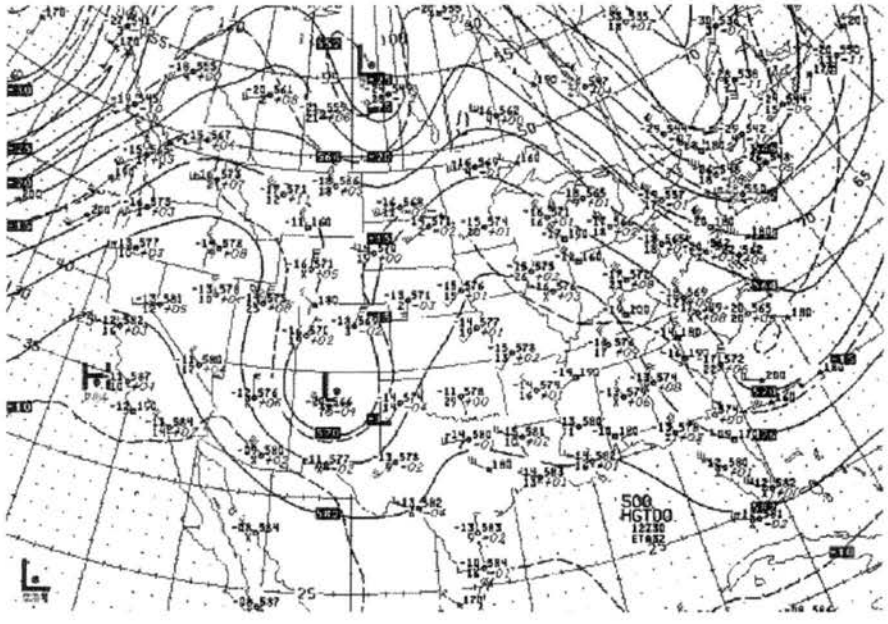

Figure 4.2: NCEP 500 hPa analysis chart for 1200 UTC on 30 April 2000: heights (dm: solid contours) and temperatures (°C: dashed contours).

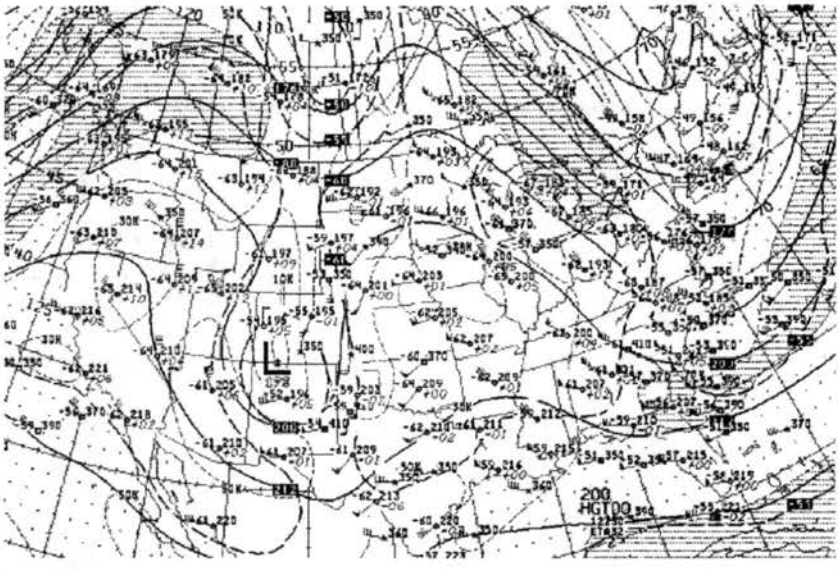

Figure 4.3: NCEP 200 hPa analysis chart for 1200 UTC on 30 April 2000. Heights (dm - 1000: solid contours), temperatures (°C: dark dashed contours) and wind speeds (kts: light dashed contours, speeds $\geq$ 60 kts shaded).

be given later. The other surface low was on the Texas–New Mexico border at 32.7 N with a dryline extending both north and south of it. A cold front extending from a low in Nebraska dipped toward the SW as it cut across the corner of the Oklahoma panhandle. By 1200 UTC the lows had merged (Fig. 4.4b). The surface low at 1200 UTC was located in the southwestern portion of the Texas panhandle. A stationary front stretched slightly northward from the low and then dove southeastward, finally paralleling the Oklahoma-Texas border. The convective line of the MCS was still parallel to the stationary front and a stratiform rain region was developing ahead of the convective line. The dryline extended from the low straight south. The cold front from Nebraska dipped south-southwestward to just north of the low. An outflow boundary from convection north of the LS MCS extended from the Oklahoma panhandle northeastward.

By 1500 UTC the surface low had moved SE, seemingly pushed by the cold front that was moving that way (Fig. 4.4c). The stationary front had moved northward and extended northeastward from the low before dipping southeastward and running parallel to the Oklahoma–Texas border. This movement was the beginning of a transition from a stationary front to a warm front that took place over the next few hours (not shown). The convective line was shorter than before and still close to the front. A significant stratiform rain area had developed. The dryline was surging ahead of the low, and the outflow boundary from the convection to the north of the LS MCS had reached the stratiform region of the LS. Throughout the period the convective line remained nearly stationary (contributing to the heavy rains) while the stratiform precipitation region expanded northeastward.

Soundings from Amarillo, Texas (Fig. 4.5a) and Norman, Oklahoma (Fig. 4.5b), depict the environment behind and ahead of the storm, respectively. Amarillo had a capping inversion between 700 and 750 hPa and strong southwesterly flow from the surface up to 300 hPa. There was also a significant amount of moisture from the surface up to 750 hPa.

Norman's sounding shows some significant differences. There was a strong surface temperature inversion at Norman, depicting a strong stable layer ahead of the MCS and

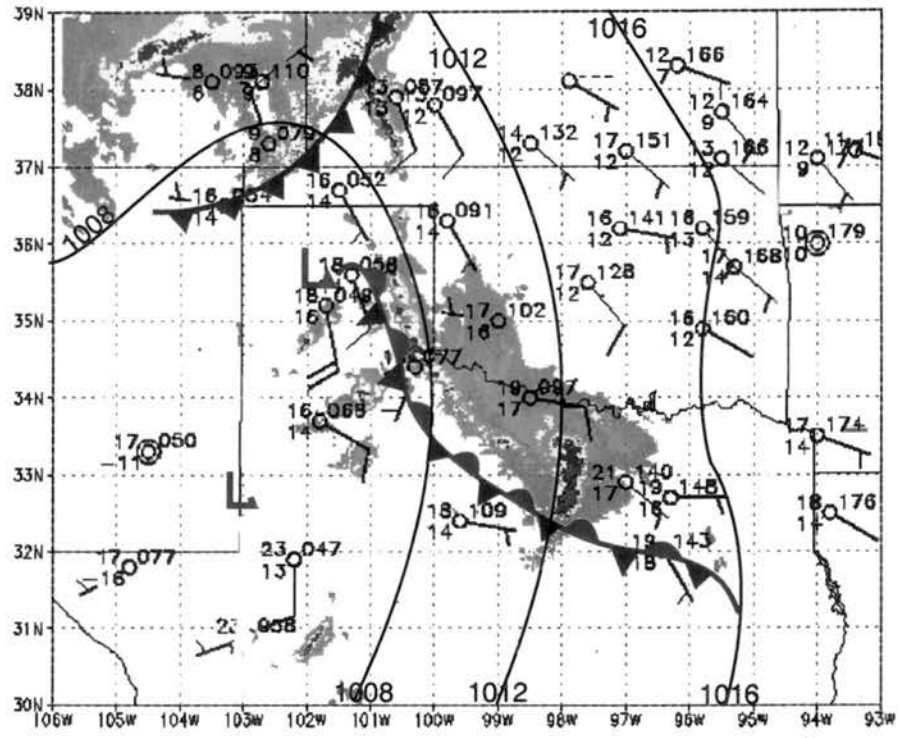

(a) 0900 UTC

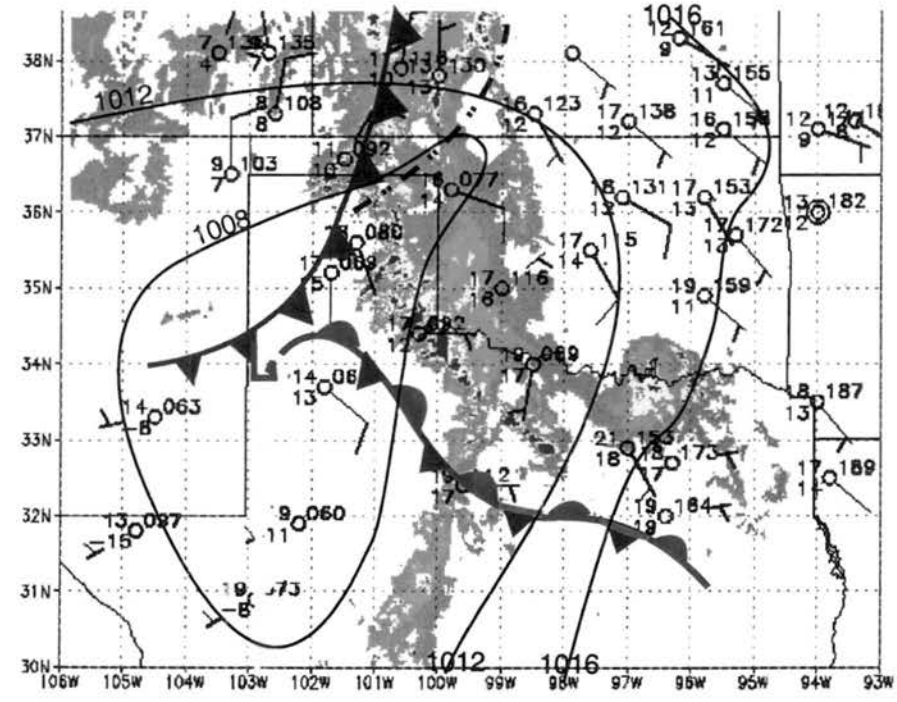

(b) 1200 UTC

Figure 4.4: Surface analyses for (a) 0900 UTC, (b) 1200 UTC, and (c) 1500 UTC. Reflectivities are shaded as follows: dark green = 20–30 dBZ, light green = 30–40 dBZ, yellow = 40–50 dBZ, and red $\geq$ 50 dBZ. Pressure is contoured every 4 hPa.

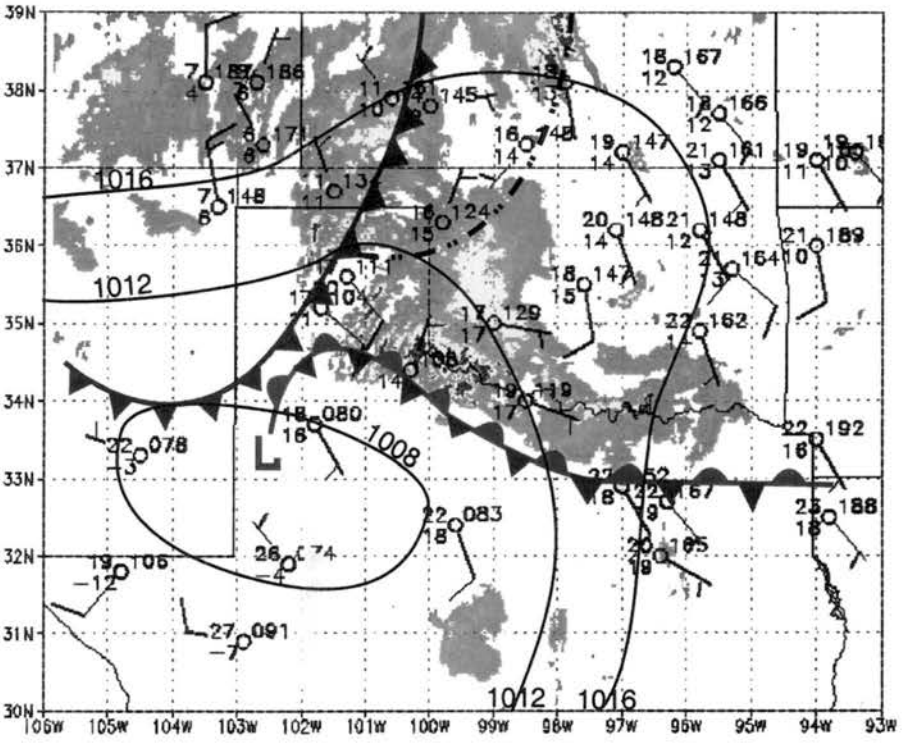

(c) 1500 UTC

Figure 4.4: *Continued*

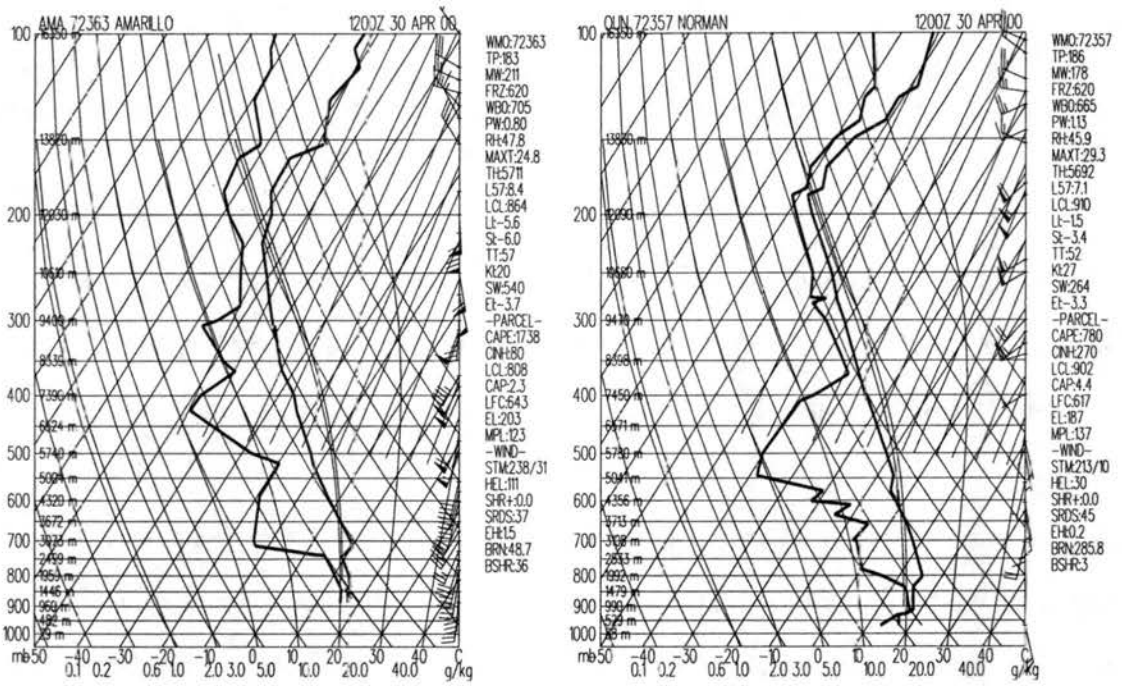

(a) Amarillo, Texas

(b) Norman, Oklahoma

Figure 4.5: 1200 UTC soundings from (a) Amarillo, Texas, and (b) Norman, Oklahoma on 30 April 2000.

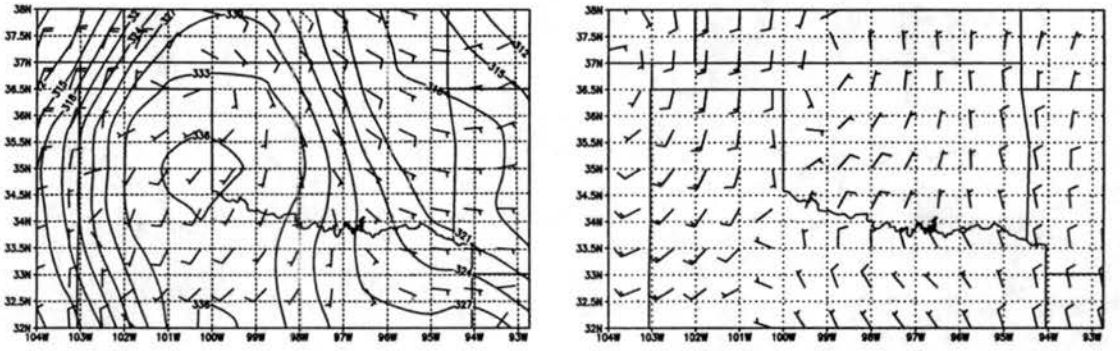

(a) 800 hPa (b) 500 hPa

Figure 4.6: Cross sections of storm-relative RUC wind barbs for (a) 800 hPa (with θ_e contoured every 3 K) and (b) 500 hPa at 1200 UTC. One full barb = 10 m s^{-1}, one half barb = 5 m s^{-1}.

indicating the presence of the stationary front. A moist layer extended from the surface to 825 hPa. Winds from the surface up to almost 250 hPa were much weaker than at Amarillo and were out of the southeast to southwest (they were stronger and more westerly above 250 hPa).

Cross sections of 40-km RUC data along pressure levels also yield insight into the large-scale features. At 1200 UTC there was a strong low-level jet evident from 900 hPa to 800 hPa (ground-relative winds not shown). Removing storm motion from the flow, there was significant storm-relative inflow from the rear, about 10 m s^{-1} from SSW (Fig. 4.6a). This rear inflow of warm, high-θ_e air fueled the storm and allowed it to perpetuate and produce floods. Storm-relative flow at 500 hPa ahead of the MCS was FTR at 10 m s^{-1} (Fig. 4.6b).

At 200 mb there was strong (15–25 m s^{-1}) cross-line RTF flow to advect hydrometeors ahead of the convective line (Fig. 4.7a). From 1200 to 2000 UTC, these upper level winds shifted from southwesterly to southerly (Fig. 4.7b). These southerly winds advected hydrometeors to the north as the convective line attained a more N–S orientation (Fig. 4.8l, later). This change in the flow shifted the stratiform precipitation from in front of the MCS

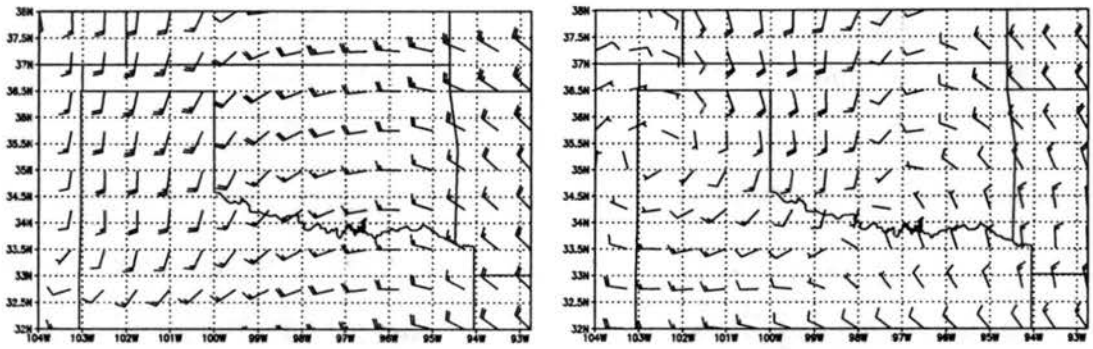

(a) 1200 UTC (b) 2000 UTC

Figure 4.7: Cross sections of storm-relative RUC wind barbs at 200 hPa for (a) 1200 UTC and (b) 2000 UTC.

to parallel to it at its northern edge. This stage could be classified as either a PS system, or as asymmetric (Houze et al. 1990), which is typical of the latter stages of the lifecycle of a TS MCS.

Overall, the synoptic setup for the day showed the atmosphere to be stably stratified at low levels over Oklahoma. A stationary front divided the air masses over the Texas panhandle and Oklahoma, with a strong stable layer ahead of the front. Behind the front there was significant moisture up to 750 hPa with southwesterly flow in mid-to-upper levels. This flow tapped into a stream of high-θ_e air from behind the system. The stability of the air mass ahead of the front indicates the difficulty that would ensue getting a surface parcel from this air mass to rise, and emphasizes the potential importance of rear-feeding to the LS MCS that developed. This may be similar to cases of elevated convection due to frontal overrunning discussed by Colman (1990) and Trier and Parsons (1993). Upper level flow was southwesterly for most of the lifecycle, changing to southerly later and shifting the location of stratiform precipitation as it did so.

4.2. Horizontal cloud and precipitation structure and their evolution

A sequence of hourly reflectivity maps shows the evolution of the MCS from 0600 to 1700 UTC on 30 April 2000 (Fig. 4.8). The convective line of what became the LS

west of the southwest border of Oklahoma formed in a NW–SE line. From 0700 to 1200 UTC the convective line of the MCS developed along the NW–SE line, but there was little overall system motion. This lack of movement of the cells contributed to the heavy rains that occurred. Animations of radar reflectivity show evidence of back-building cells, which then moved over the same area producing heavy rain (Bluestein and Jain 1985; Chappell 1986) and also contributing to the floods of the day. After 1200 UTC the storm propagated toward the northeast, with an overall storm motion vector of 9 m s^{-1} toward 32°.

Leading stratiform rain began to develop around 1000 UTC (Fig. 4.8e). It expanded toward the northeast and developed all along the convective line by 1300 UTC (Fig. 4.8h). At 1400 UTC (Fig. 4.8i), a separation developed between the stratiform rain and the convective line. This is indicative of the transition zone, analagous to that observed for TS systems (Smull and Houze 1985). The stratiform rain continued to expand and propagate to the NE through 1500 UTC (Fig. 4.8j), but shrank after that. The stratiform rain led the convective cells until 1800 UTC (not shown), when the upper level winds shifted (discussed in the previous section) and the stratiform rain relocated to be parallel with the convective line. Other examples of this type of transformation can be found in Parker and Johnson (2000).

The convective cells for this storm (and others observed by the author) are more discontinuous than those typically seen in TS storms (Carbone 1982; Rutledge et al. 1988; Houze et al. 1989, Houze et al. 1990). A potential explanation for this will be discussed later. At times early in the storm's lifetime they are elongated perpendicular to the convective line (Figs. 4.8f, g, and h). As the system matures (Figs. 4.8i, j, and k), convective cells appear canted at 45–60° angles with respect to the line. This orientation is similar to the canted alignment of cells of TS systems found by Houze et al. (1990) to be 45–90° with respect to the convective line. Reasons for this canting are not known.

The visible satellite image at 1415 UTC (Fig. 4.9) confirms what the radar data imply. Strong convective cells are seen at the western edge of the storm, which is consistent

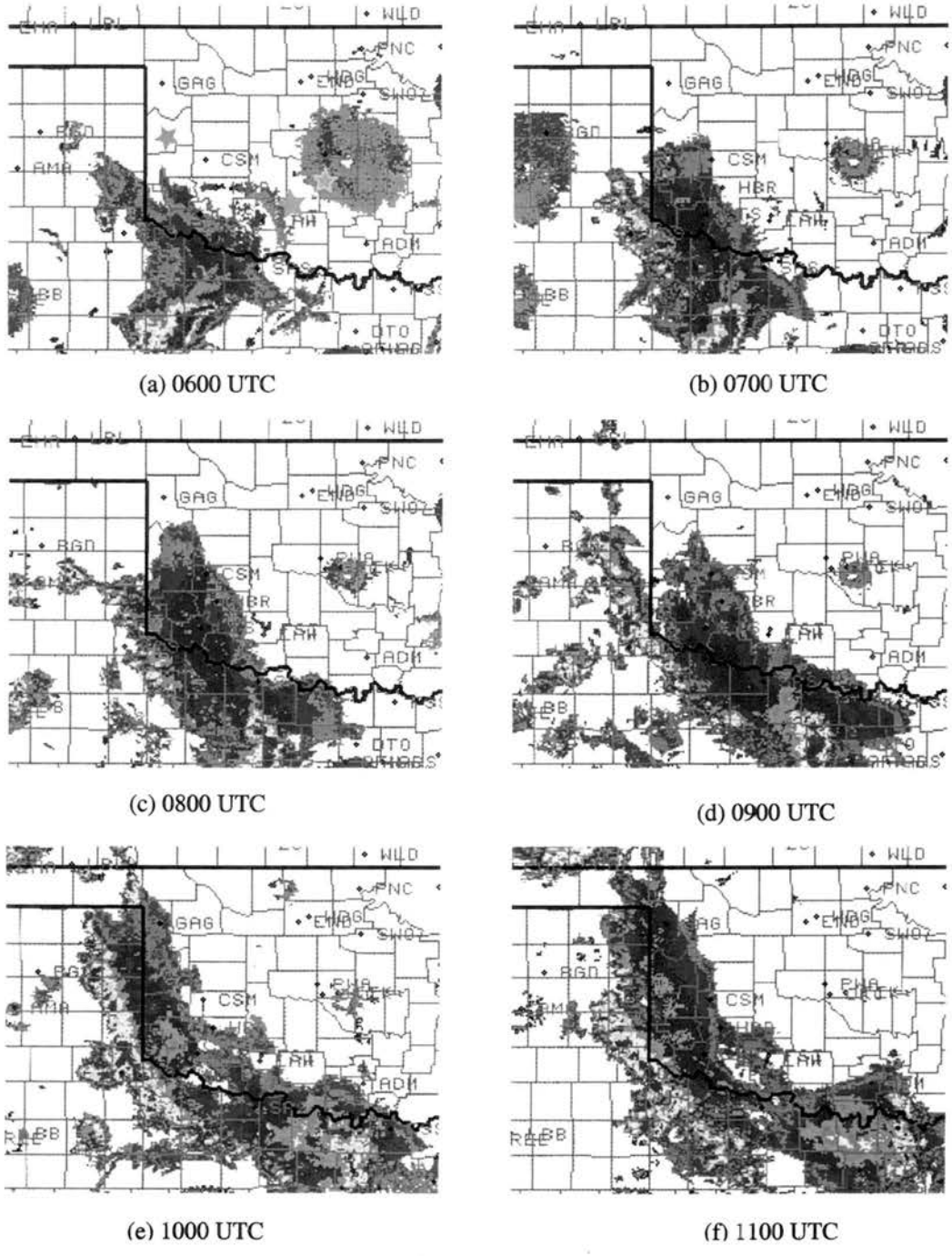

(a) 0600 UTC

(b) 0700 UTC

(c) 0800 UTC

(d) 0900 UTC

(e) 1000 UTC

(f) 1100 UTC

Figure 4.8: Time series of radar reflectivity for 30 April 2000. In (a), stars indicate the location of specific mesonet stations discussed later. Green = CHEY, pink = MANG, orange = WASH, and light blue = ACME. In (j), line A-B is used for Figs. 4.16, 4.17, 4.18, and 4.19.

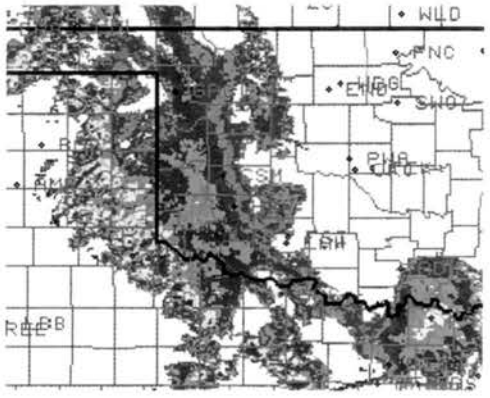

(g) 1200 UTC

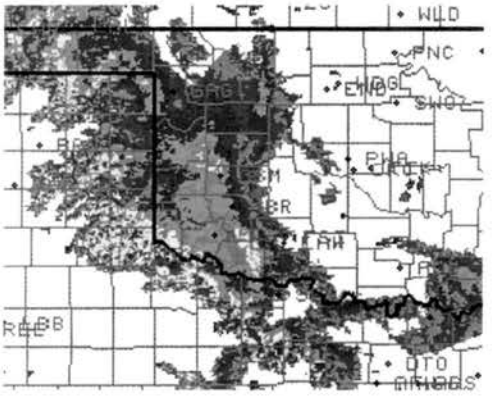

(h) 1300 UTC

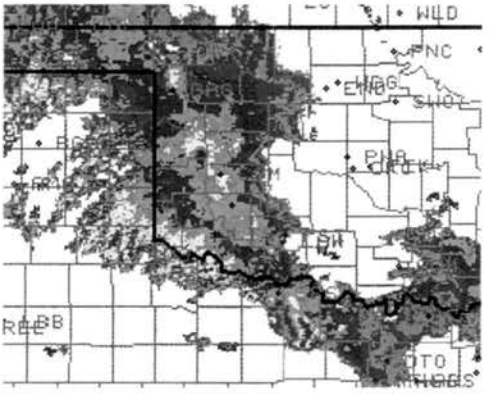

(i) 1400 UTC

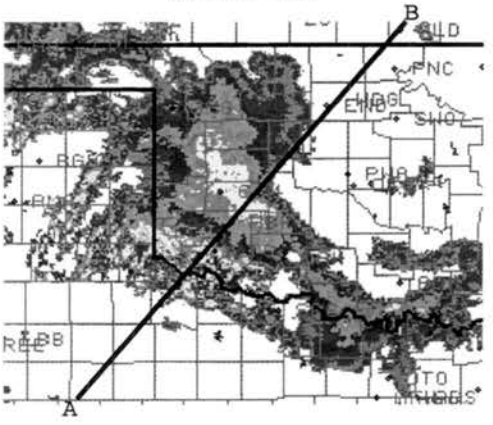

(j) 1500 UTC

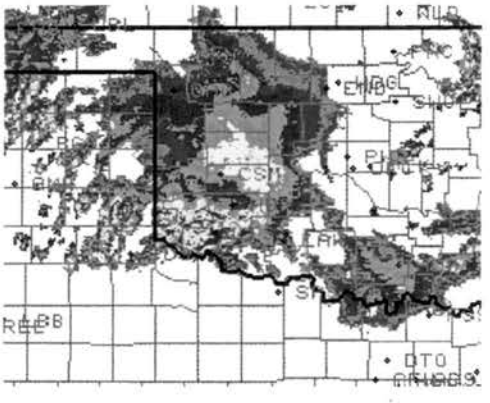

(k) 1600 UTC

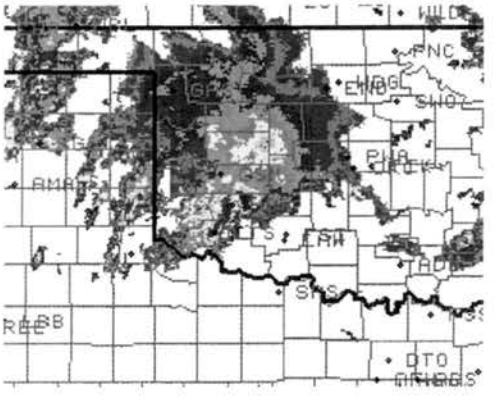

(l) 1700 UTC

Figure 4.8: *Continued*

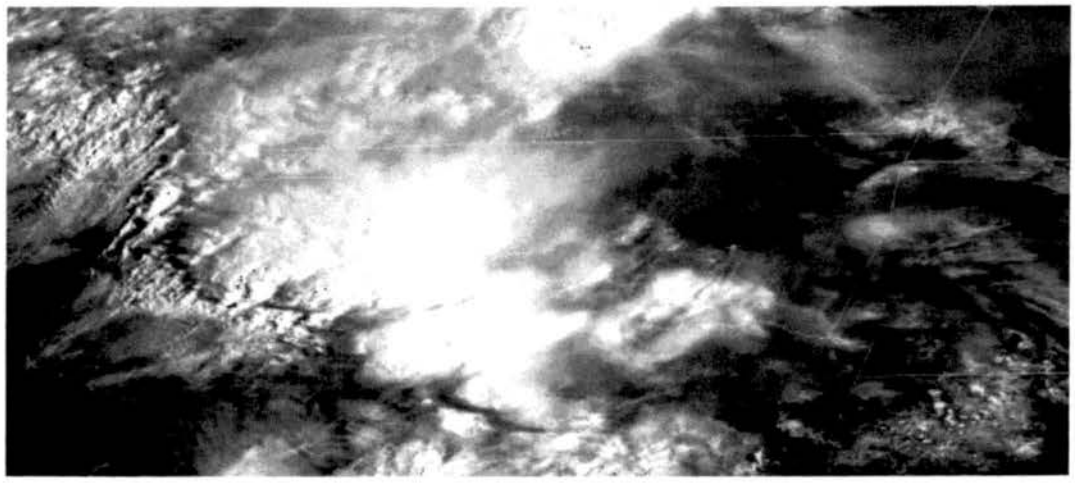

Figure 4.9: Visible satellite image over Oklahoma at 1415 UTC.

with the location of the high radar reflectivities around that time (Fig. 4.8i). There is a distinctive difference between cloud tops at the southwestern edge of the storm and those to the northeast. The cloud top is more uniform to the northeast, suggesting a greater likelihood of stratiform rain in this area.

To summarize, the 30 April LS MCS began as a slow-moving, NW–SE oriented convective line and then stratiform precipitation developed to its northeast. Convective cells were discontinuous. In early stages of the storm's lifetime, they were elongated in a direction perpendicular to the convective line. In the later stages, the convective cells became more canted toward a 45–60° angle. Animations of reflectivity showed evidence of back-building cells, which presumably contributed to the heavy rainfall. Features such as a transition zone and stratiform region of enhanced reflectivity were observed, similar to, but a mirror image of, those in TS systems.

4.3. Surface features sampled by the Oklahoma Mesonet

A sequence of plots of the pressure field (Fig. 4.10) from the Oklahoma mesonet show the presence of a mesolow in advance of the stratiform region, referred to as a leading mesolow. This mesolow formed near the northernmost part of the stratiform region (Fig.

4.10b,c). At 0930 UTC (Fig. 4.10d) the mesolow was in front of the MCS toward its midsection. The mesolow moved east for the next hour, staying just ahead of the stratiform rain area. At 1030 UTC (Fig. 4.10f), the mesolow started moving to the southeast along the front edge of the stratiform region, parallel to the storm orientation. It continued this movement to the time it exited the coverage of the mesonet at about 1230 UTC (Fig. 4.10j).

A station plot displaying the effect of this mesolow on a specific station is shown in Fig. 4.11. The stratiform rain for this station began 75 minutes after the passage of the mesolow, with convective rain not arriving for another few hours. In a general sense, the time series in Fig. 4.11 is the reverse of that for a TS system, where the wake low appears at the back edge of the stratiform rain region (Johnson and Hamilton 1988, their Fig. 11). However, the analogy between the two systems (LS and TS) is not obvious, as we shall see.

Further analysis of this mesolow shows that it may have structure similar to a gravity wave. At several stations, the wind speed in the direction of the movement of the pressure perturbation, u^*, was calculated. The mean station pressure and mean u^* were then removed from each observation to produce the plots in Fig. 4.12 (as in Ralph et al. 1993). Subjectively, there seems to be good agreement in phase, which is expected for gravity waves. For a more objective determination, the pressure-wind correlation was calculated over the time period of most significance for each station (Koch and Siedlarz 1999). High correlation values can indicate a strong gravity wave signal. Correlation values for selected stations in the vicinity of the mesolow are shown in Table 4.1. Correlation values greater than 0.24 are statistically significant at the 95% level.

It is difficult, however, to determine the true nature of this mesolow with the available data. No evidence of a mesohigh is apparent in the data, therefore the mesolow does not seem to be part of a mesohigh-wake low couplet that is typical of gravity waves. This signature can develop in response to low-level evaporative cooling in the stratiform region (Haertel and Johnson 2000). In particular, these authors found that for a travelling stratiform rain area, a mesohigh appears ahead of the rain region and a wake low to its rear.

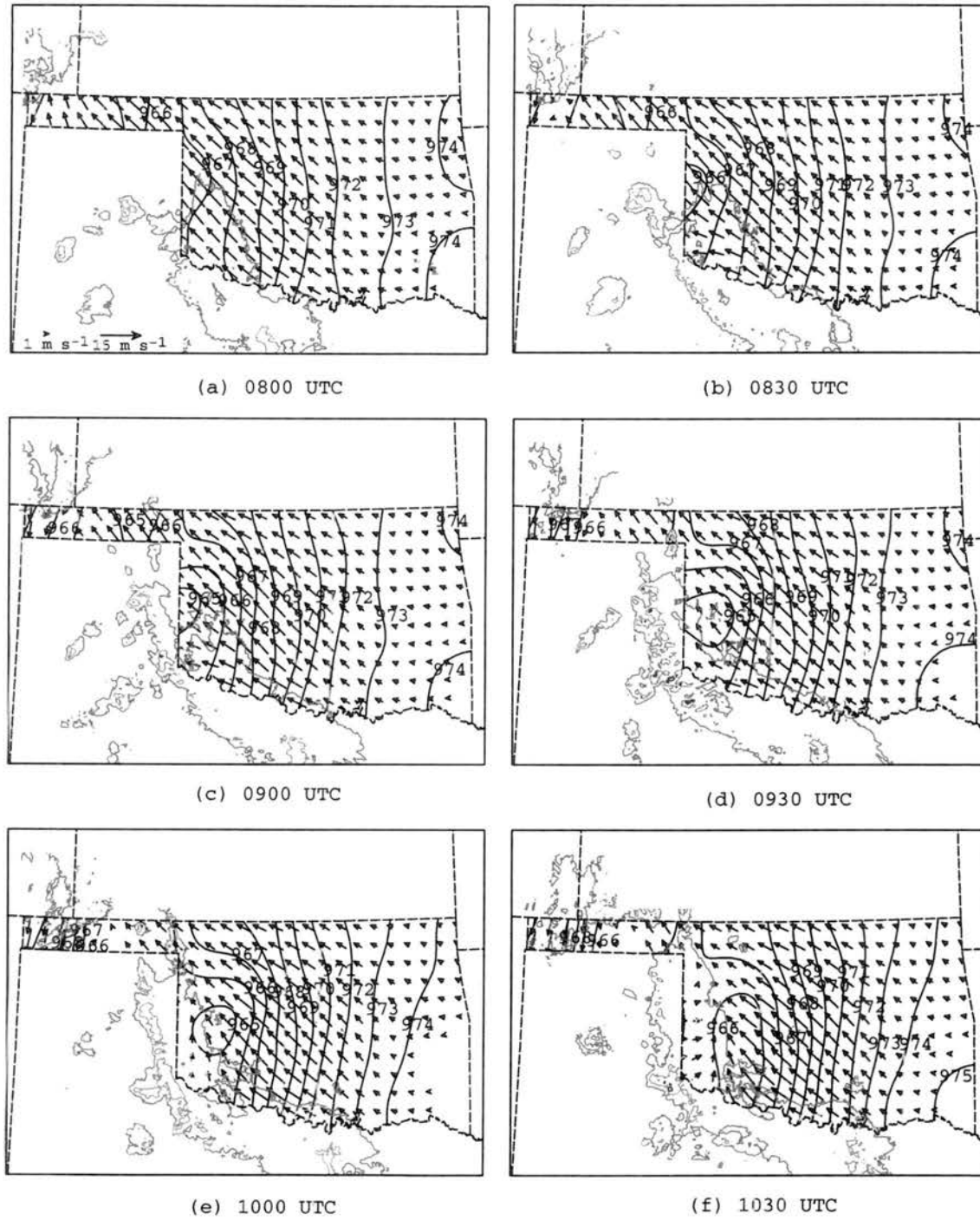

Figure 4.10: Time series of adjusted station pressure (hPa) and ground-relative surface wind vectors from the Oklahoma mesonet. Radar reflectivity is contoured. Green contour = 20 dBZ, yellow contour = 40 dBZ, orange contour = 50 dBZ.

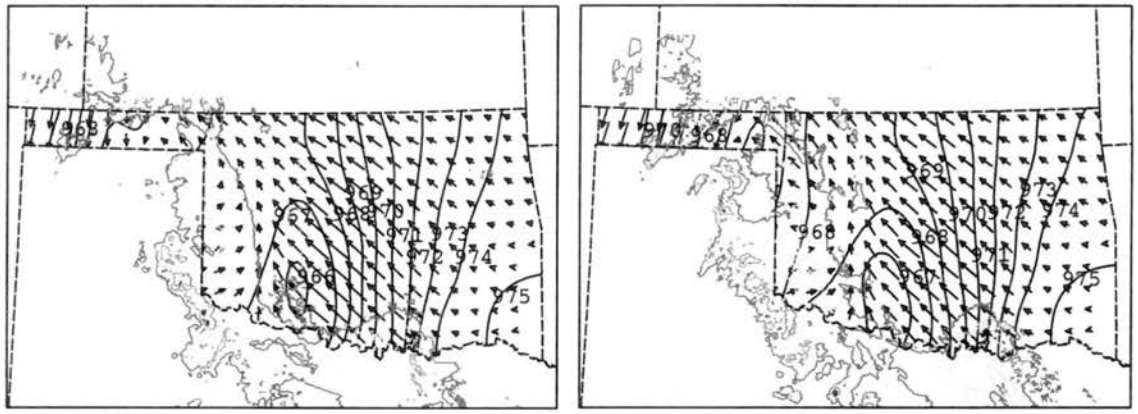

(g) 1100 UTC (h) 1130 UTC

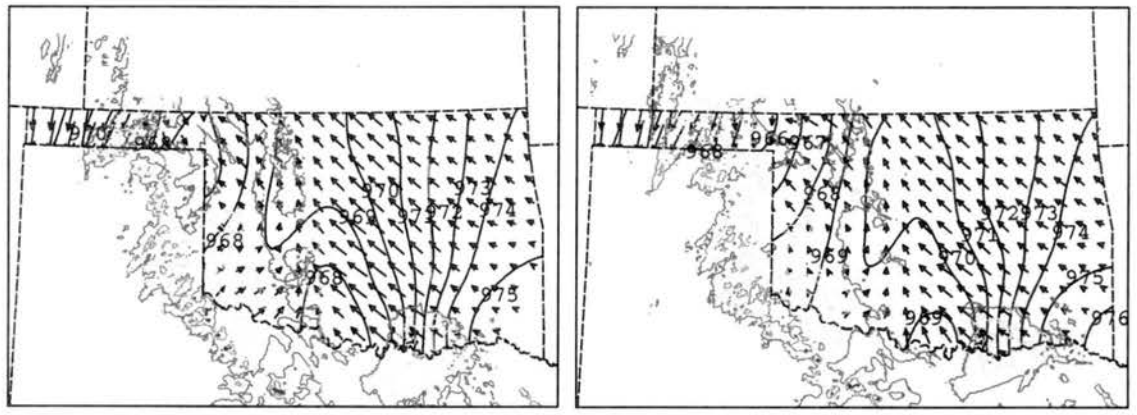

(i) 1200 UTC (j) 1230 UTC

Figure 4.10: *Continued*

Table 4.1: Station Identifiers affected by mesolow and their correlation coefficients.

Identifier	Correlation Coefficient
ACME	0.40
APAC	0.35
KETC	0.47
MEDI	0.85
NINN	0.77
RING	0.09
WALT	0.20
WASH	0.79

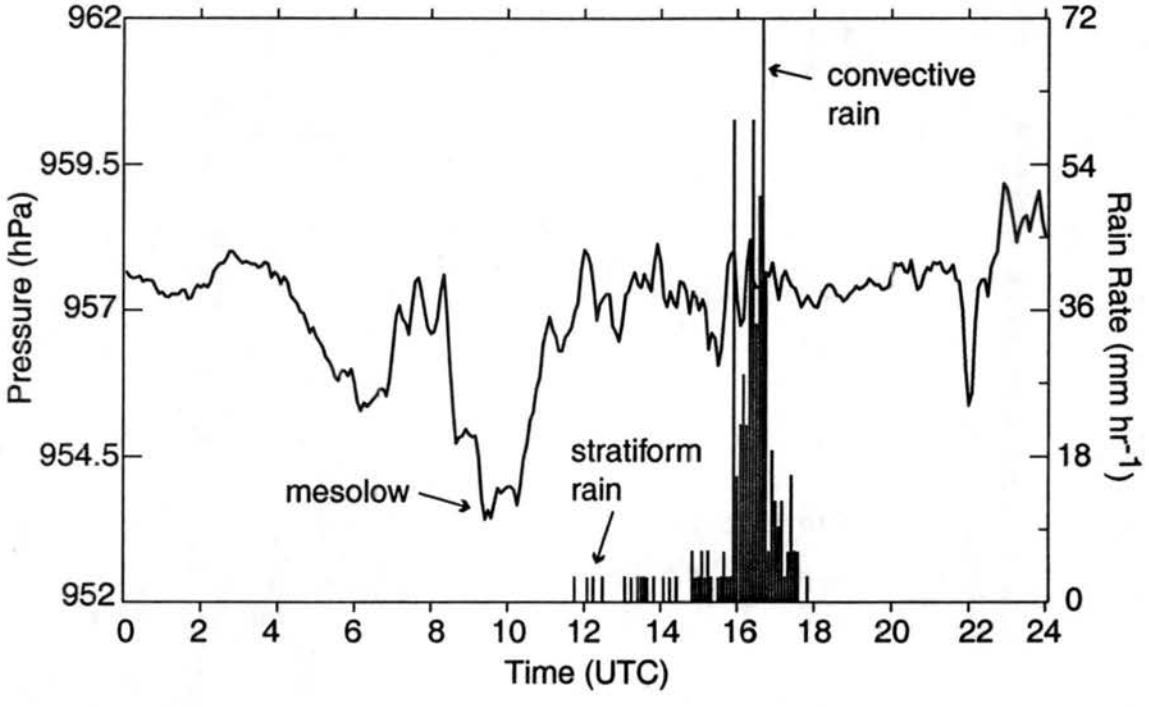

Figure 4.11: Station plot for MANG (see Fig. 4.8a for location). Pressure (line) is in hPa, rain rate (bars) is in mm hr^{-1}.

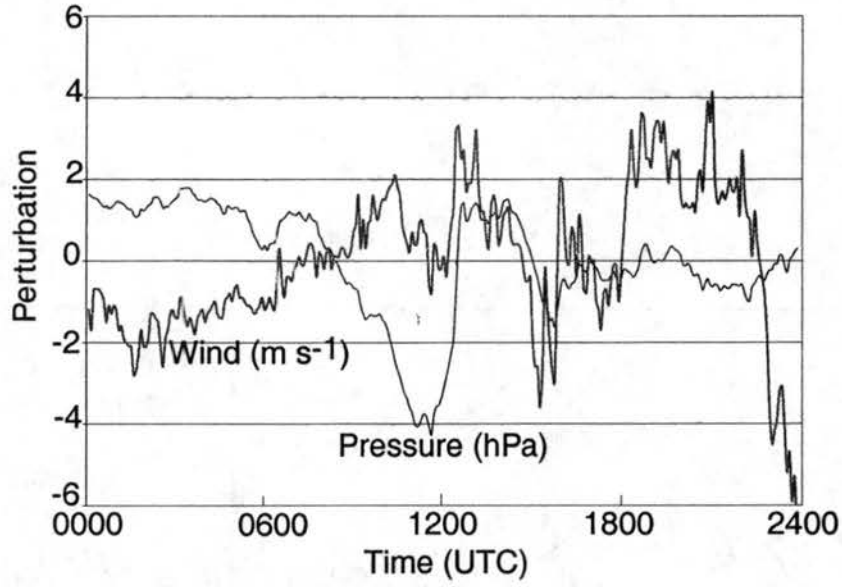

(a) ACME

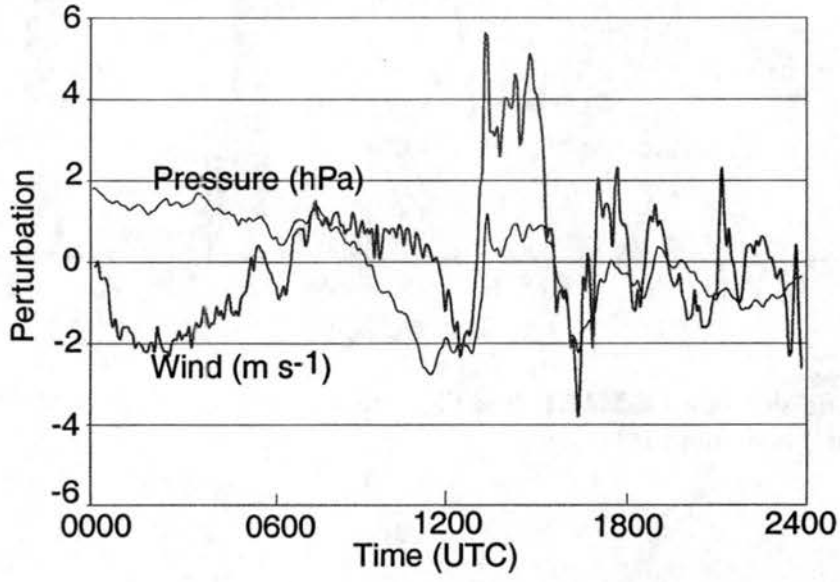

(b) WASH

Figure 4.12: Plot of pressure perturbations (black line) and wind perturbations (gray line) for (a) ACME and (b) WASH (see Fig. 4.8a for locations).

Such a pattern was not found in this case, perhaps partly because during the period of observations in Fig. 4.10, the stratiform region was moving very slowly. Neither does it appear to be a gravity current, which consists only of a mesohigh. A combination of the two, a gravity current/wave (Haertel et al. 2001), also consists of both a mesohigh and a wake low portion. The pressure field does not show such a couplet, but perhaps a portion of the mesohigh resided outside the Oklahoma mesonet. Another potential distinguishing factor between gravity waves and gravity currents is the way they advance. The leading edges of gravity current outflow are advected, while gravity wave outflow propagates due to horizontal convergence (Haertel et al. 2001). Unfortunately the difference between these two modes of propagation is indistinguishable in the dataset.

Another feature which seems to be associated with the leading mesolow is a heat burst (Johnson 1983). The station plot for CHEY (Fig. 4.13) shows evidence of a strong heat burst prior to stratiform rainfall commencing at 1230 UTC (not shown). From 1045 to 1125, the temperature rose 5.5°C, and the relative humidity fell 44%. Station pressure reached a minimum at 1120, having fallen 1.6 hPa. Similar surface changes due to heat bursts were reported by Johnson et al. (1989). Winds shifted from WSW to easterly and increased in speed from 5 to 9 m s^{-1} (not shown). Similar weaker features are seen at several stations. Analyzing the time and location of these heat bursts places them just ahead of the stratiform rain as seen by radar. This location supplies an explanation for a possible mechanism for the heat bursts. As air beneath the stratiform anvil is evaporatively cooled it becomes cooler than the surrounding air and sinks. As it sinks it is compressionally warmed. This sinking air gains momentum and can break through the stable layer, reaching the surface as a heat burst (Johnson 2001). This particular case appears to correspond well with the lateral inflow jet described by Bernstein and Johnson (1994). Although the heat bursts do not seem to progress in any one direction, they appear to correspond loosely with the location of the leading low. Eight of the eleven heat bursts occurred between 1100 and 1200 UTC.

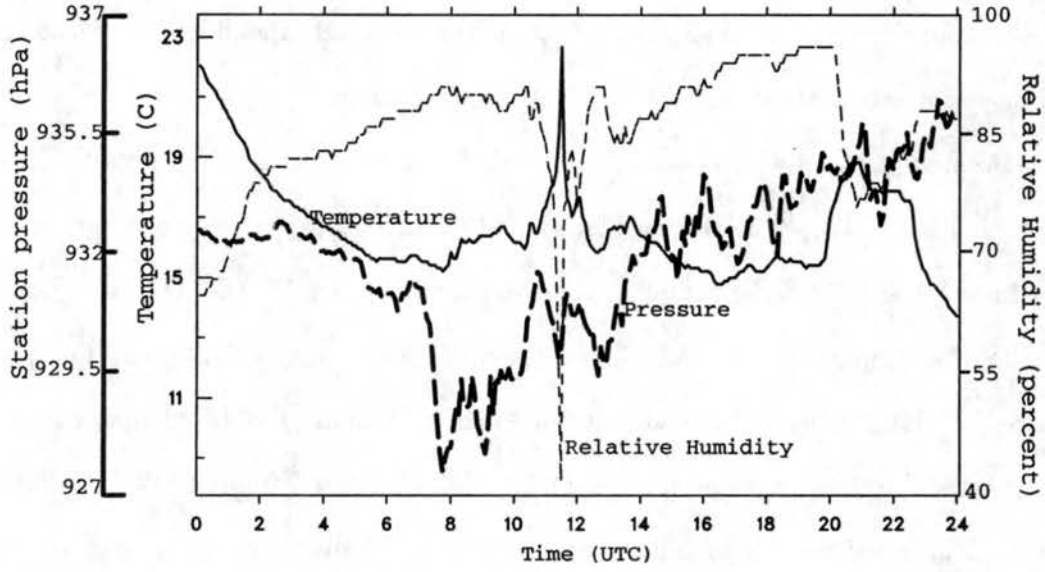

Figure 4.13: Station plot for CHEY (see Fig. 4.8a for location). Temperature (solid line) is in °C. Pressure (thick dashed line) is in hPa. Relative humidity (thin dashed line) is in percent.

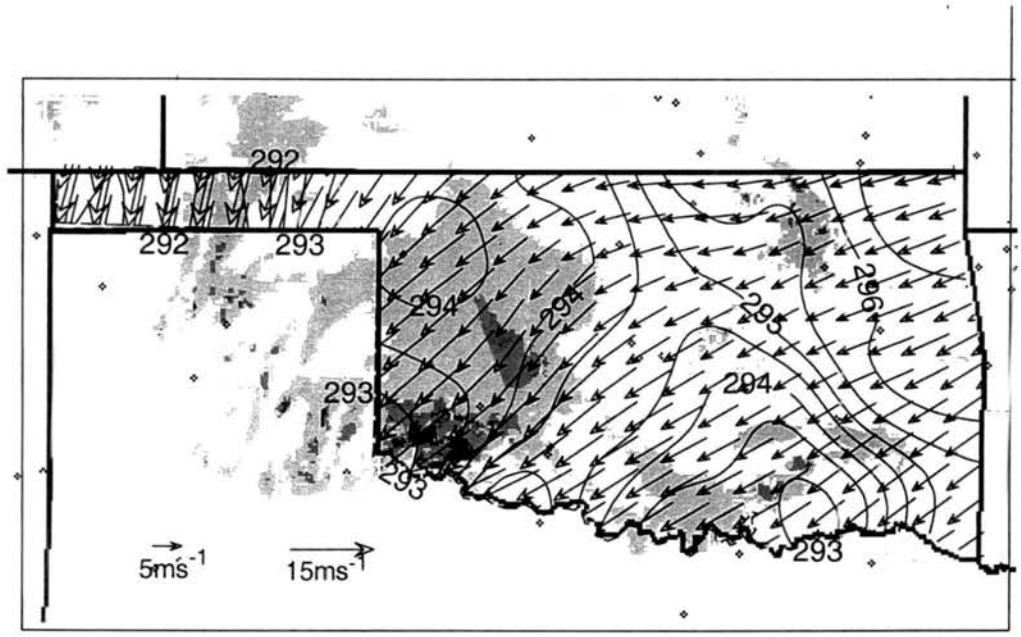

Figure 4.14: Potential temperature (contour interval 0.5 K) and storm-relative wind vectors at 1600 UTC 30 April 2000 over the Oklahoma mesonet. Radar reflectivity shaded as light shading = 20–39 dBZ, medium shading 40–49 dBZ, dark shading $\geq$ 50 dBZ.

Unfortunately the convective cells of the MCS were located over Texas (outside the Oklahoma mesonet) for the majority of the lifespan of the MCS, making it difficult to determine the existence of a mesohigh. It is possible, however, to detect a weak cold pool on the edge of the mesonet observation area in the southwestern corner of Oklahoma (Fig. 4.14). The potential temperature there was 293 K, while beneath the stratiform region it was between 293.5 and 294 K. Surface storm-relative winds can also be seen in Fig. 4.14, flowing from front-to-rear throughout the storm.

As mentioned earlier, the rainfall in this storm caused a significant amount of flooding. To further understand the rainfall pattern, an analysis was performed on the mesonet data to separate the total precipitation into convective portion and stratiform portion (Fig. 4.15). A threshold of 0.5 mm in 5 minutes was used (Johnson and Hamilton 1988). The stratiform rain accounts for a large percentage of the total rainfall in the northwestern and southcentral parts of Oklahoma. Over half of the precipitation at many stations in northwestern Oklahoma was stratiform. In the panhandle the stratiform precipitation totals

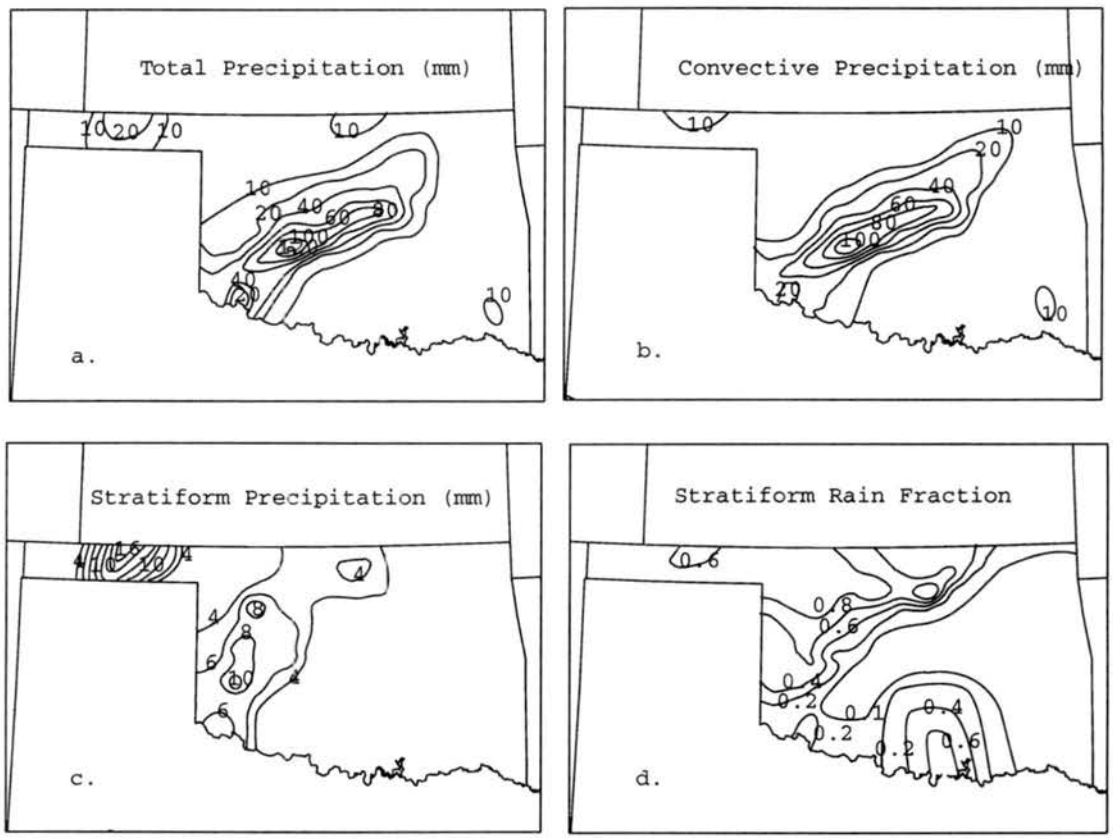

Figure 4.15: Precipitation retrieved from the Oklahoma mesonet for (a) storm total, (b) convective component, (c) stratiform component, and (d) fraction of the total rainfall due to the stratiform component.

were as high as 16 mm, while the maxima in the rest of Oklahoma did not exceed 9 to 10 mm. The stratiform precipitation totals as well as the stratiform rain fraction are similar to those for the TS system in Johnson and Hamilton (1988). The convective rainfall is greater in the LS storm, however, which undoubtedly played a role in the flooding that occurred. It is also possible that the order of the precipitation makes a difference. Although similar amounts of stratiform precipitation are seen in both cases, the stratiform rain in the LS moistens the ground prior to the arrival of the heavy rain, which may also assist in flooding.

The Oklahoma mesonet provided a great deal of insight into the surface features of the storm. Surface flow was front-to-rear throughout the system. A mesolow was evident just ahead of the stratiform rain area for a time, and its location seemed to coincide with

surface heat bursts. However, the movement of the mesolow, parallel to the northeast edge of the stratiform region, differed from the behavior of wake lows in TS systems. In TS systems a mesohigh/wake low couplet is seen to propagate with the stratiform region. In this case, a weak cold pool appeared near the convective cells, but no mesohigh was seen. Stratiform rain amounts were similar to those seen in TS systems, but the slow movement of the storm in addition to the moistening of the ground prior to the convective rainfall seemed to contribute to the flooding that occurred.

4.4. Vertical structure

Since Doppler radar data were unavailable for the 30 April LS MCS, wind profiler network data, as well as 40-km RUC analyses, were used to construct the vertical profile of the environmental flow. Although these data are coarse relative to Doppler radar data, they supplied the general vertical flow structure for this case.

A vertical cross section of θ_e (along line A-B in Fig. 4.8j) from the 40-km RUC at 1500 UTC can be seen in Fig. 4.16. A tongue of high-θ_e air can be seen between 850 and 800 hPa in the western part of the cross section (from behind the LS MCS). This might suggest convection in Oklahoma was elevated (Colman 1990; Trier and Parsons 1993) and fed from the rear. There is also a θ_e maximum at 850 hPa, collocated with the stratiform precipitation at this time. A stable layer can be seen from the surface up to this θ_e maximum.

A vertical cross section of the line-normal wind component of the flow along line A-B in Fig. 4.8j at 1500 UTC is shown in Fig. 4.17. This cross section is based on an objective analysis of winds from the profiler network. An extensive stratiform region had developed by 1500 UTC, making it more likely that the profiler network would be able to resolve some of the large-scale features of the LS. While large-scale features are resolved, the profiler data appear unable to resolve MCS-scale motions (this inadequacy will become more apparent in the next chapter, where analyses from Doppler and RUC fields are compared). Therefore, certain small-scale features, such as the low-level divergent flow near 97 W, are considered

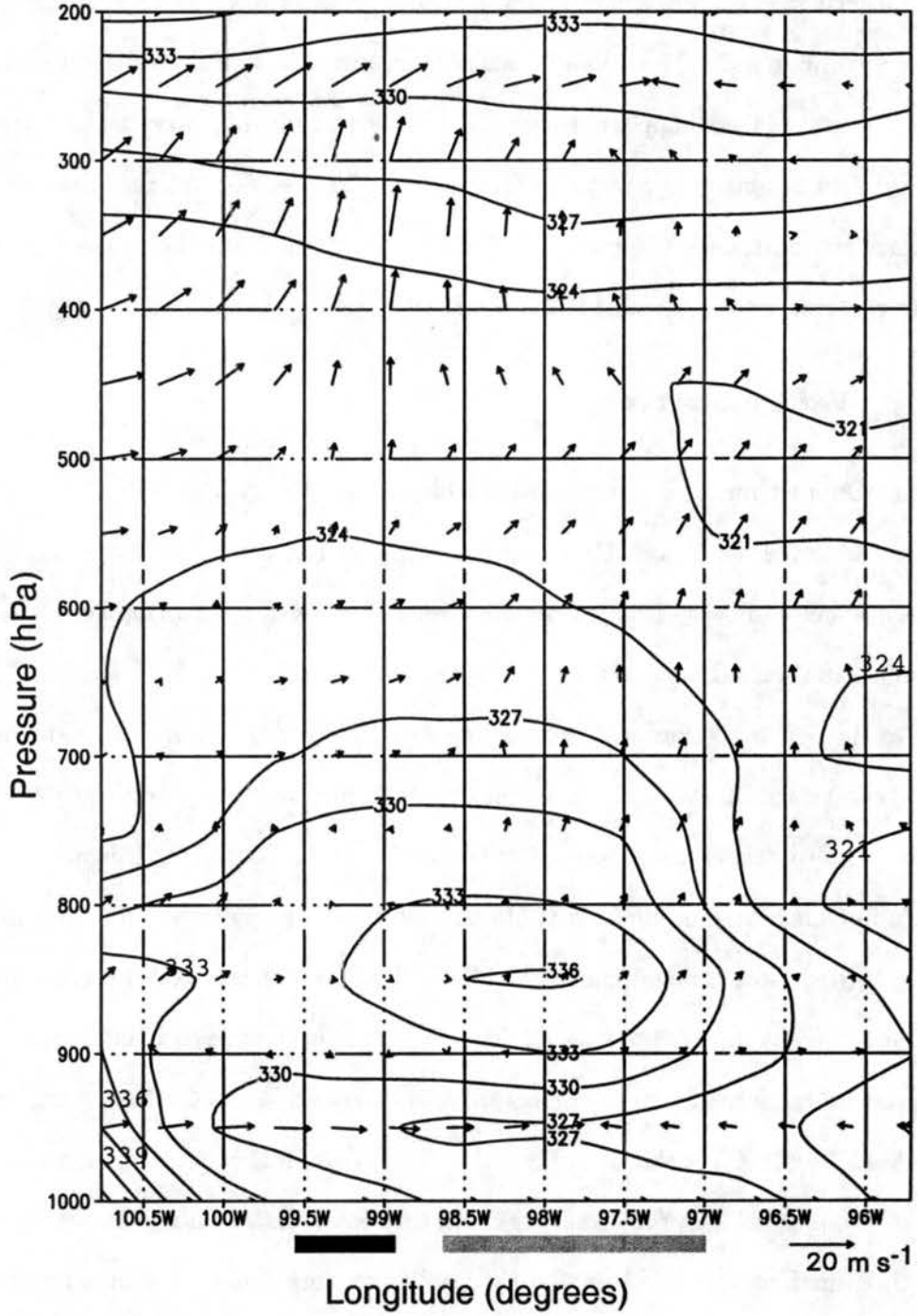

Figure 4.16: Vertical cross section of RUC equivalent potential temperature in K and storm-relative wind vectors at 1500 UTC along the line in Fig. 4.8j. Black bar indicates convective region, gray bar indicates stratiform region.

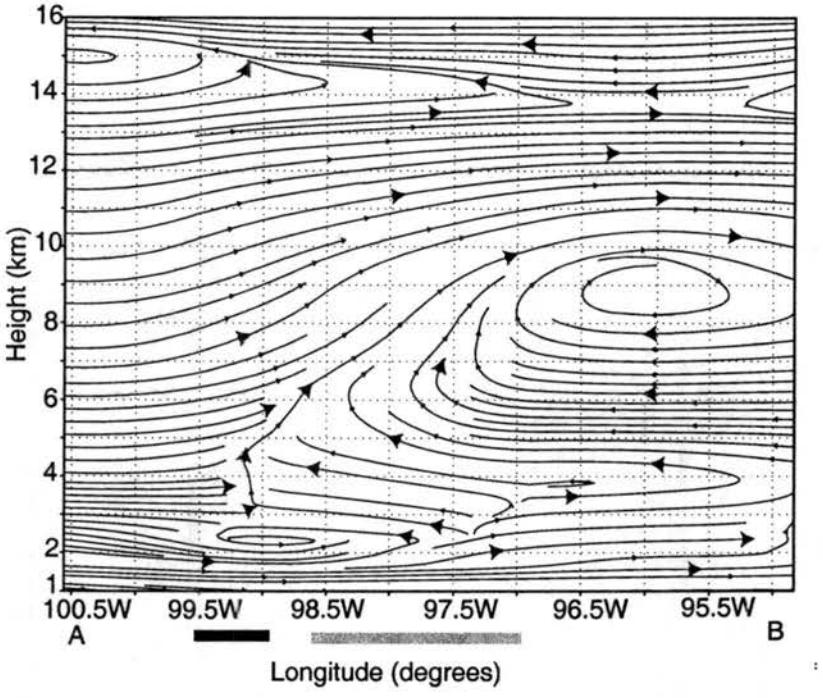

Figure 4.17: Vertical cross section of profiler-derived storm-relative streamlines along A-B in Fig. 4.8j for 1500 UTC. Black bar indicates convective region, gray bar indicates stratiform region.

unreliable.

The updraft in the convective line was fed from an elevated RTF flow (Fig. 4.17) that appears to be above the stable layer (Fig. 4.16). With the stratiform precipitation advancing ahead of the convective line, this rear inflow "feeds" the LS convective line high-θ_e air (Fig. 4.16) unmodified by rainfall evaporation. The updraft appears tilted downstream (Fig. 4.17), and air in upper levels moves from rear to front, rising in the convective area and sinking near and ahead of the stratiform rain (Fig. 4.18).

Ahead of the leading stratiform rain, air is flowing toward the storm at low- to mid-levels, some of which is sinking (Fig. 4.18). This air appears to reach the convective cells, but the profiler network cannot resolve such detail. Since flow at the surface is FTR throughout (Fig. 4.14), it is possible that this air passes underneath the convective cells at the surface. This feature appears to be a "leading inflow jet", similar to the TS rear inflow jet. It could

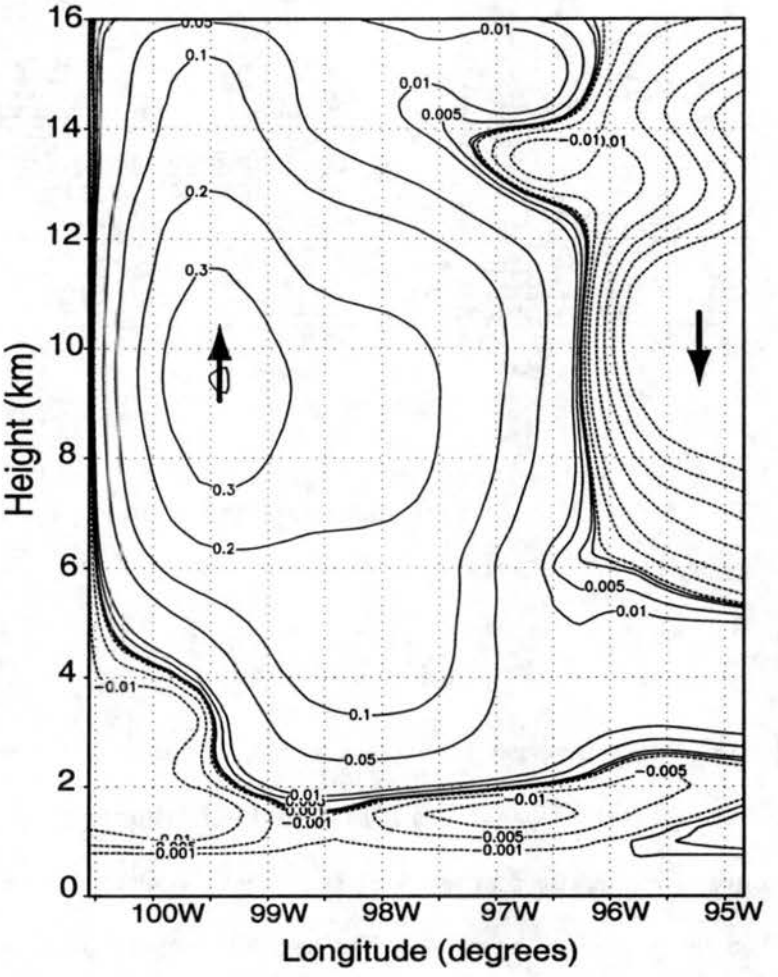

Figure 4.18: Average vertical velocity (m s^{-1}) derived from gridded wind profiler analysis along A-B in Fig. 4.8j for 1200–1500 UTC 30 April 2000. Dashed contours represent descending motion, solid contours represent ascending motion.

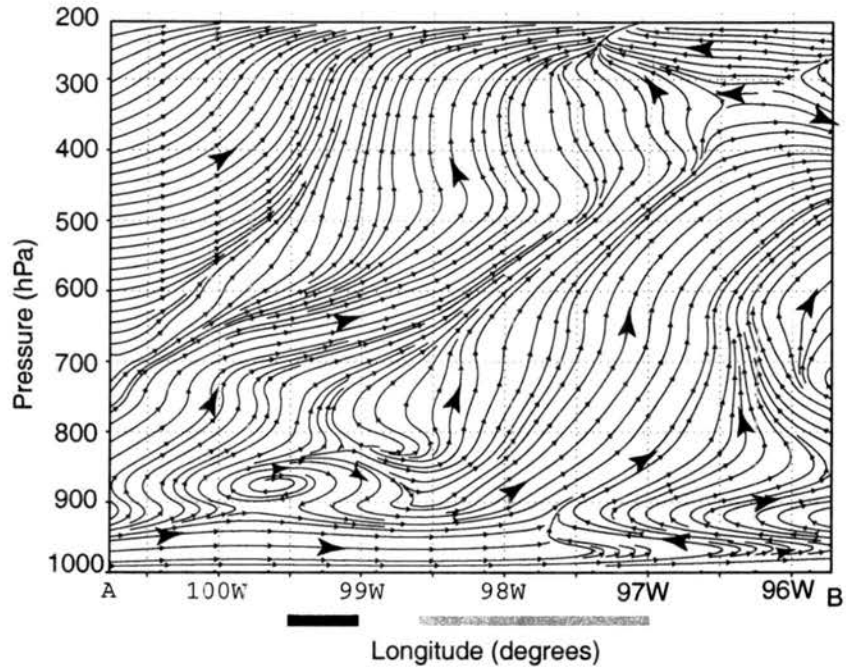

Figure 4.19: Vertical cross section of RUC derived storm-relative streamlines along A-B in Fig. 4.8j for 1500 UTC. Black bar indicates convective region, gray bar indicates stratiform region.

be responsible for heat bursts that occur ahead of and beneath the stratiform area in a manner similar to that described by Bernstein and Johnson (1994) and Johnson (2001).

RUC analysis data agrees with the profiler assessment somewhat. Vertical cross sections similar to those created with profiler data seem to capture less of the MCS-scale motion than the profiler data (Fig. 4.19). Upward motion is seen everywhere in the cross section, with no descent visible except in the location of the convection. A cross section of potential temperature overlaid with relative humidity contours and storm-relative wind vectors can be seen in Fig. 4.20. Evidence of the stationary front is visible on the west side of the cross section centered near 800 hPa. A cold pool of 294 K that may be connected with the MCS is seen in Fig. 4.20. Isentropic surfaces slant upward from west to east from 850 to 500 hPa, introducing the potential interaction between convective and frontal lifting (e.g., Colman 1990; Trier and Parsons 1993) and also the potential to enhance precipitation in the stratiform region.

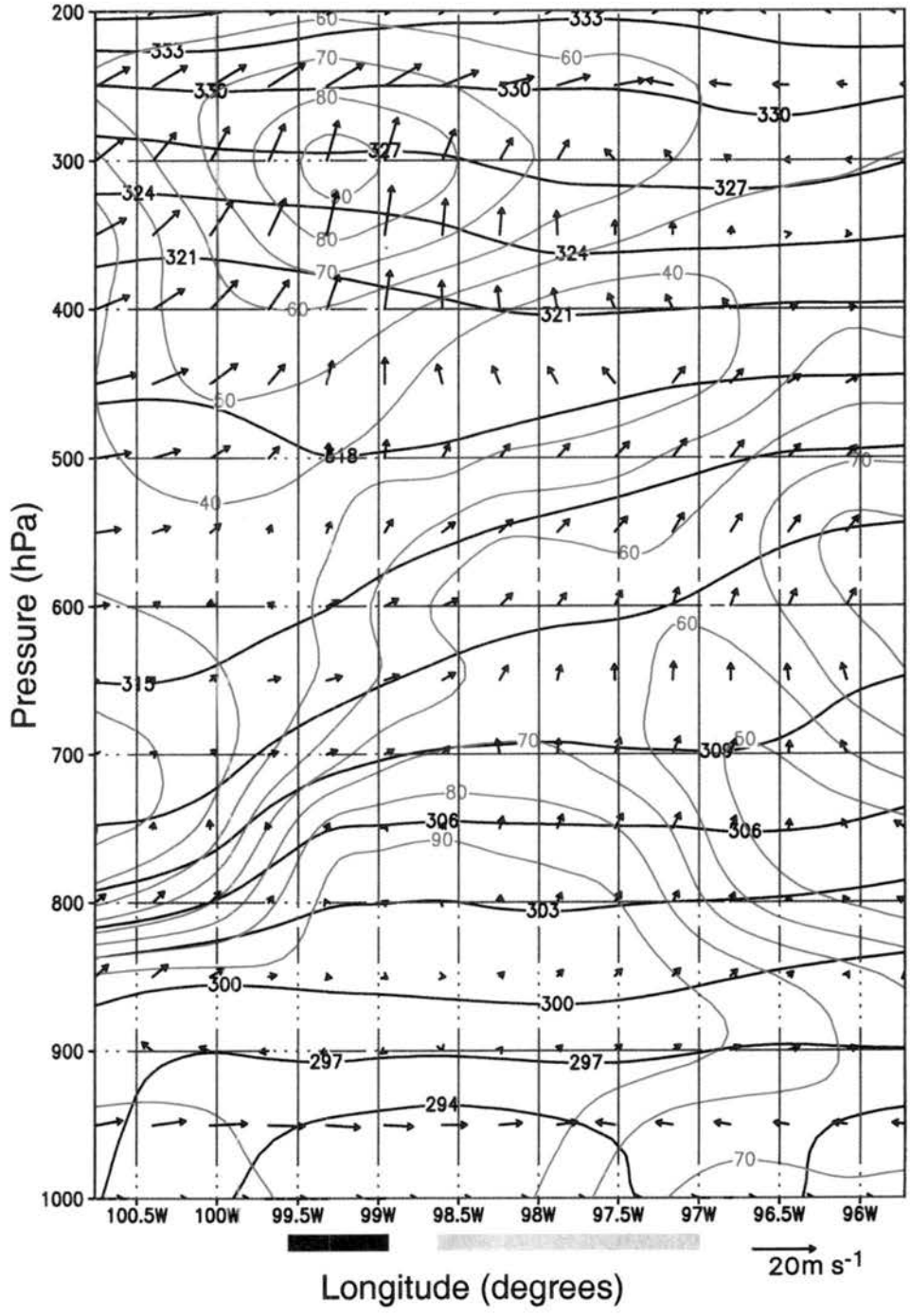

Figure 4.20: Vertical cross section of RUC potential temperature in K (black contours), relative humidity in percent (green contours), and storm-relative wind vectors (with 100*vertical motion) at 1500 UTC along the line in Fig. 4.8j. Black bar indicates convective region, gray bar indicates stratiform region.

This cross section has several similarities to an observational study by Fritsch et al. (1994), which showed the dynamical differences between typical TS structure and the structure they found. In a typical TS (e.g. front-fed), a relatively deep vertical circulation develops along an outflow boundary if the sign of the shear vorticity opposes the cold pool vorticity and the magnitudes of each are comparable (Rotunno et al. 1988). Like the 30 April LS, however, the Fritsch et al. (1994) storm was rear fed. In this situation the ambient shear vorticity and the cold pool vorticity have the same sign (Fig. 4.21). This causes lifting along the boundary to be relatively weak, and does not enable parcels to reach their level of free convection (LFC) along the boundary. In Fritsch's study, potential temperature surfaces sloped upward from the rear of the system into a mid-level vortex above the cold pool, causing air to ascend isentropically into the center of the vortex and initiate convection. Although a mid-level vortex has not been detected for 30 April, isentropic surfaces do slope upward from the rear (Fig. 4.20). Without adequate data, it is difficult to determine where convection was initiated with respect to the cold pool, but the possibility of weaker, non-linear forcing above the cold pool could help to explain the discontinuity of the convective line. However, unlike the case described by Fritsch et al. (1994), where convection occurred near the center of the cold pool, convection in our case is closer to the trailing edge of the cold pool.

Fig. 4.20 captures the elevated rear inflow and the ascending RTF flow. It does not show any indication of a descending leading inflow jet. The model does capture relative humidity greater than ninety percent below 780 hPa around the MCS, indicating the large quantity of low-level moisture available. Flow crossing isentropes toward higher θ indicates diabatic heating due to condensation and should have relative humidities near 100%. This produces greater relative humidity around 300 hPa in the western side of the cross section, however, the eastern portion of the cross section has relative humidity actually decreasing as the flow crosses isentropes toward higher potential temperature. This may be due to parameterized convection existing in an unsaturated environment in the model. While the

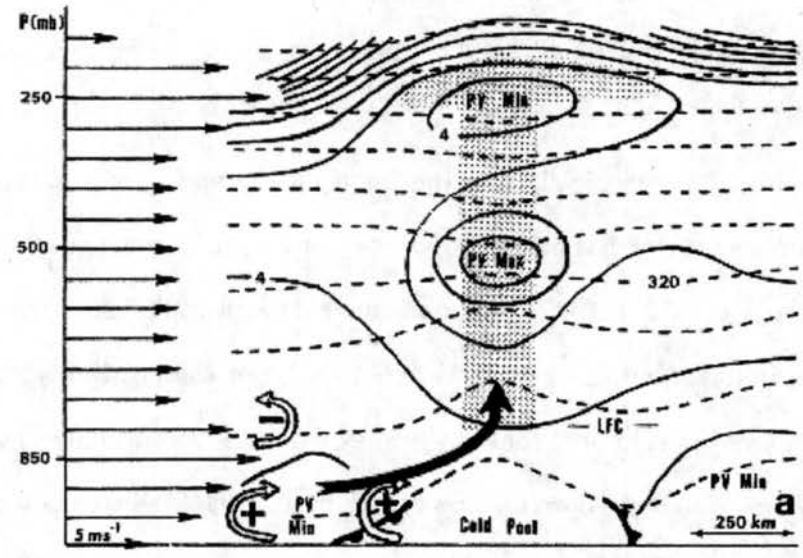

Figure 4.21: Fig. 29 from Fritsch et al. 1994. System is propagating left to right at about 5–8 m s^{-1} and shows the development of convection over the cold pool when shear vorticity and cold pool vorticity are of the same sign.

RUC captures some of the larger flow features, it is simply unable to resolve the mesoscale motions of this MCS.

An area average of vertical velocity and divergence from the RUC data over the stratiform rain region (reflectivities < 40 dBZ) at 1600 UTC displays the coarse resolution of the RUC data as well (Fig. 4.22). Although averaged only over the stratiform rain area, it produces a profile similar to one averaged over an entire MCS (Brandes 1990). There is strong divergence at upper levels, peaking at 250 hPa. There is also a layer of convergence from 925 hPa to 725 hPa. The profile of vertical motion shows a double peak, with one peak at 700 hPa and another at 350 hPa. This profile is suggestive of separate contributions by convective and stratiform components of the MCS, since convective vertical motion peaks near 700 hPa (Maddox 1983) while stratiform vertical motion peaks at upper levels. There are different possible reasons for this. The average was taken where the stratiform rain was observed, not where it was located in the model. It is possible that the model stratiform rain was shifted in some manner. Also with 40-km resolution the RUC should be able to resolve the stratiform rain, but it cannot resolve the convection. Therefore convection must be parameterized. It is possible that the area averaged may have contained both resolved stratiform rain as well as parameterized convection. One or both of these possibilities may have impacted the results.

In summary, vertical cross sections of gridded wind profiler data, as well as the RUC analyses, depict the vertical flow structure of the LS. A mid-level FTR flow that appears to be descending may be the mirror image of a TS system rear inflow jet. However, not all aspects of the flow are a mirror image. An elevated rear inflow exists which can "feed" the system high-θ_e air from behind. This slightly elevated RTF flow is different than what would be expected based on the archetype developed by Parker and Johnson (2000) (Fig. 2.5) which shows FTR storm-relative flow at this level from soundings taken ahead of the system. An ascending RTF flow aloft carries hydrometeors ahead of the convective line to form the stratiform region there, consistent with the Parker and Johnson (2000) model.

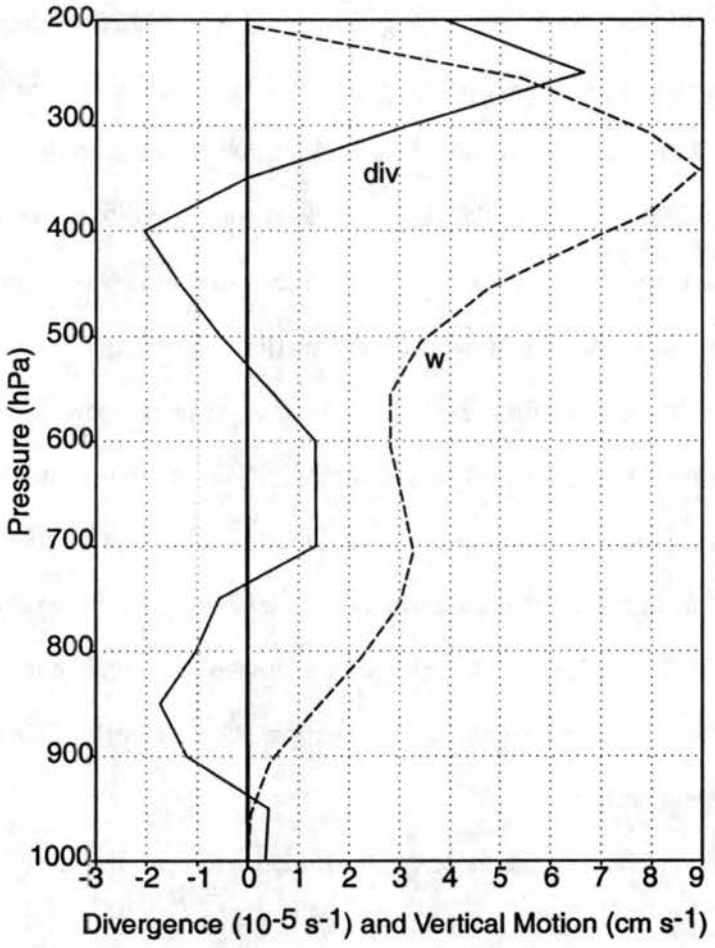

Figure 4.22: Area averaged vertical profile of vertical motion (dashed line) and divergence (solid line) from RUC data for the stratiform region at 1600 UTC.

Isentropic upglide introduces the potential for frontal lifting to initiate or prolong convection or enhance the stratiform region. A sharp frontal inversion caused by the quasi-stationary front decouples the surface flow (which was FTR throughout) from the elevated rear inflow.

4.5. Summary

In a broad sense, most features in the 30 April LS MCS appear as a mirror image of typical TS structure. In terms of horizontal reflectivity structure, cells in the convective line are canted in a similar manner to TS systems. As the LS system progresses, it develops a transition zone of lower reflectivity and an enhanced stratiform rain region. Oklahoma mesonet data show evidence of a cold pool beneath the convective cells. They also show a leading mesolow, which in some ways resembles a TS wake low. Heat bursts, features that have been associated with several TS systems, are evident at several stations. Stratiform rain totals are similar to those measured in TS storms. Some features associated with vertical structure are similar as well. A leading inflow jet exists which could be the equivalent of a TS rear inflow jet. There is also strong rising RTF flow aloft blowing hydrometeors downstream, the exact opposite of a TS system.

Although many features are similar, there are also several differences. The convective line in this LS system is more discontinuous. Although convective cells are oriented in a similar manner, the cells are elongated more than in a typical TS. Another distinctive difference found in the mesonet data is the surface flow in the LS. A TS rear inflow jet usually reverses when it reaches the convective core, with the jet flow being RTF but the surface flow below being FTR in a storm-relative sense. In this LS, however, the leading inflow jet and the surface flow are both FTR. It is possible that the jet flow descends and reverses atop the FTR surface flow as it reaches the convective region, but it is difficult to determine from the coarse profiler data. Unlike TS systems that are typically fed from the boundary layer, the convective line of this LS is fed by an elevated rear inflow of enhanced θ_e from behind the system. This inflow is decoupled from a reversed surface flow. The back-

building nature of cells in the convective line is consistent with this RTF flow of high-θ_e air.

Chapter 5

CASE II: A RAPIDLY MOVING LS MCS OVER SOUTH DAKOTA, MINNESOTA, AND IOWA

On 7 May 1997 an MCS formed over South Dakota and moved across the states of Minnesota and Iowa. The system moved more rapidly than the 30 April LS (15 m s^{-1} compared to 9 m s^{-1}) and did not produce flooding. It did, however, pass directly over the Sioux Falls, South Dakota WSR-88D, providing high resolution Doppler radar data to analyze.

5.1. Synoptic environment

The upper level flow pattern at 1200 UTC on 7 May 1997 was dominated by a ridge over the central United States (Fig. 5.1). A trough was located over New England, with another trough stretching through Montana and Wyoming. The South Dakota–Minnesota–Iowa border was located in the right entrance region of a jet streak (Fig. 5.2), enhancing the potential for convection in that area.

A sequence of surface maps is shown in Fig. 5.3. There was a surface low near Valentine, Nebraska at 0900 UTC (Fig. 5.3a). A trough line extended south-southwestward from the low. A warm front stretched from the low east-southeastward until it ran parallel with the Iowa–Nebraska border. The convective line with a N–S orientation was initiated north of the front. A more detailed description of the radar reflectivity evolution will be given later. At 1200 UTC (Fig. 5.3b) the low moved ENE, just over the border in South Dakota. The trough line was oriented N–S. The warm front paralleled the Nebraska–South

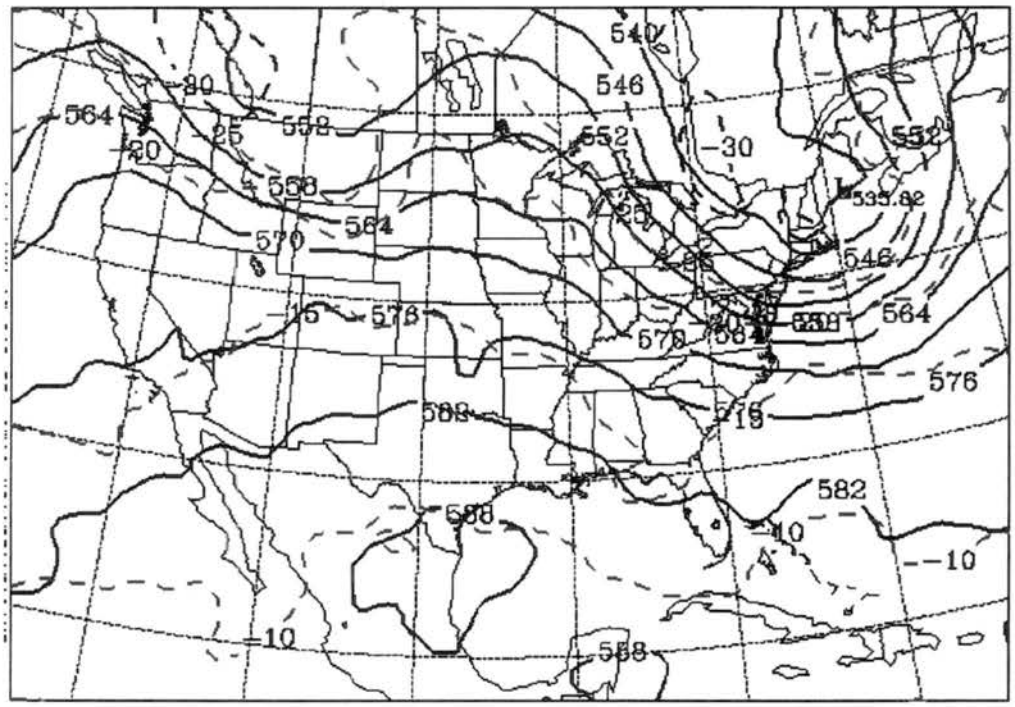

Figure 5.1: 500 hPa heights (dm) and temperatures (°C) from EDAS.

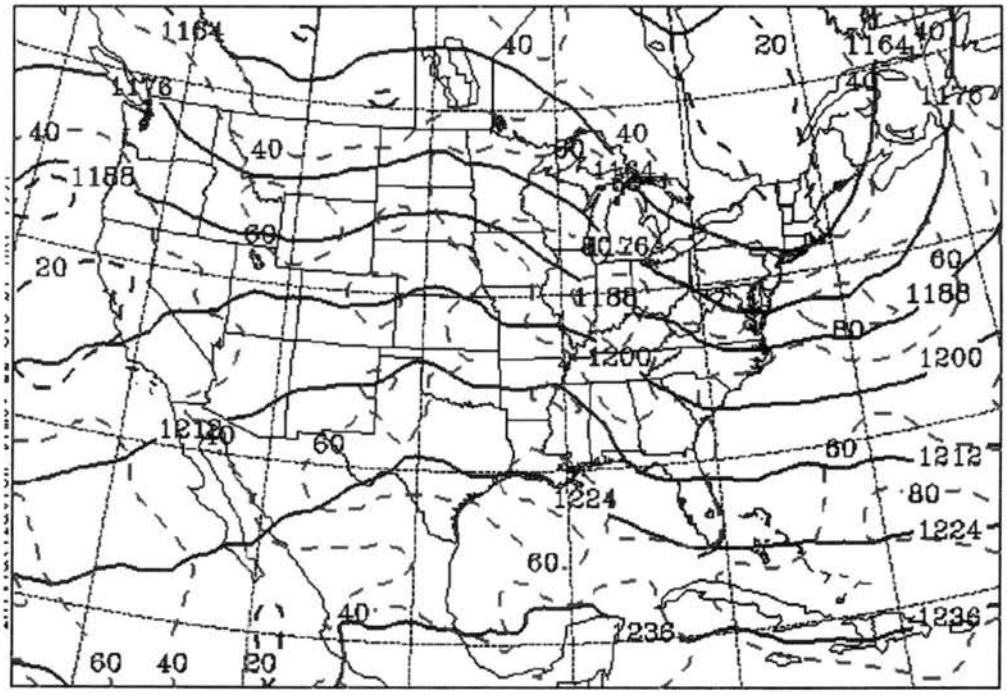

Figure 5.2: 200 hPa heights (dm) and wind speeds (kts) from EDAS.

Dakota and Nebraska–Iowa borders. A significant stratiform rain area developed ahead (east) of the convective line, which paralleled the Iowa–South Dakota border.

The low moved farther ENE by 1500 UTC (Fig. 5.3c). The warm front stretched SSE and the trough line followed it. By this time, the convective line had collapsed to a few cells and was parallel to the warm front, with an enhanced and extensive stratiform rain region ahead of it. By 1800 UTC (Fig. 5.3d) the low was just west of Sioux Falls, South Dakota. The warm front moved into Iowa, still leading the trough line. The convective line moved farther from the front.

Soundings were taken west of (behind) the formation of the MCS. Nearby soundings at OAX (Fig. 5.4a) and ABR (Fig. 5.4b) show nearly saturated conditions from 800 to 500 hPa and significant temperature inversions at the surface. These inversions are a reflection of the warm front (Fig. 5.3b). Surface parcels have no bouyancy in either sounding, therefore any convection that formed must have been elevated. Wind speeds and directions from these soundings show southwesterly to westerly flow above 900 hPa. This flow could have blown the warm, moist mid-level air ahead of the warm front and into the cooler air mass to spark elevated convection.

An 800 hPa cross section of 60-km RUC θ_e at 1200 UTC is shown in Fig. 5.5. A maximum of 333 K was located west of (behind) the LS. This is consistent with the sounding data and could provide the means for elevated convection to develop.

The synoptic situation of 7 May 1997 presents some similar conditions to that of 30 April 2000. There is an elevated θ_e maximum behind (west of) the LS convective cells. Soundings show weak southwesterly to westerly storm-relative flow above 900 hPa, indicating the potential for the LS convective cells to tap into the enhanced θ_e air. There is a saturated layer from 800 to 500 hPa, providing moisture for the system. The LS forms northeast of a warm front, which may be providing synoptic-scale lifting for the storm (Colman 1990; Trier and Parsons 1993). This will be discussed in more detail in Section 5.3.

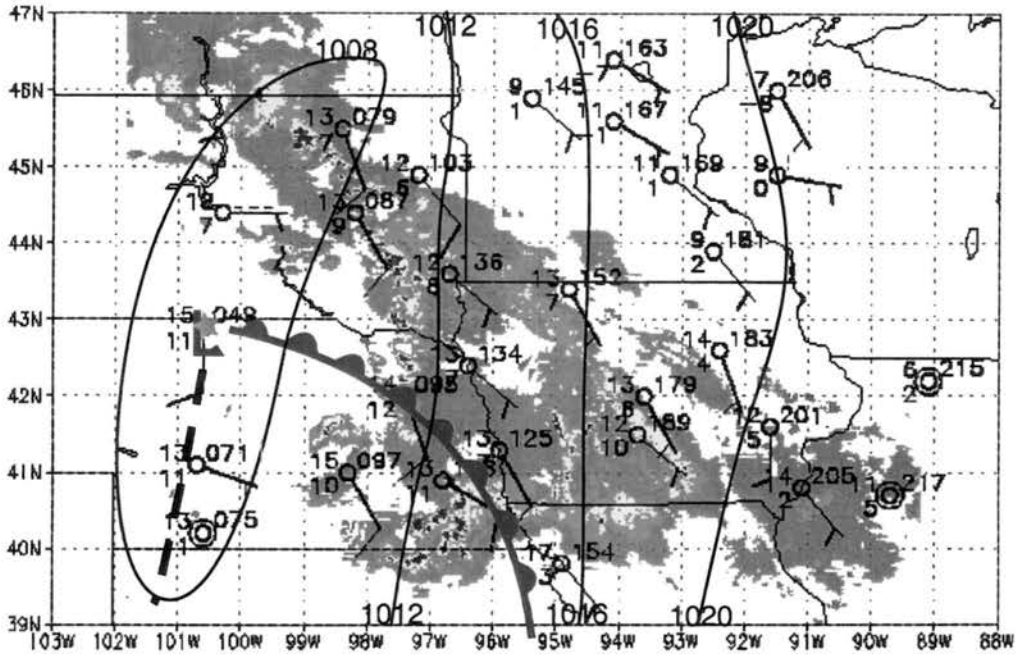

(a) 0900 UTC

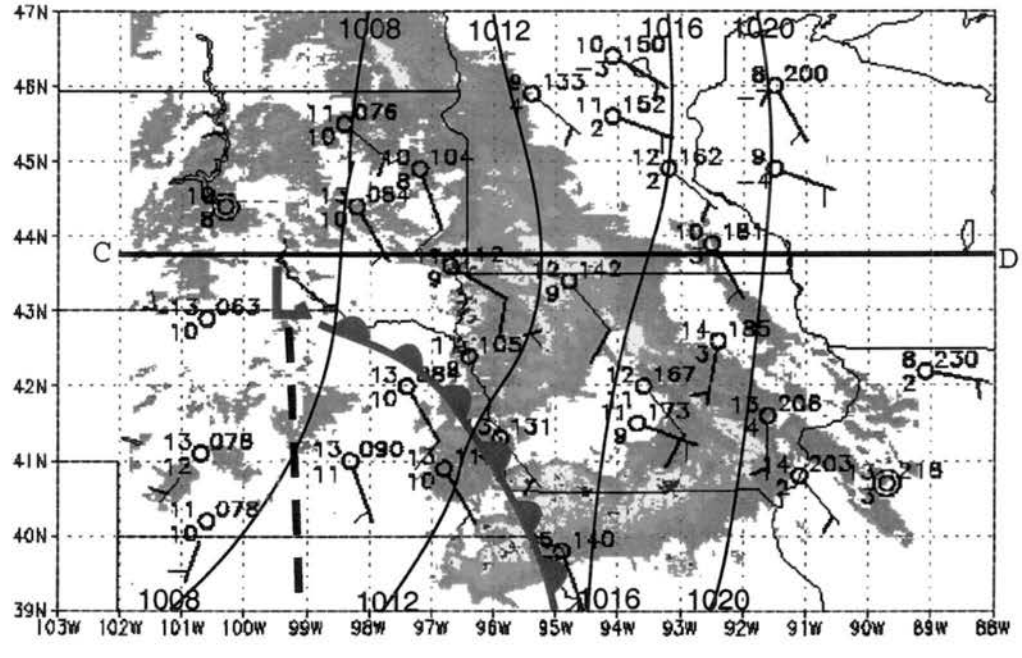

(b) 1200 UTC

Figure 5.3: Surface analyses for (a) 0900 UTC, (b) 1200 UTC, (c) 1500 UTC, and (d) 1800 UTC. Reflectivities are shaded as in Fig. 4.4. Line C-D in (b) is used for Figs. 5.11 and 5.12. Pink star indicates location of (a) Valentine, Nebraska, and (d) Sioux Falls, South Dakota. Pressure is contoured every 4 hPa.

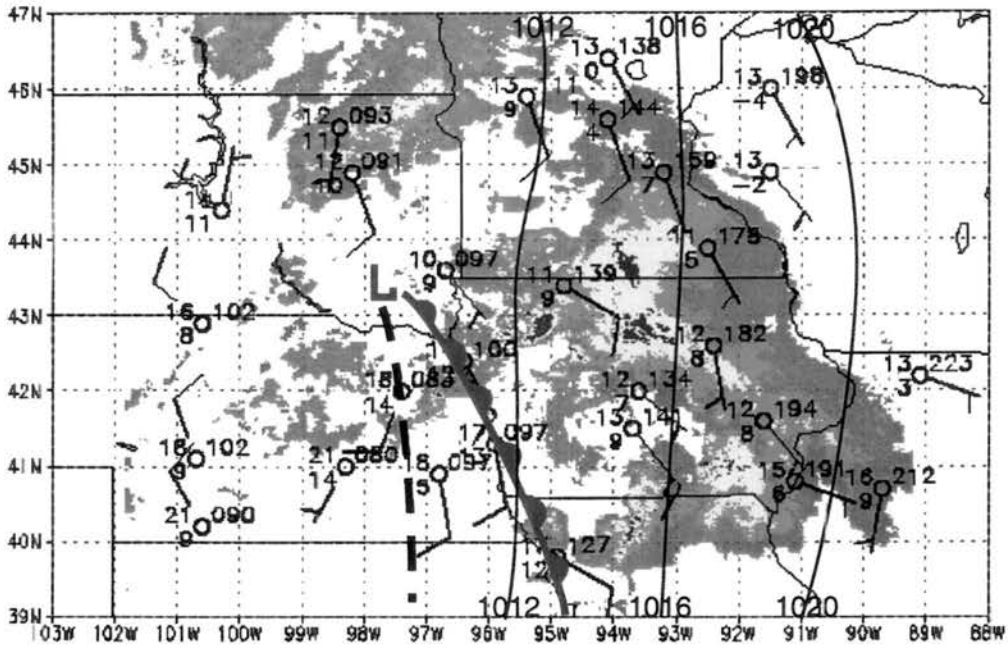

(c) 1500 UTC

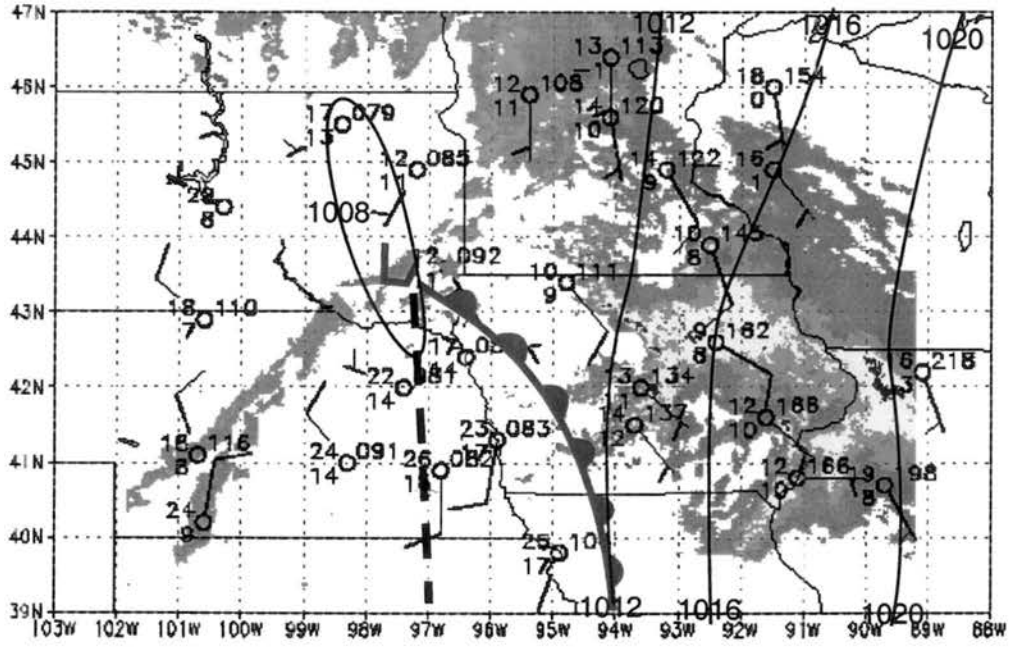

(d) 1800 UTC

Figure 5.3: *Continued*

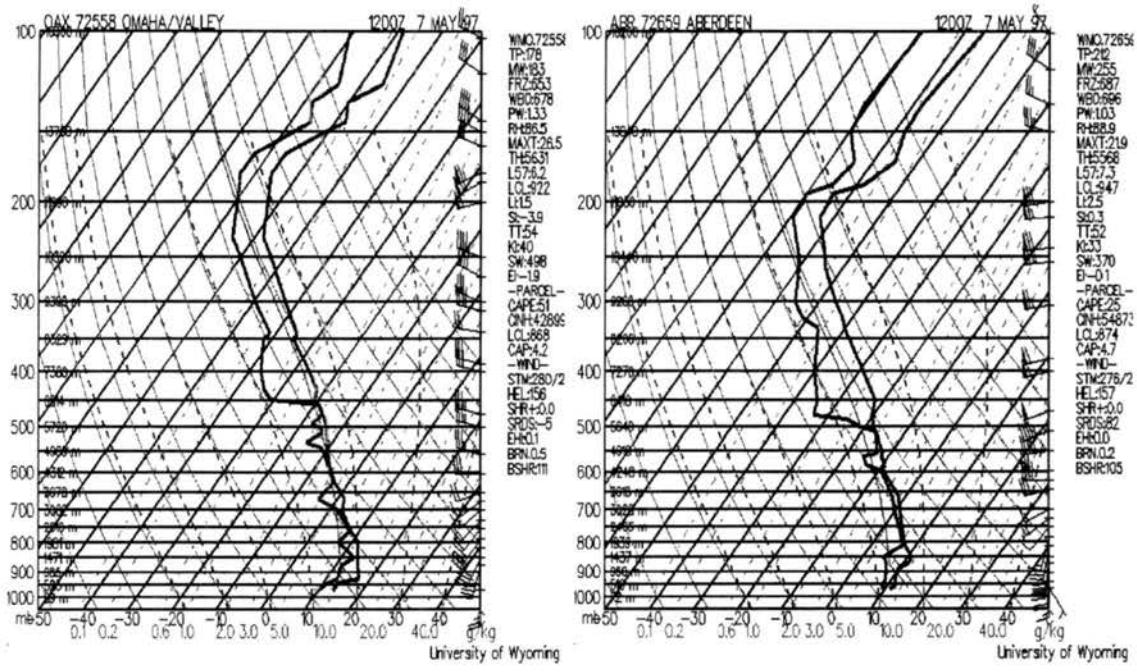

(a) Omaha, NE

(b) Aberdeen, SD

Figure 5.4: 1200 UTC soundings from (a) Omaha, Nebraska and (b) Aberdeen, South Dakota on 7 May 1997. Locations are shown in Fig. 5.6g.

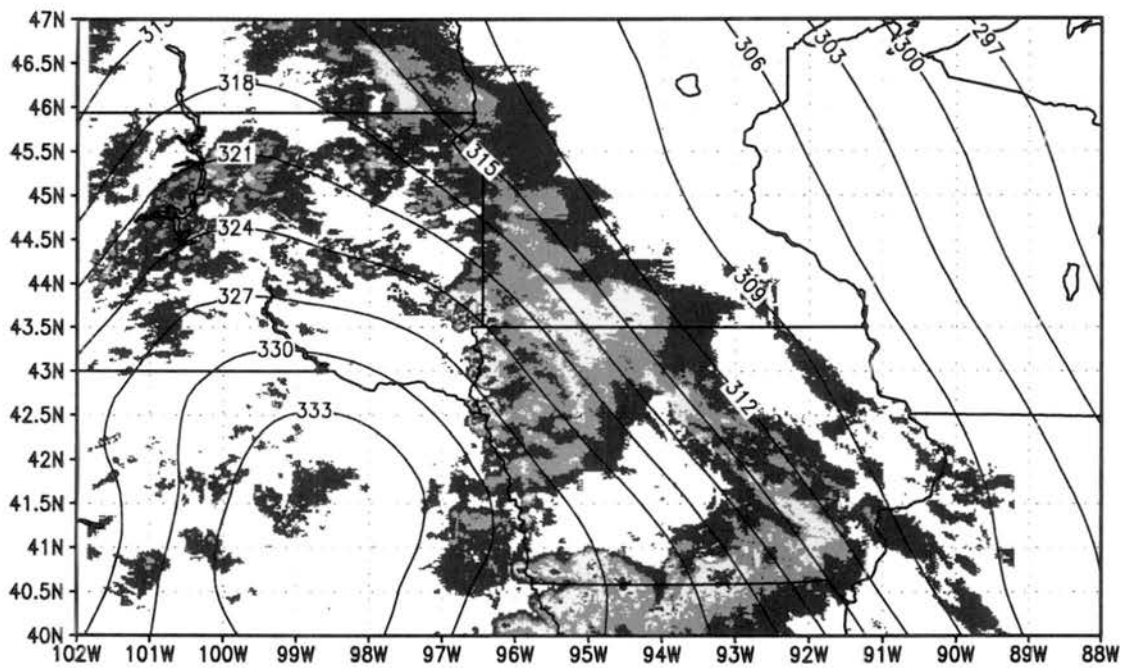

Figure 5.5: 800 hPa cross section of RUC θ_e (contoured every 3 K) at 1200 UTC.

5.2. Horizontal structure and system evolution

A look at the overall evolution of the storm can be seen in Fig. 5.6. The first few convective cells in the formative LS MCS were visible at 0600 UTC (Fig. 5.6a) in the southeastern corner of South Dakota. They formed along a NW–SE line until 0800 UTC (Fig. 5.6c), when a more N–S orientation began to develop. A stratiform region expanded rapidly after 0700 UTC and was extensive by 1100 UTC (Fig. 5.6f). A region of enhanced stratiform reflectivity formed well ahead of the convective line at 1200 UTC (Fig. 5.6g). This enhanced stratiform region continued throughout the storm's lifetime, separated from the convective line by a region of lower reflectivity–a transition zone similar to those seen in TS systems (Smull and Houze 1985). The convective line orientation shifted to NNW–SSE at 1300 UTC (Fig. 5.6h). From 1300–1500 UTC (Figs. 5.6h, i, and j), the convective line shrank down to one large convective cell. The line reformed by 1600 UTC (Fig. 5.6k). By 1900 UTC (Fig. 5.6n) the system became more disorganized and moved out of the area by 2100 UTC (Fig. 5.6p).

The convective cells of the MCS were very discontinuous. Some were elongated perpendicular to the line (Fig. 5.6e), while others were elongated at an angle slightly off perpendicular (Figs. 5.6f and g). This is similar to the 30 April case, and also to TS MCSs (Houze et al. 1990).

The visible satellite image at 1415 UTC provides another view of the storm structure (Fig. 5.7). The satellite image shows the convective cells on the western edge of the system. In addition, there is evidence of lines of developing cells farther to the west. A cirrus cloud shield extends downstream (east) of the convection.

The horizontal structure of the 7 May 1997 LS shows significant discontinuity in the convective line. The individual cells are elongated and sometimes canted at a 60 to 90° angle to the convective line. The convective line itself evolves significantly. The line orientation goes from NW–SE, to N–S, then to NNW–SSE. It consists of several convective cells during the beginning of its lifecycle, evolves to only one large cell, and continues back to multiple

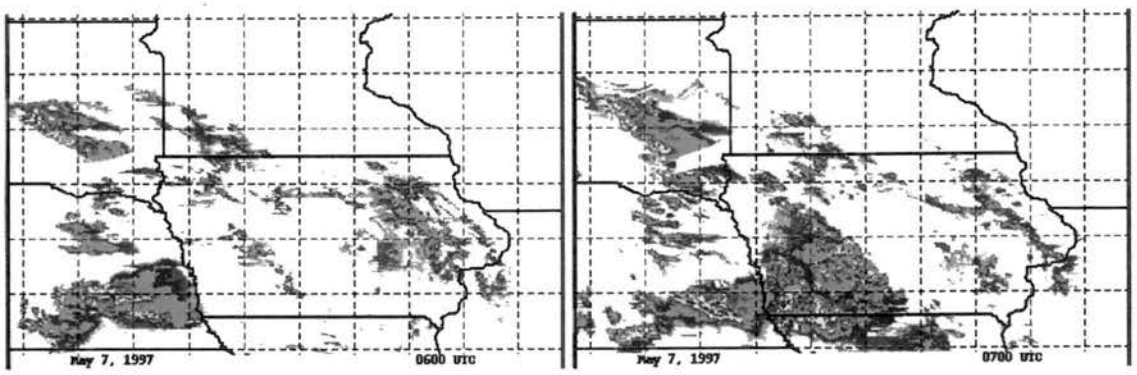

(a) 0600 UTC

(b) 0700 UTC

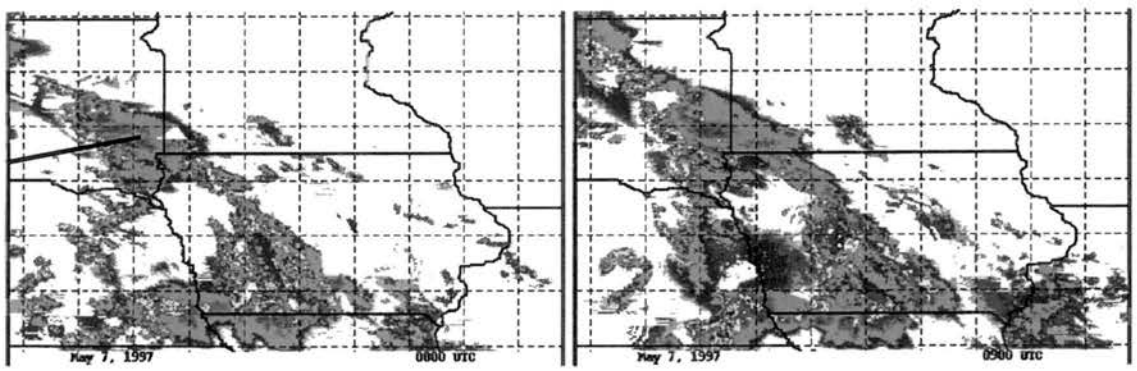

(c) 0800 UTC

(d) 0900 UTC

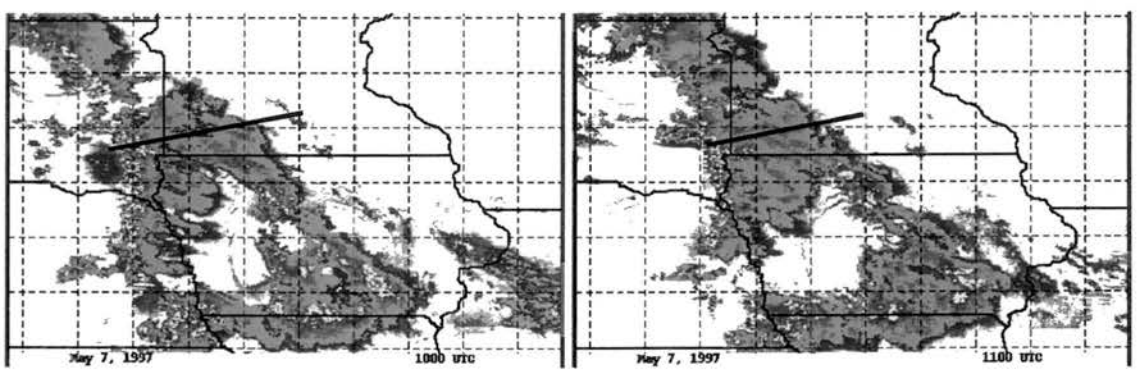

(e) 1000 UTC

(f) 1100 UTC

Figure 5.6: Radar reflectivity for 0700–2100 UTC for 7 May 1997. In (g), stars indicate the locations of sounding sites. Pink = Aberdeen, South Dakota, purple = Omaha, Nebraska.

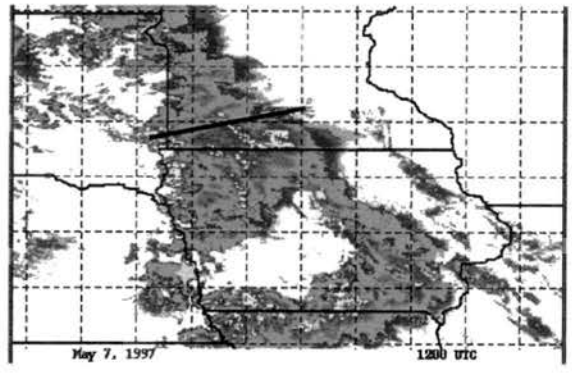

(g) 1200 UTC

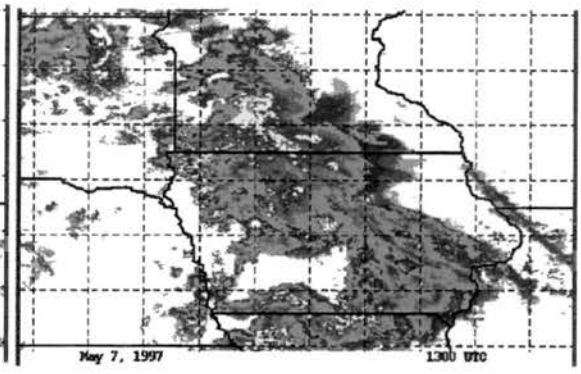

(h) 1300 UTC

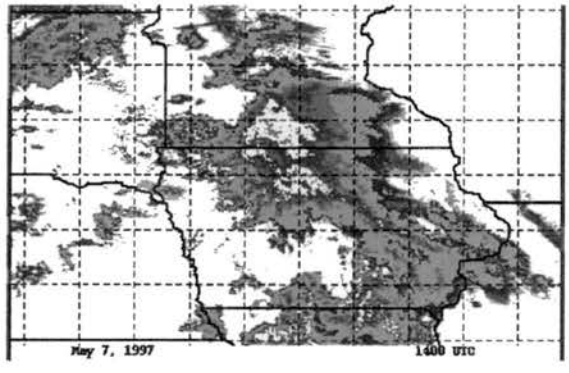

(i) 1400 UTC

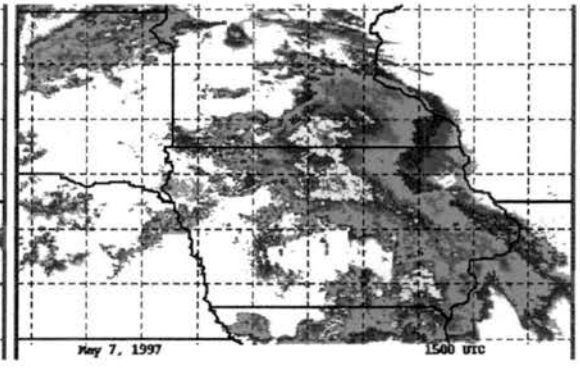

(j) 1500 UTC

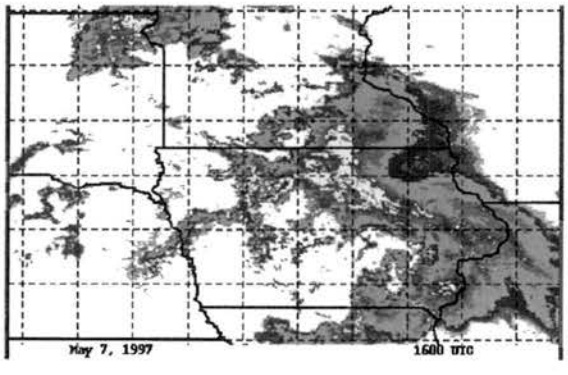

(k) 1600 UTC

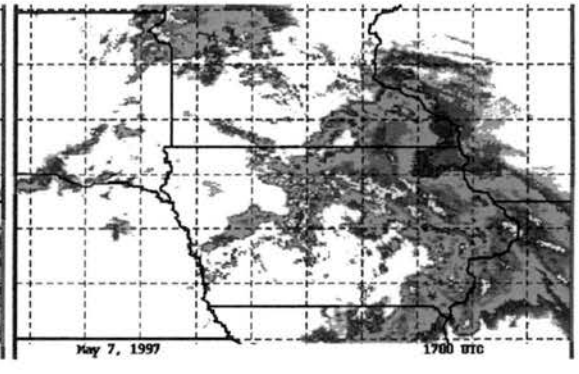

(l) 1700 UTC

Figure 5.6: *Continued*

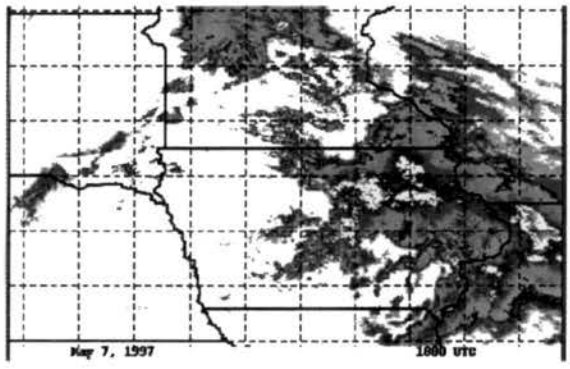

(m) 1800 UTC

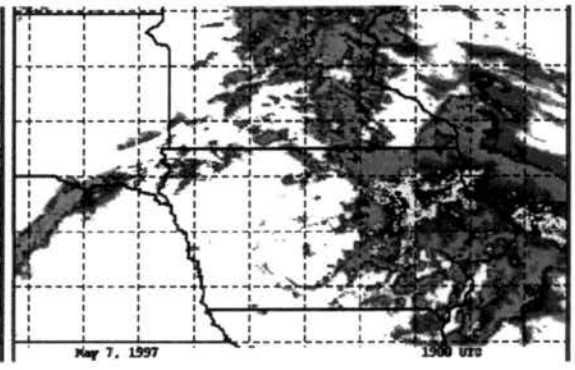

(n) 1900 UTC

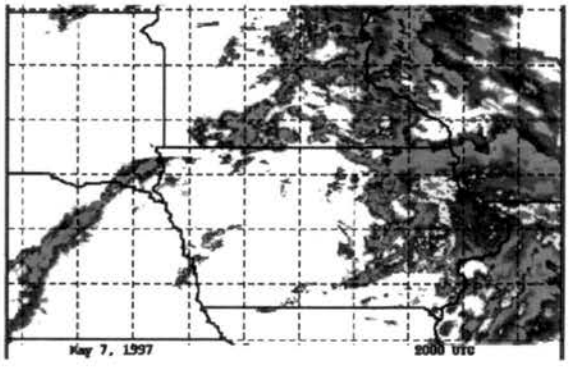

(o) 2000 UTC

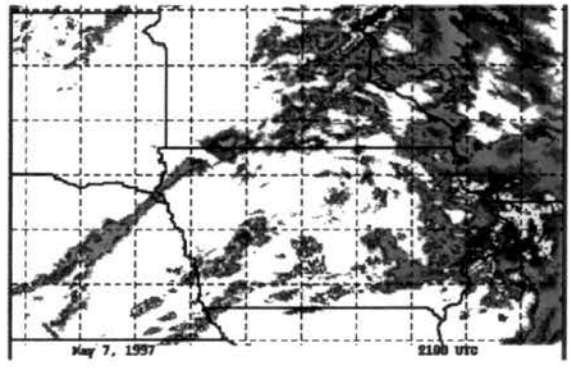

(p) 2100 UTC

Figure 5.6: *Continued*

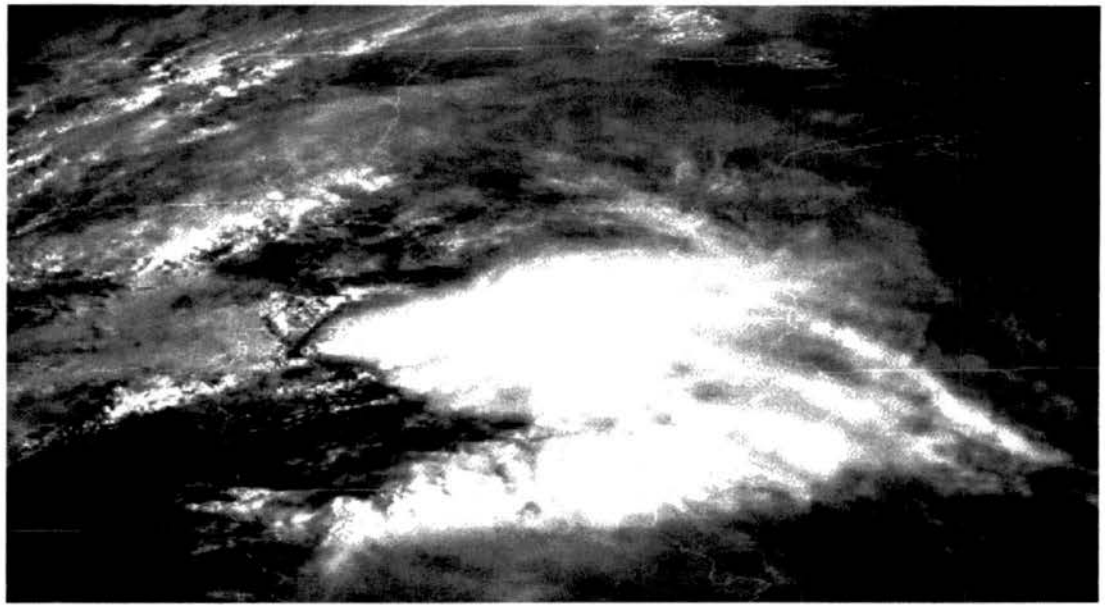

Figure 5.7: Visible satellite image over northern Midwest at 1415 UTC.

cells. The stratiform rain area becomes enhanced, with a transition zone of lower reflectivity separating it from the convective line. Using Parker and Johnson's (2000) conditions for LS determination, the overall lifespan of the system was 12 hours (0700–1900 UTC), 5.2 hours longer than the average for an LS system.

5.3. Vertical structure

Doppler radar data from the WSR-88D in Sioux Falls, South Dakota, were available for the 7 May LS. An analysis of this dataset provides the vertical structure of the storm at a much higher resolution than the 30 April case. Unfortunately three hours of data, from 0742 to 1031 UTC, were missing from the dataset. Prior to 0700 the LS had formed very little stratiform rain, and was farther from the radar site. After around 1300 UTC most of the system (especially its stratiform elements), was out of the range of the radar. With these constraints, four vertical cross sections are taken along the direction of motion using IDL to show the evolution of the system. Cross sections are averaged over a ten minute period (3 scans) to reduce noise. Radial velocities are storm relative, with a storm motion vector of 15 m s^{-1} toward 82° used to determine storm-relative flow.

At 0733 UTC the system was beginning to produce stratiform rain (Fig. 5.8a). Flow patterns were beginning to develop characterized by FTR flow at low levels and RTF flow at mid-to-upper levels. Flow behind the system at low-to-mid levels was indeterminable because of the height of the lowest scan 80 km from the radar. At 1036 UTC convection was directly overhead of the radar (Fig. 5.8b). Rising RTF flow was seen atop FTR flow. Elevated rear inflow can be seen as low as 2 km AGL, representing flow atop the inversions in Fig. 5.4. This elevated inflow allowed the MCS to tap into the elevated θ_e maximum found in the air mass behind (to the west of) it (Fig. 5.11). A large leading anvil was developing at this time.

At 1126 UTC the convection moved east of the radar (Fig. 5.8c). An elevated rear inflow was evident, but was higher than at 1036 UTC. The FTR flow was now descending

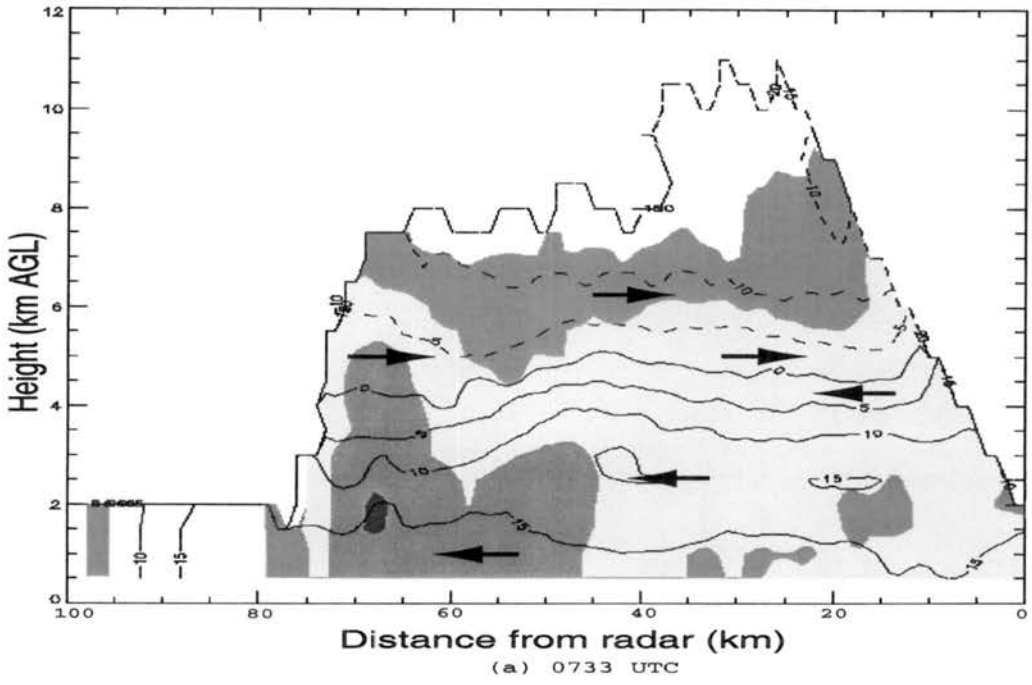

Figure 5.8: Average vertical cross section of radar reflectivity and storm-relative flow (m s^{-1}) from (a) 0733 (along line in Fig. 5.6c), (b) 1036 (along line in Fig. 5.6e), (c) 1126 (along line in Fig. 5.6f), and (d) 1226 UTC (along line in Fig. 5.6g) on 7 May 1997. Reflectivities are shaded in 10 dBZ increments, green = 10–20 dBZ, yellow = 20–30dBZ, orange = 30–40 dBZ, red = 40–50 dBZ. Solid contours are away from the radar, dashed contours are toward the radar in m s^{-1}.

and was located below 5 km, with ascending RTF flow above it. An enhanced stratiform region had formed, and a transition zone (Smull and Houze 1985) of lower reflectivity centered around 40 km separated it from the convective core. At 1226 UTC a descending FTR inflow extended to near the surface topped by an ascending RTF flow carrying hydrometeors ahead of the convective line (Fig. 5.8d). An elevated rear inflow can be seen around 3 km AGL, closer to the level at 1036 UTC. Most of these features seen in the radar cross sections are consistent with the 30 April case, however, there was not RTF flow at low levels seen in the radar data for 7 May. This may indicate that aspect of the 30 April flow was a result of interpolation for the low resolution datasets and not a real feature.

Vertical cross sections of radar reflectivity from radial coordinates using WATADS were taken to get a sharper picture of the reflectivity structure since gridding tends to

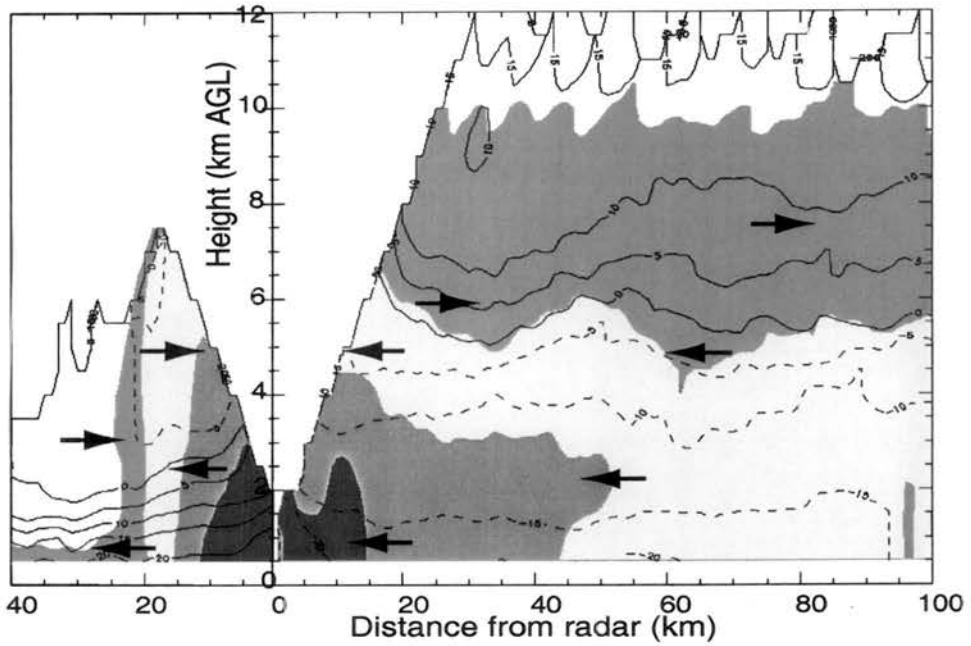

(b) 1036 UTC

Figure 5.8: *Continued*

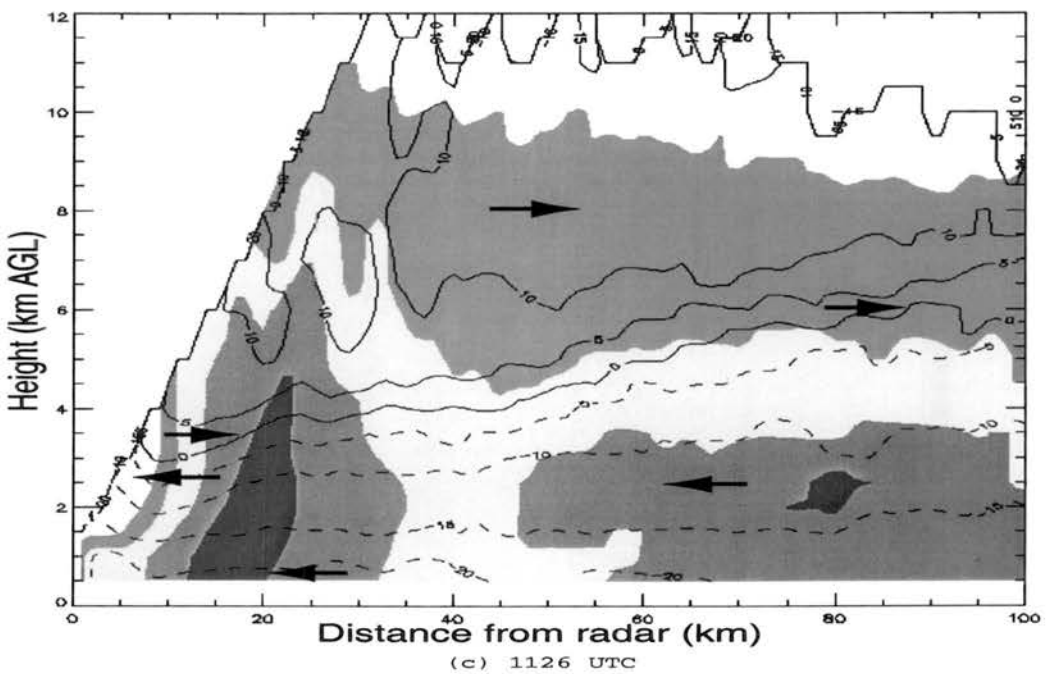

(c) 1126 UTC

Figure 5.8: *Continued*

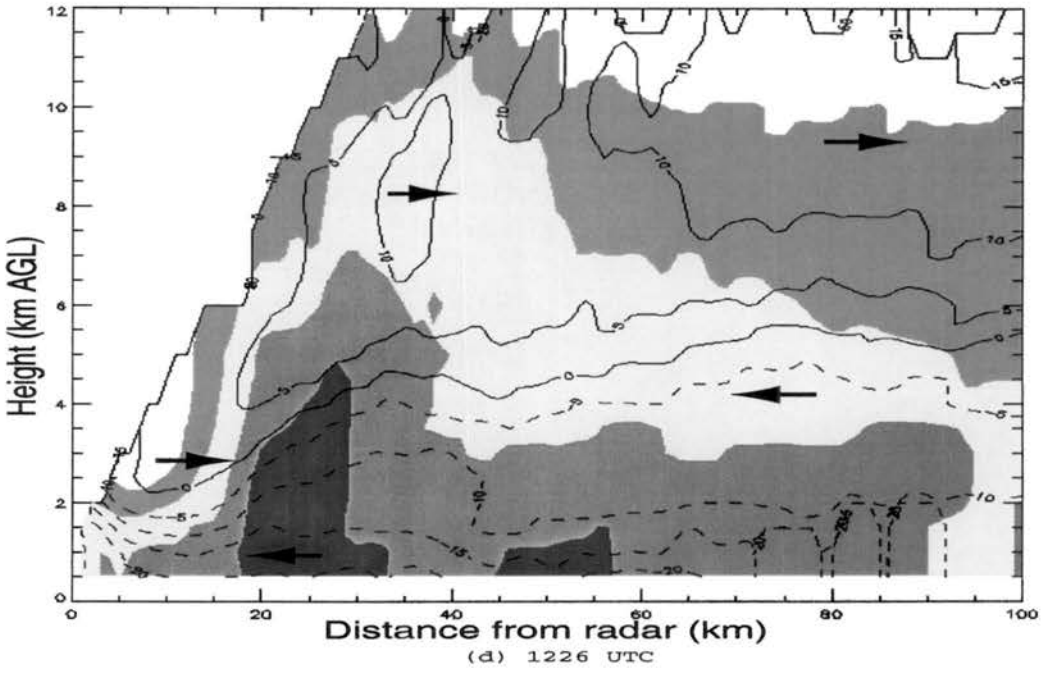

Figure 5.8: *Continued*

spread out smaller scale features. Numerous cross sections showed a significant bright band (Houze et al. 1989) progressing ahead of the convective line with a transition zone of low reflectivity dividing the two areas. One of them is shown in Fig. 5.9. They also showed evidence of a small trailing anvil, similar to the leading anvil seen in a TS storm (Fig. 2.1, taken from Houze et al. 1989).

Streamlines of vertical motion versus storm-relative winds from the RUC were used to determine how well the 60-km RUC could resolve the circulation features of this LS MCS (Fig. 5.10). The RUC captured upward motion in the area of the MCS and descending motion ahead of it, but it missed the details that Doppler radar was able to resolve. This comparison suggests there are serious limitations in inferring storm circulations from the coarse RUC and profiler analyses for the 30 April 2000 case.

A vertical cross section of 60-km RUC θ_e at 1200 UTC can be seen in Fig. 5.11. An elevated maximum of 327 K at 800 hPa is located west of the LS MCS. Storm-relative flow in this cross section appears to be easterly at this level, which does not agree with the Doppler radar cross sections. This is an example of the limitations of the lower resolution RUC dataset. Westerly storm-relative flow at this level (as determined by Doppler radar) is able to bring the high-θ_e air to the LS.

A cross section of potential temperature overlaid with relative humidity contours and storm-relative wind vectors can be seen in Fig. 5.12. This analysis captured most of the overall flow features but did not depict the elevated rear inflow evident in the Doppler radar data. The model captured areas of condensation where the flow was rising across isentropes, but it did not saturate the air there (relative humidities are from 60 to 90%). This apparent discrepancy is due to (1) some of the condensation in the RUC is parameterized, and (2) instantaneous fields of relative humidity and vertical motion should not be expected to match perfectly. Flow descending across isentropes reduced the relative humidity somewhat. A dry intrusion below 900 hPa extended eastward of 94 W and may be the model's attempt to capture the descending motion of the leading inflow jet. Similar dry conditions are known

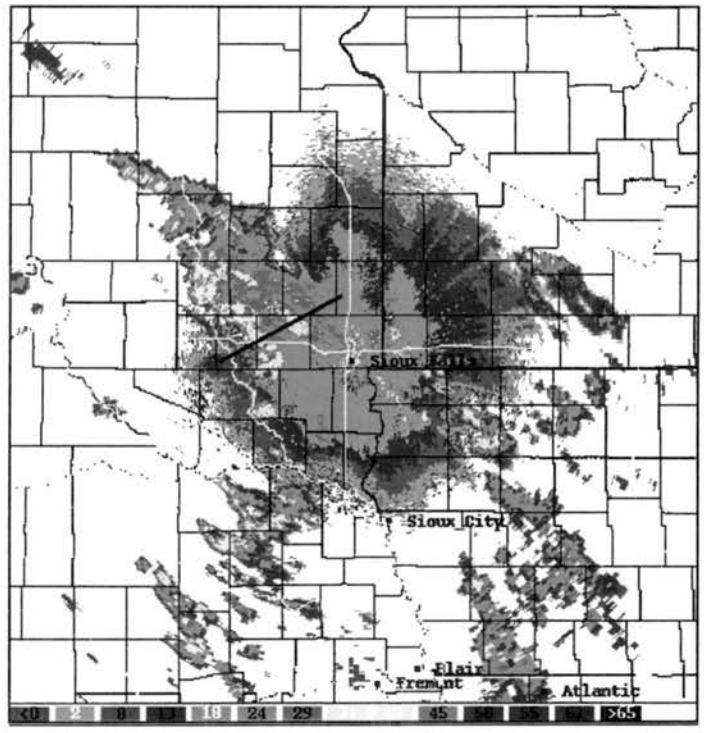

(a) 0728 UTC. Line is used for (b).

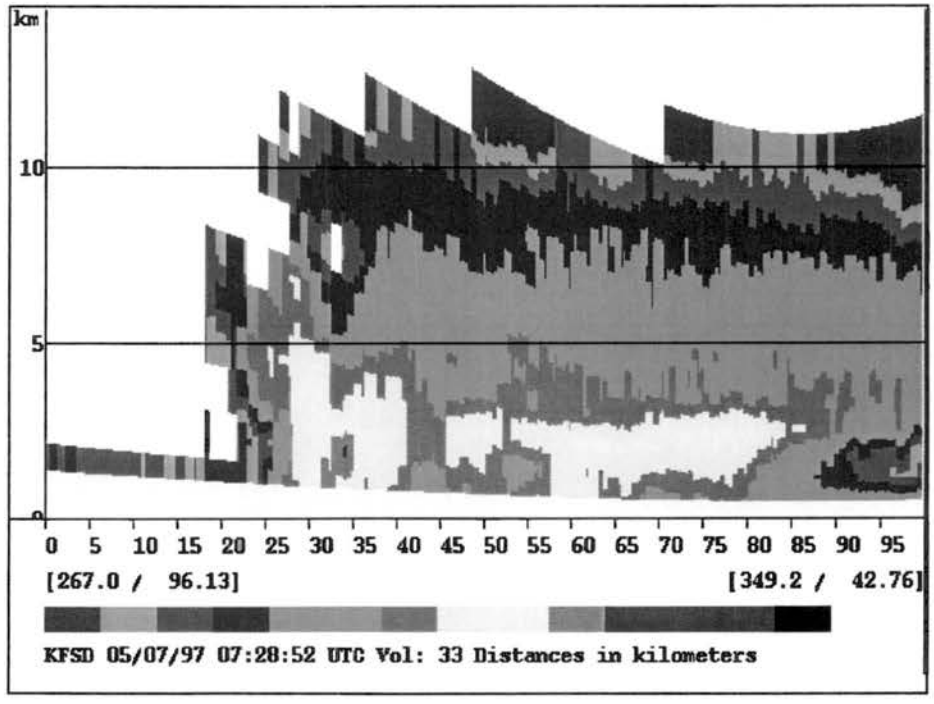

(b) 0728 UTC cross section

Figure 5.9: Vertical cross section of ungridded radar reflectivity at 0728 UTC taken at the line in Fig. 5.9a.

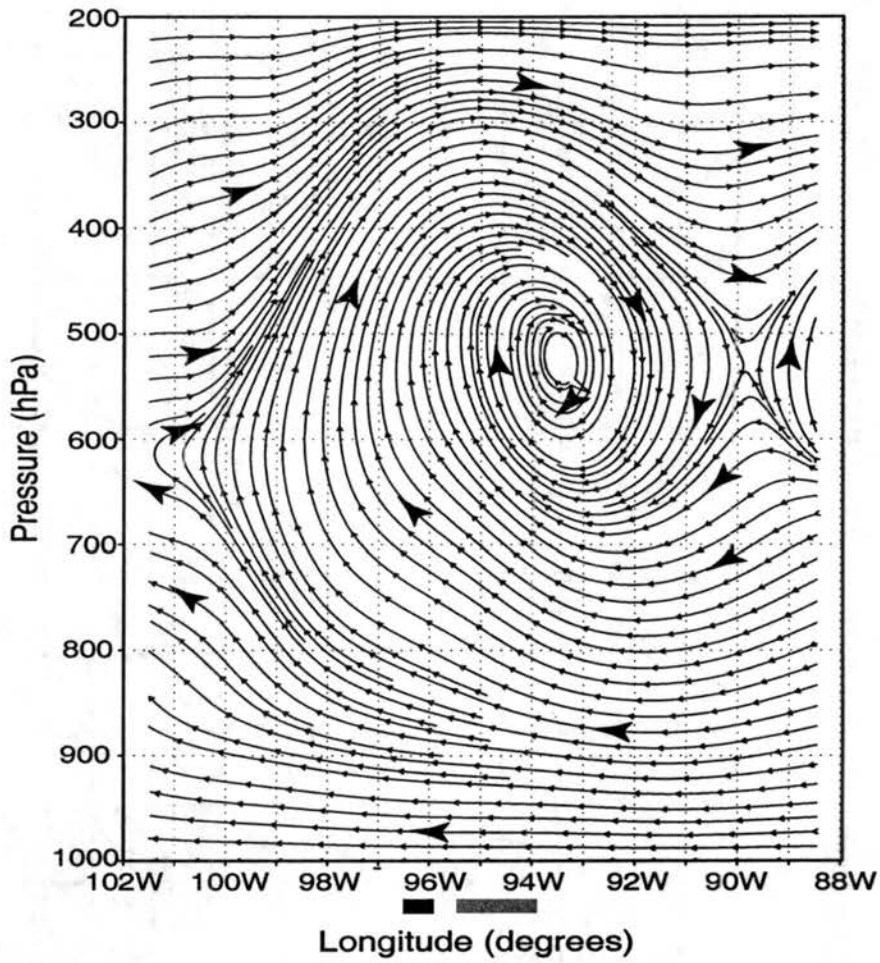

Figure 5.10: Vertical cross section of RUC derived storm-relative streamlines along 43 N for 1200 UTC. Vertical motion is scaled by 100. Black bar indicates convective region, gray bar indicates stratiform region.

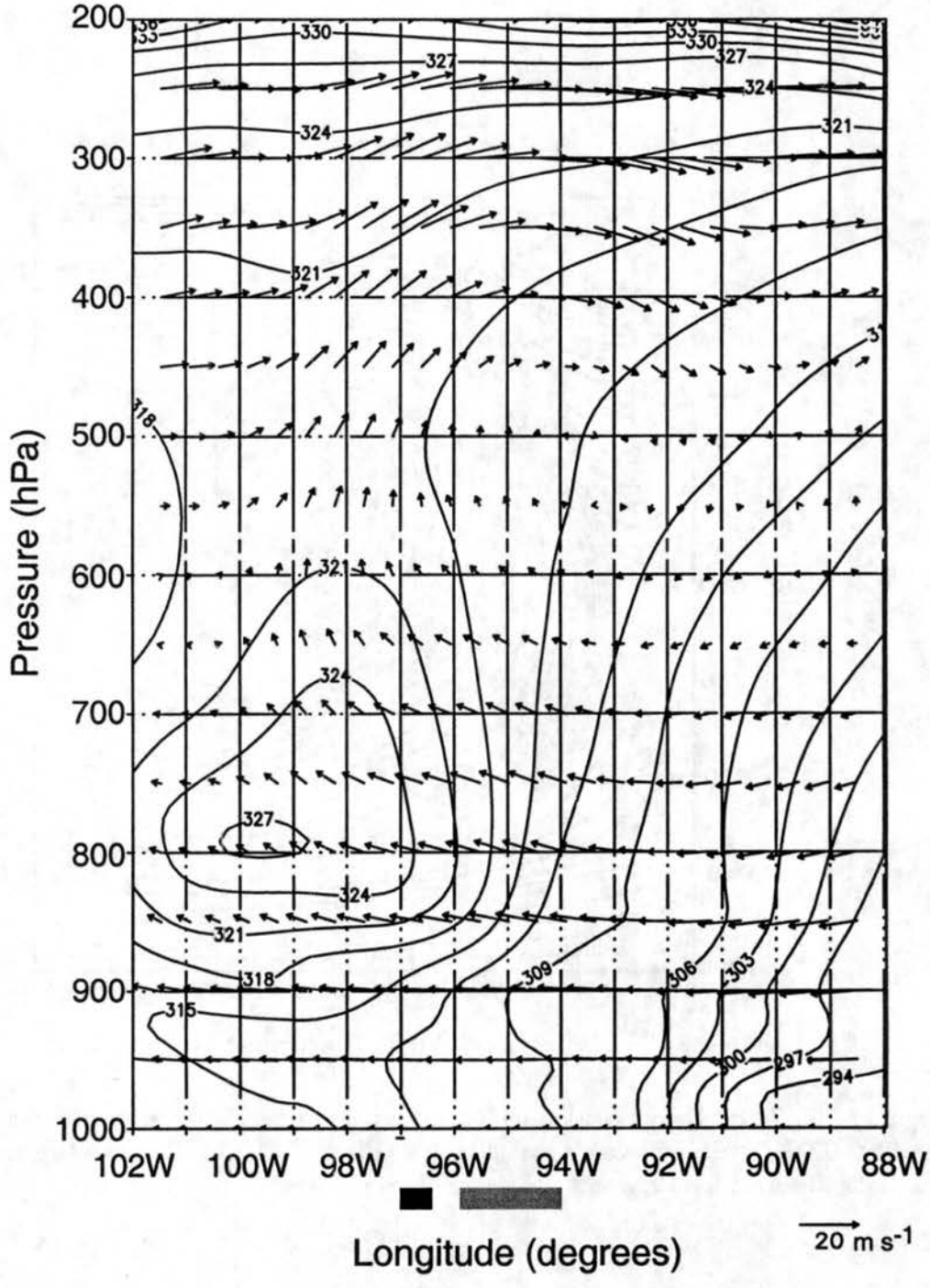

Figure 5.11: Vertical cross section of RUC equivalent potential temperature in K at 1200 UTC with storm-relative wind vectors (vertical motion scaled by 100) along line C-D in Fig. 5.3b. Black bar indicates convective region, gray bar indicates stratiform region.

to occur within the rear inflow jet of TS systems (Houze 1977; Zipser 1977; Johnson and Hamilton 1988).

The cross section in Fig. 5.12 looks very similar to a cross section of a warm front observed over the northern Atlantic with front relative winds seen in Wakimoto and Bosart (2001). If real, it could indicate that the lifting mechanism in this case is some combination of both warm frontal and convective lifting, which could have enhanced the stratiform rain area around 1500 UTC. Since convective cells are not being resolved, it is also possible that the RUC is showing a mixture of resolved stratiform and parameterized convection spread over the area.

Area averaged divergence and vertical motion profiles (Figs. 5.13 and 5.14) were produced over the stratiform rain area to determine if the model could capture distinct stratiform features. Another average was done over the entire MCS and produced similar results, indicating that the 60-km RUC cannot resolve the difference between convective and stratiform areas; instead, it combines the parameterized convection and the resolved stratiform area. The profiles produced (Fig. 5.13) are very similar to those from Cotton et al. (1989) for MCCs, with a maximum in upward vertical motion at mid-levels in the initial stage and at upper levels in the mature and dissipating stages. Divergence profiles agreed in a similar manner, with strong low-level convergence in the early stage and strong upper-level divergence in the later stages (Fig. 5.14).

The Doppler radar data for this case has permitted the first documentation of the detailed airflow within an LS MCS. There is ascending RTF flow atop a descending FTR flow. An elevated rear inflow exists between 2 and 3 km. Reflectivity features are similar to, but the mirror image of, those in TS storms, with a bright band, transition zone, and small leading anvil. An elevated θ_e maximum exists behind the system. A dry intrusion appears in the area of the leading inflow jet. The vertical structure from the RUC model looks very similar to a warm frontal cross section, showing that frontal overrunning may play a role in the initiation and formation of the LS.

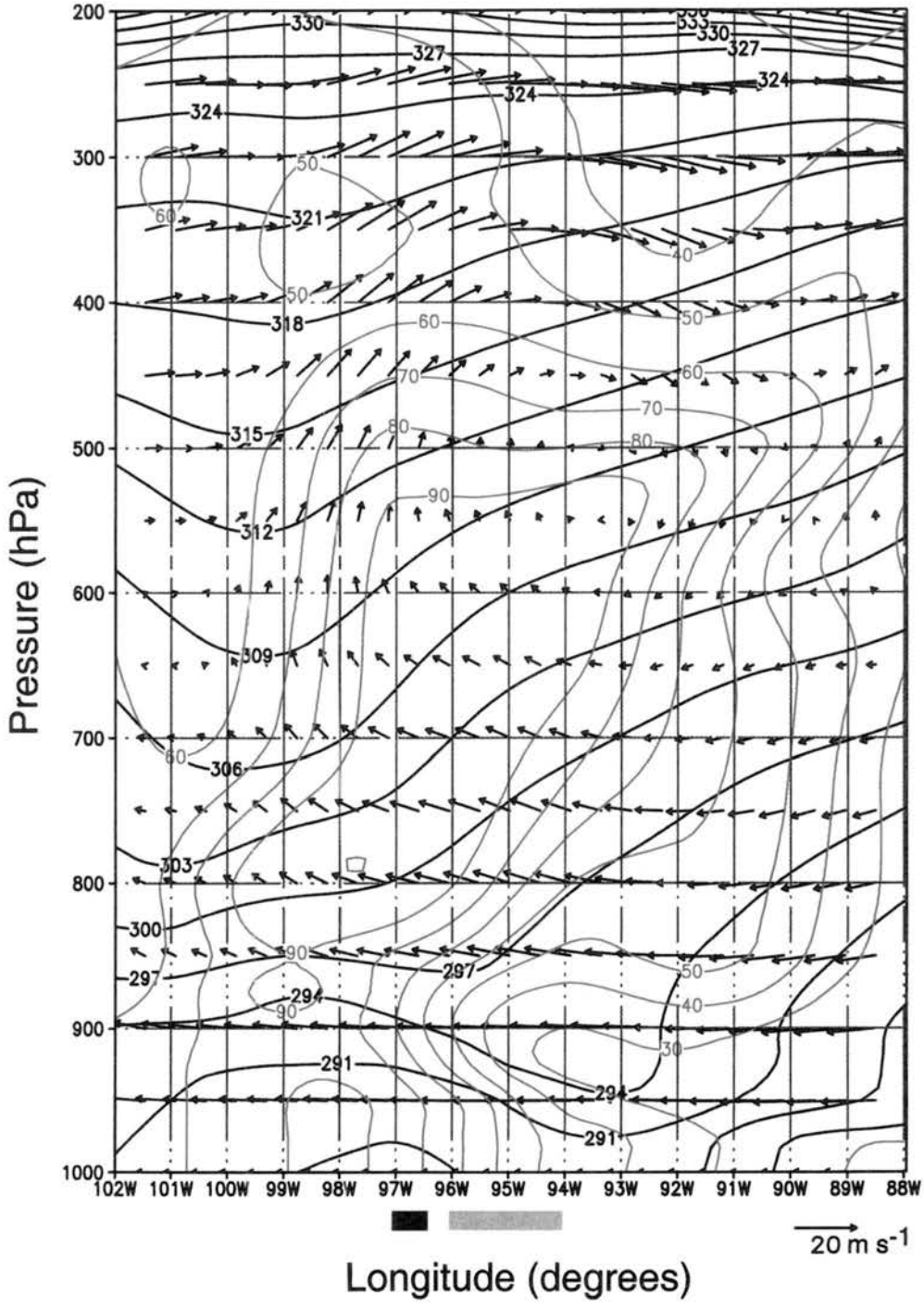

Figure 5.12: Vertical cross section of RUC potential temperature in K (black contours), relative humidity in percent (green contours), and storm-relative wind vectors (vertical motion scaled by 100) at 1200 UTC along line C-D in Fig. 5.3b. Black bar indicates convective region, gray bar indicates stratiform region.

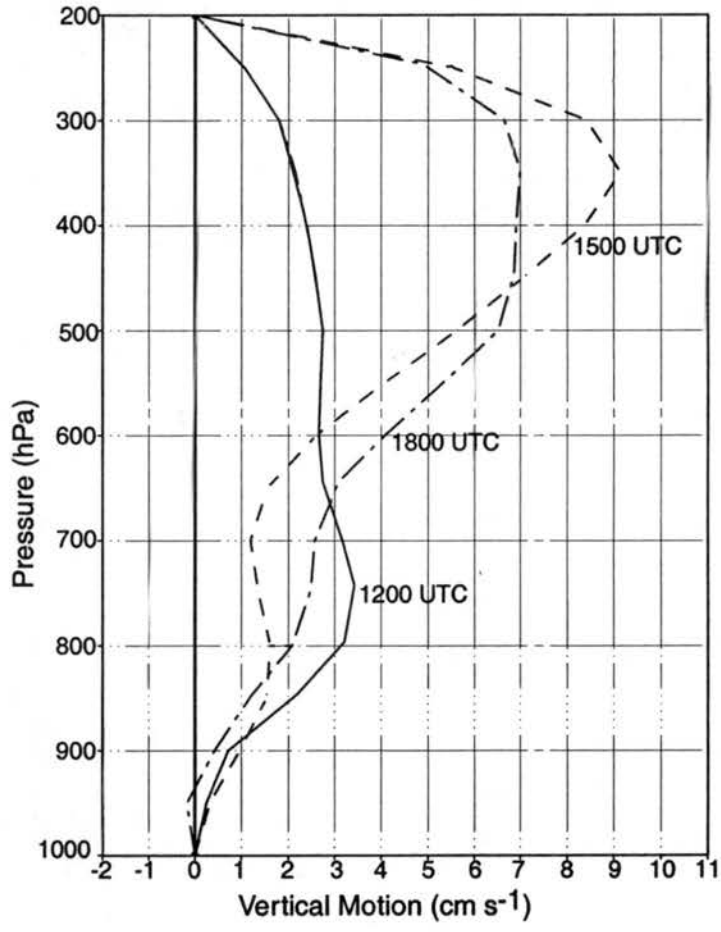

Figure 5.13: Area averaged vertical profile of vertical motion at 1200 (solid line), 1500 (dashed line) and 1800 UTC (dot-dashed line) from RUC data for the stratiform region.

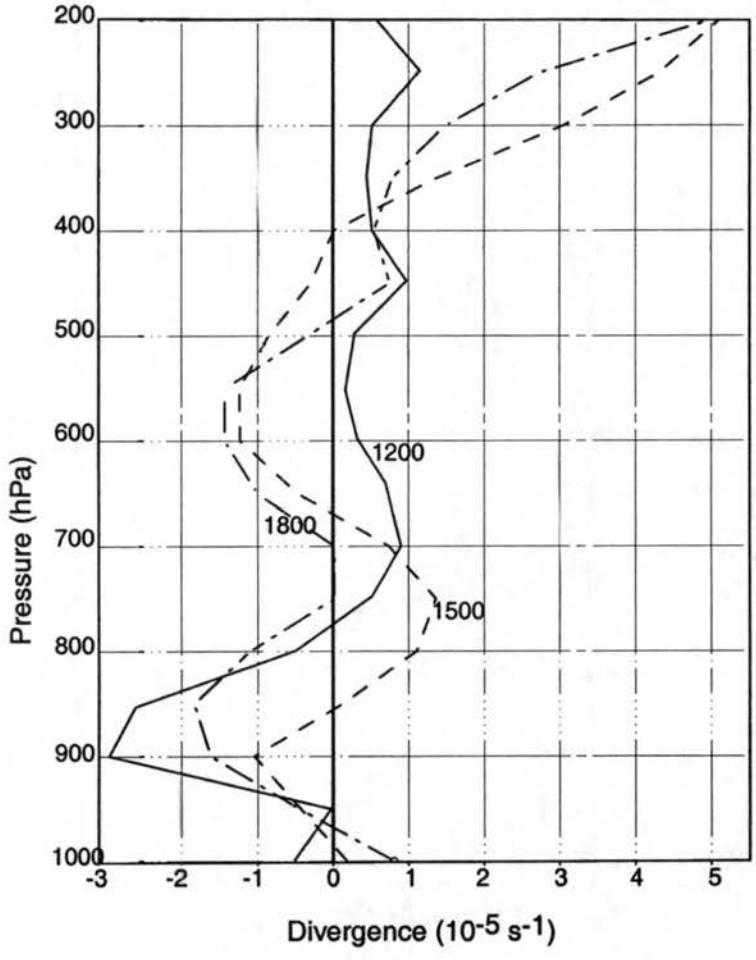

Figure 5.14: Area averaged vertical profile of divergence at 1200 (solid line), 1500 (dashed line) and 1800 UTC (dot-dashed line) from RUC data for the stratiform region.

In summary, vertical cross sections of Doppler radar show evidence of descending FTR flow at low-to-mid levels (leading inflow jet), and ascending RTF flow above it carrying hydrometeors downstream. Soundings from behind the storm and RUC data show an elevated θ_e maximum that is tapped by the RTF flow around 3 km (shown by radar). Reflectivity structure shows that while the convective line is more discontinuous than a TS system, it also has similar features to a TS storm, though they are a mirror image, with a small leading anvil and a bright band. RUC data show the potential for isentropic upglide to affect the storm, and provide evidence that the organization of the LS may be similar to that of a warm front.

Chapter 6

A SYNTHESIS OF THE TWO LS CASE STUDIES AND THEIR RELATIONSHIP TO TS FEATURES

Two leading stratiform mesoscale convective systems were examined in this study using operational datasets. While some features were specific to the individual case, many similar features were seen in both cases. A schematic diagram of the structure of the main features discovered in these cases can be seen in Fig. 6.1. Evidence of a leading inflow jet; leading mesolow; rear-feeding on an elevated θ_e maximum behind the system; frontal overrunning; canted, discontinuous convective cells; ascending rear-to-front flow at mid-to-upper levels; and an enhanced stratiform rain region can be detected in the cases. These features are described in the remainder of this chapter.

There is descending FTR flow at low-to-mid levels in both cases, referred to as a leading inflow jet. It has similar evolution and structure to a TS rear inflow jet. The rear inflow jet (RIJ) is caused by horizontal buoyancy gradients from latent heat release and unsaturated mesoscale descent which causes a horizontal pressure gradient to form and a horizontal vorticity couplet which favors rear inflow (LeMone 1983; LeMone et al. 1984; Smull and Houze 1987; Lafore and Moncrieff 1989). This buoyancy gradient presumably exists in an LS as well and serves to form the leading inflow jet in the same way. Descending motion in a TS RIJ has two potential causes. Upper level blocking of the flow by the anticyclone aloft of the stratiform region can channel flow downward (Schmidt and Cotton 1990; Nachamkin et al. 1994). This is unlikely in the case of LSs because the mean flow aloft is westerly, which would not allow the mean flow to impinge upon the anticyclone from the

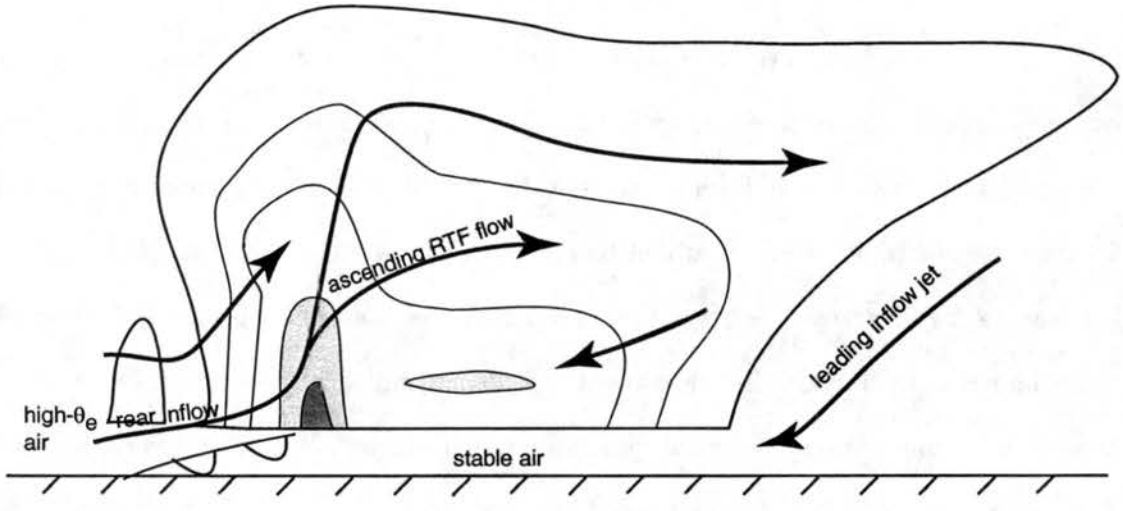

Figure 6.1: Conceptual model of an LS viewed in a vertical cross section oriented perpendicular to the convective line (i.e. parallel to its motion). Arrows indicate the direction of the flow. Reflectivities are thin contours. Cloud outlines are thicker contours. Areas of enhanced reflectivity are shaded.

east, causing it to descend and flow FTR in a storm-relative sense. Descending motion can also be caused and maintained by cooling due to evaporation and sublimation (Smull and Houze 1987; Zhang and Gao 1989; Gallus and Johnson 1991; Stensrud et al. 1991; Braun and Houze 1997). This would be possible in LSs as well, since the leading inflow jet would be travelling along the edge of the stratiform rain.

TS RIJs create wake lows due to subsidence warming (Fritsch and Chappell 1980; Johnson and Hamilton 1988; Schmidt and Cotton 1990; Gallus and Johnson 1991; Nachamkin et al. 1994). In a TS, the wake low is found just behind the stratiform rain area. In the 30 April LS, a leading mesolow was apparent in the mesonet data just ahead of the stratiform rain region, a mirror image of the wake low location in a TS. The 30 April leading mesolow moved in a different manner than that of a wake low TS, though. In a TS, the wake low typically "hugs" the back of the stratiform region throughout the storm's lifetime (Johnson and Hamilton 1988; Loehrer and Johnson 1995; Johnson 2001). The 30 April leading mesolow formed near the front edge of the stratiform rain, but then moved parallel to the stratiform rain toward the southeast and out of the Oklahoma mesonet altogether. The wake low of a TS system is also typically part of a mesohigh-wake low couplet that is produced by the movement of the storm and moves together with the system. No mesohigh was visible in the 30 April LS, possibly because there was little movement of the system, and the convective cells were out of the Oklahoma mesonet for most of its lifetime. While the leading mesolow could have its origin in subsidence warming from the descending leading inflow jet, its movement away from the stratiform rain region toward the southeast cannot be explained. Analysis of surface pressure and wind data indicated the mesolow had some gravity wave characteristics. The possibility of the leading mesolow being a gravity wave or a gravity current was addressed, but no conclusions could be drawn from the available data. Therefore the origin and essence of this leading mesolow are considered unknown.

Rear feeding from an elevated θ_e maximum behind the convective line and some potential for frontal overrunning was apparent in both the 30 April 2000 and the 7 May 1997

LSs. This is different from a typical TS system, in which a maximum in θ_e is usually ahead of the system and rooted in the boundary layer. Nocturnal MCC development to the north of quasi-stationary fronts have been attributed to low-level warm advection (Maddox and Doswell 1982) and to destabilization by diurnally modulated low-level jets, mesoscale ascents produced by fronts and convergence near the terminus of the jet (Trier and Parsons 1993). There is evidence of elevated warm advection in the LS cases as well as a front which could provide mesoscale ascent. The 30 April LS also has a low-level jet. Low-level jets enhance moisture and temperature advection, increase low level convergence, and increase vertical wind shear (Means 1952; Bonner 1966; Wallace 1975; Maddox 1983; and Trier and Parsons 1993). Emanuel (1985) suggested that frontogenetical forcing in a symmetrically neutral environment was a possible initiation mechanism for elevated convection. Colman (1990) found that elevated thunderstorms in a convectively stable environment with little to no CAPE are likely the product of frontogenetical forcing in the presence of weak symmetric stability. Conditional symmetric instability states that the atmosphere is stable with respect to vertical (buoyancy) and horizontal (inertial) displacements but unstable with respect to displacements along slantwise paths (Bennetts and Hoskins 1979; Emanuel 1979; Schultz and Schumacher 1999). Colman (1990) found that elevated thunderstorms in frontal overrunning situations developed in strongly baroclinic environments and were aligned along the geostrophic shear, which is consistent with moist symmetric instability (Emanuel 1979, 1983). The cross sections of θ_e and wind contours for both cases look similar to a cross section of an oceanic warm front by Wakimoto and Bosart (2001) (Fig. 6.2). This similarity could lend credence to the idea that frontal lifting is important in these two cases, and provides the means for the elevated convection to develop. Perhaps these storms start with weak symmetric stability and slantwise frontal forcing, and through this mechanism their parcels reach convective instability and continue to develop.

Houze et al. (1990) described the convective line of the TS system as having elongated cells oriented 45–90 degrees with respect to the line. This canting of cells is also seen in

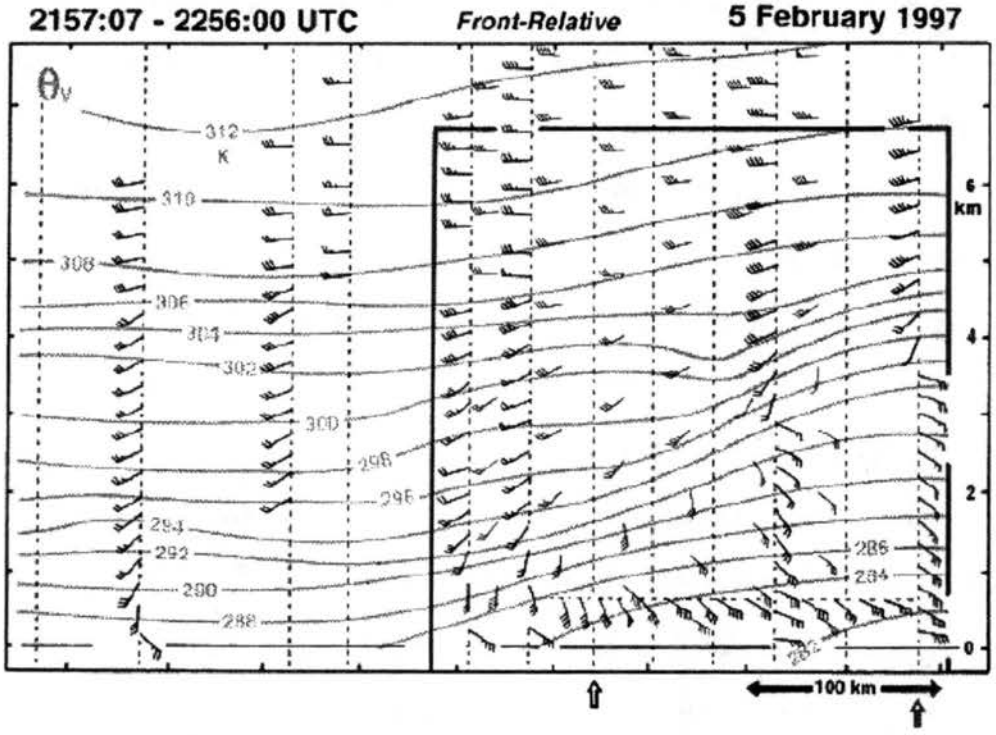

Figure 6.2: Vertical cross section of oceanic warm front taken from Wakimoto and Bosart (2001: their Fig. 9b). Front-relative winds superimposed onto virtual potential temperature (gray lines). Wind vectors are plotted with the following notation: flag = 25 m s^{-1}, barb = 5 m s^{-1}, half barb = 2.5 m s^{-1}.

both LS systems studied here. Houze et al. (1990) also describes the convective line as having a solid appearance, with a series of intense reflectivity cells connected by echo of more moderate intensity. The LS cases are distinctly different in this manner.

Discontinuous convective lines were seen in both cases. There are several potential reasons for this. Neiman et al. (1993) described a process of elevator/escalator of downscale convective-symmetric instability that led to convection in an extratropical cyclone. Fig. 6.3 shows a schematic diagram of this process. The schematic diagram looks similar to both LS case studies, with convection forming ahead of a front and stratiform rain moving out ahead of it. Another possibility for the banded structure of the convective cells is horizontal convective rolls (Kuettner 1959, 1971; LeMone 1973; Brown 1980). Horizontal convective rolls consist of counterrotating helices aligned nearly parallel to the mean boundary layer wind direction (Atkins et al. 1995). Convective bands in these rolls also form parallel to (or within a 15° angle of) the mean wind in the boundary layer (Kuettner 1971; LeMone 1973). Using station observations for both cases, it is difficult to determine the mean boundary layer wind near the vicinity of the convection. Individual stations at some time periods meet this requirement while others do not. Many of the stations in the close vicinity of the convection have been modified by it, making it difficult to determine the mean wind in the area of the storm. With a few stations indicating winds parallel to the elongated convective cells, horizontal convective rolls may well play a part in forming these discontinuous, canted convective cells.

Another possibility can be seen in Fritsch et al. (1994). With both of these LS systems being rear-fed, the shear vorticity and cold pool vorticity are of the same sign. This does not allow for strong lifting along the linear boundary of the cold pool. Instead, parcels do not reach their LFC until they are above the cold pool. If the forcing is not consistent above the cold pool, the ensuing convective line would be discontinuous. It is important to note, however, that in the Fritsch et al. (1994) case convection develops over the center of the cold pool, while in this study the convection seems to develop at the back edge of the

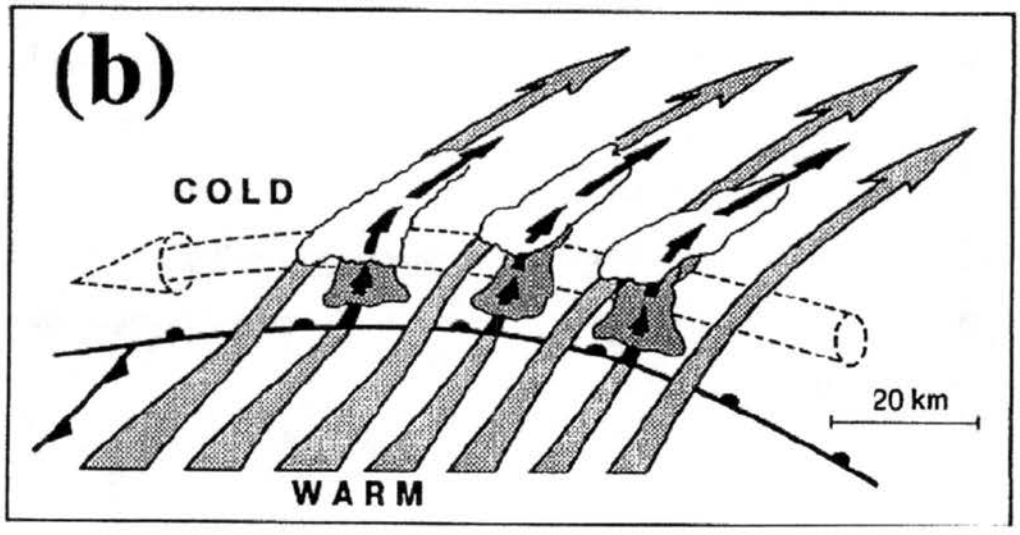

Figure 6.3: Schematic of downscale convective-symmetric instability as depicted in the "escalator-elevator" warm-frontal-ascent model (Neiman et al. 1993, their Fig. 8). Warm southerly airstream (flat, lightly stippled arrows) rises over the cold easterly polar airstream (tubular dashed arrow). Mesoconvective ascent (the elevator, solid arrows) and convective clouds (stippled with white anvils) are shown at regular intervals between regions of gentler ascent (the escalator).

cold pool.

Ascending RTF flow at mid-to-upper levels is seen in both cases. This flow appears very similar to, but a mirrow image of, TS flow. In a TS system, this flow advects hydrometeors rearward of the convective line. Most of these will be ice particles. In TS systems the fallspeed of the ice particles is generally greater than that of the ascending air motion (Rutledge et al. 1988). Therefore the ice particles fall slowly as they are carried away from the convective region, growing first by vapor deposition and then forming aggregates as they reach warmer air (Houze et al. 1989). As the aggregates fall through the freezing level, they begin to melt, forming a bright band on radar and an area of heavy stratiform rain (Houze et al. 1989). This bright band signature is evident in the vertical cross sections of the 7 May 1997 case, and a region of stratiform rain with enhanced reflectivity ahead of the convective line is seen in the horizontal reflectivity fields of both cases ahead of the convective line. This evidence suggests that hydrometeor transport similar to, but a mirror

image of, that in a TS system is occurring in the ascending RTF flow of the LS system.

In summary, features found in the two LS case studies presented were synthesized to produce the schematic shown in Fig. 6.1. Features noted in these cases included a leading inflow jet, leading mesolow, rear-feeding from an elevated θ_e maximum behind the system, frontal overrunning, canted, discontinuous convective cells, ascending RTF flow at mid-to-upper levels, and an enhanced stratiform rain region. These results give insight into the structure of LS systems.

Chapter 7

SUMMARY AND FUTURE WORK

7.1. Summary

Data from Doppler radar, NOAA's Wind Profiler Network, radiosonde soundings, the Oklahoma mesonet, and the 40-km and 60-km RUC model were combined to analyze two leading stratiform mesoscale convective systems. The 30 April 2000 LS was slow moving and produced flash floods, while the 7 May 1997 case moved rapidly. The main findings of these case studies will be summarized by addressing the three questions posed at the end of Chapter 2.

What are the airflow characteristics for LS storms?

Airflow characteristics that were consistent for both cases included three main flow branches. First there was a rear inflow at 2–3 km that brought high-θ_e, moist air into the convective cells. This appeared to have some interaction with frontal overrunning. Second, there was a rising RTF flow at upper levels that carried hydrometeors downstream to form the stratiform rain ahead of the convective line. Third, there was a sinking FTR flow at low-to-mid levels, a "leading inflow jet", that may be the equivalent of the TS rear inflow jet.

Are some LS systems fed from the back side of the storm? If so, how does such a flow pattern enhance the potential for heavy rainfall?

Yes, the two cases studied were both rear-fed. This may enhance the potential for heavy rain in several ways. It allows storms to develop in environments where air ahead of the system is stable by tapping into high-θ_e air from behind the storm. It also enhances the

possibility that the convective cells will back-build. This causes a cell to form by the rear inflow, advect away, and have another cell form over the same area. This keeps the system relatively stationary, which heightens its potential for flooding (Chappell 1986). It is also possible that flooding may be enhanced by stratiform rain moistening the ground before convective cells arrive.

What are the surface features associated with LS systems?

A leading mesolow was spotted in the 30 April case which travelled parallel to the edge of the stratiform rain. No mesohigh was seen, but this may be due to convective cells being out of the Oklahoma mesonet over most of the storm's lifetime. Without high resolution surface data for 7 May, no mesoscale surface pressure patterns were detectable. Weak cold pools were observed in both cases. Both cases formed in proximity to surface warm or stationary fronts, contributing to frontal overrunning of high-θ_e air.

7.2. Future work

There is a great deal more that can be learned about these systems. While this study provides observations of two rear-fed LS MCSs, it is not comprehensive. High resolution Doppler radar data was only available for one of the cases, making it difficult to generalize the results to include most rear-fed LSs. A study of more cases of LS systems using Doppler radar to produce a composite of storm-relative flow would be beneficial to extend the flow characteristics found in these two cases to other systems.

A Dual-Doppler study of LS systems would provide much better information on vertical motion in the storms. This may help to better understand how these systems are similar to/different from TS storms.

Since rear-fed LSs have features which make them conducive to flood production, a climatology of flood-producing LSs is necessary to determine what features are common to these flooding systems, and what environmental conditions are favorable for their formation. This information could greatly aid in the forecasting of flash flood events.

Finally, this study examined two elevated, rear-fed LSs. However, Parker and Johnson (2000) showed that the average storm-relative surface and mid-level flow of the LSs they studied is FTR, showing that several cases must be front-fed. Observational and modelling studies of these systems should be done to determine potential differences between them and the cases studied here and what effect these might have on the potential for flooding.

REFERENCES

Atkins, N. T., R. M. Wakimoto, and T. M. Weckwerth, 1995: Observations of the sea-breeze front during CaPE. Part II: Dual-Doppler and Aircraft Analysis. *Mon. Wea. Rev.*, **123**, 944–969.

Barnes, S.L., 1973: Mesoscale objective analysis using weighted time-series observations. *NOAA Tech. Memo. ERL NSSL-62*, National Severe Storms Laboratory, Norman, OK 73069, 60pp. [NTIS COM-73-10781].

Benjamin, S.G., J.M. Brown, K.J. Brundage, B.E. Schwartz, T.G. Smirnova, and T.L. Smith, 1998: The operational RUC-2. Preprints, *16th Conference on Weather Analysis and Forecasting*, AMS, Phoenix, 249-252.

Benjamin, S. G., K. J. Brundage, and L. L. Morone, 1994: The Rapid Update Cycle. Part I: Analysis/model description. *Technical Procedures Bulletin No. 416*, NOAA/NWS, 16 pp.

Bennetts, D. A., and B. J. Hoskins, 1979: Conditional symmetric instability–A possible explanation for frontal rainbands. *Quart. J. Roy. Meteor. Soc.*, **105**, 945–962.

Bernstein, B. C., and R. H. Johnson, 1994: A dual-Doppler radar study of an OK PRE-STORM heat burst event. *Mon. Wea. Rev.*, **122**, 259–273.

Bluestein, H. B. and M. H. Jain, 1985: Formation of mesoscale lines of precipitation: Severe squall lines in Oklahoma during the spring. *J. Atmos. Sci.*, **42**, 1711–1732.

Bonner, W. D., 1966: Case study of thunderstorm activity in relation to the low-level jet. *Mon. Wea. Rev.*, **94**, 167–178.

Brandes, E. A., 1990: Evolution and structure of the 6-7 May 1985 mesoscale convective system and associated vortex. *Mon. Wea. Rev.*, **118**, 109–127.

Braun, S. A., and R. A. Houze, Jr., 1997: The evolution of the 10-11 June 1985 PRESTORM squall line: Initiation, development of rear inflow and dissipation. *Mon. Wea. Rev.*, **125**, 478–504.

Brock, F. V., K. C. Crawford, R. L. Elliott, G. W. Cuperus, S. J. Stadler, H.L. Johnson, and M. D. Eilts, 1995: The Oklahoma mesonet: A technical overview. *J. Atmos. Oceanic Technol.*, **12**, 5–19.

Brown, R. A., 1980: Longitudinal instabilities and secondary flows in the planetray boundary layer: A review. *Rev. Geophys. Space Phys.*, **18**, 683–697.

Carbone, R. E., 1982: A severe frontal rainband. Part I: Stormwide hydrodynamic structure. *J. Atmos. Sci.*, **39**, 258–279.

Chappell, C. F., 1986: Quasi-stationary convective events. In *Mesoscale Meteorology and Forecasting*, P. S. Ray, Ed., Amer. Meteor. Soc., 289–310.

Colman, B. R., 1990: Thunderstorms above frontal surfaces in environments without positive CAPE. Part II: Organization and instability mechanisms. *Mon. Wea. Rev.*, **118**, 1123–1144.

Cotton, W. R., M. Lin, R. L. McAnelly, and C. J. Tremback, 1989: A compossite model of mesoscale convective complexes. *Mon. Wea. Rev.*, **117**, 765–783.

Doswell, C. A., III, 1977: Obtaining meteorologically significant surface divergence fields through the filtering property of objective analysis. *Mon Wea. Rev.*, **105**, 885–892.

Doswell, C. A., III, H. E. Brooks, and R. A. Maddox, 1996: Flash flood forecasting: An ingredients-based methodology. *Wea. Forecasting*, **11**, 560–581.

Emanuel, K. A., 1979: Inertial instability and mesoscale convective systems. Part I: Linear theory of inertial instability in rotating viscous fluids. *J. Atmos. Sci.*, **36**, 2425–2449.

Emanuel, K. A., 1983: The Lagrangian parcel dynamics of moist symmetric stability. *J.*

Atmos. Sci., **40**, 2368–2376.

Emanuel, K. A., 1985: Frontal circulations in the presence of small moist symmetric instability. *J. Atmos. Sci.*, **42**, 1062–1071.

Fritsch, J. M., and C. F. Chappell, 1980: Numerical prediction of convectively driven mesoscale pressure systems. Part II: Mesoscale model. *J. Atmos. Sci.*, **37**, 1734–1762.

Fritsch, J. M., R. J. Kane, and C. R. Chelius, 1986: The contribution of mesoscale convective weather systems to the warm-season precipitation in the United States. *J. Clim. Appl. Meteor.*, **25**, 1333–1345.

Fritsch, J. M., J. D. Murphy, J. S. Kain, 1994: Warm core vortex amplification over land. *J. Atmos. Sci.*, **51**, 1780–1807.

Fujita, T. T., 1955: Results of detailed synoptic studies of squall lines. *Tellus*, **7**, 405–436.

Fujita, T. T., 1978: Manual of downburst identification for project NIMROD. SMRP Research Paper 156, University of Chicago, 42 pp.

Gallus, Jr., W. A., and R. H. Johnson, 1991: Heat and moisture budgets of an intense midlatitude squall line. *J. Atmos. Sci.*, **48**, 122–146.

Golden, J. H., R. Serafin, V. Lally, and J. Facundo, 1986: Atmospheric sounding systems. *In Mesoscale Meteorology and Forecasting*, P.S. Ray (Ed.), Amer. Meteor. Soc., Boston, 50–70.

Grady, R. L., and J. Verlinde, 1997: Triple-Doppler analysis of a discretely propagating, long-lived, High Plains squall line. *J. Atmos. Sci.*, **54**, 2729–2748.

Haertel, P. T., and R. H. Johnson, 2000: The linear dynamics of squall-line mesohighs and wake lows. *J. Atmos. Sci.*, **57**, 93–107.

Haertel, P. T., R. H. Johnson, and S. N. Tulich, 2001: Some simple simulations of thunderstorm outflows. *J. Atmos. Sci.*, **58**, 504–516.

Houze, R. A., Jr., 1977: Structure and dynamics of a tropical squall-line system observed during GATE. *Mon. Wea. Rev.*, **105**, 1540–1567.

Houze, R. A., Jr., S. A. Rutledge, M. I. Biggerstaff,and B. F. Smull, 1989: Interpretation of Doppler weather radar displays of midlatitude mesoscale convective systems. *Bull. Amer. Meteor. Soc.*, **70**, 608–619.

Houze, R. A., Jr., B. F. Smull, and P. Dodge, 1990: Mesoscale organization of springtime rainstorms in Oklahoma. *Mon. Wea. Rev.*, **118**, 613–654.

Huschke, R. E., 1959: *Glossary of Meteorology*. Amer. Meteor. Soc., 638 pp.

Johnson, B. C., 1983: The heat burst of 29 May 1976. *Mon. Wea. Rev.*, **111**, 1776–1792.

Johnson, R. H., and P. J. Hamilton, 1988: The relationship of surface pressure features to the precipitation and airflow structure of an intense midlatitude squall line. *Mon. Wea. Rev.*, **116**, 1444–1472.

Johnson, R. H., S. Chen, and J. J. Toth, 1989: Circulations associated with a mature-to-decaying midlatitude mesoscale convective system. Part I: Surface features-Heat bursts and mesolow development. *Mon. Wea. Rev.*, **117**, 942–959.

Johnson, R. H., 2001: Surface mesohighs and mesolows. *Bull. Amer. Meteor. Soc.*, **82**, 13–31.

Johnson, R. H., and M. D. Parker, 2001: Mesoscale convective systems and floods: A review. *Preprints, Symposium on Precipitation Extremes: Prediction, Impacts, and Responses*, Albuquerque, NM, Amer. Meteor. Soc., 102–106.

Koch, S. E., M. DesJardins, and P. J. Kocin, 1983: An interactive Barnes objective map analysis scheme for use with satellite and conventional data. *J. Appl. Meteor.*, **22**, 1487–1502.

Koch, S. E., and R. E. Golus, 1988: A mesoscale gravity wave event observed during CCOPE. Part I: Multiscale statistical analysis of wave characteristics. *Mon. Wea. Rev.*, **116**, 2527–2544.

Koch, S. E., and L. M. Siedlarz, 1999: Mesoscale gravity waves and their environment in the central United States during STORM-FEST. *Mon. Wea. Rev.*, **127**, 2854–2879.

Kuettner, J. P., 1959: The band structure of the atmosphere. *Tellus*, **11**, 267–294.

Kuettner, J. P., 1971: Cloud bands in the earth's atmosphere: Observations and theory. *Tellus*, **23**, 404–425.

Lafore, J. P., and M. W. Moncrieff, 1989: A numerical investigation of the organization and interaction of the convective and stratiform regions of tropical squall lines. *J. Atmos. Sci.*, **46**, 521–544.

LeMone, M. A., 1973: The structure and dynamics of horizontal roll vortices in the planetary boundary layer. *J. Atmos. Sci*, **30**, 1077–1091.

LeMone, M. A., 1983: Momentum transport by a line of cumulonimbus. *J. Atmos. Sci.*, **40**, 1815–1834.

LeMone, M. A., G. M. Barnes, and E. J. Zipser, 1984: Momentum fluxes by lines of cumulonimbus over the tropical oceans. *J. Atmos. Sci.*, **41**, 1914–1932.

Loehrer, S. M., and R. H. Johnson, 1995: Surface pressure and precipitation life cycle characteristics of PRE-STORM mesoscale convective systems. *Mon. Wea. Rev.*, **123**, 600–621.

Maddox, R. A., C. F. Chappell, and L. R. Hoxit, 1979: Synoptic and meso-α scale aspects of flash flood events. *Bull. Amer. Meteor. Soc.*, **60**, 115–123.

Maddox, R. A., 1980: An objective technique for separating macroscale and mesoscale features in meteorological data. *Mon. Wea. Rev.*, **108**, 1108–1121.

Maddox, R. A., 1980: Mesoscale convective complexes. *Bull. Amer. Meteor. Soc.*, **61**, 1374–1387.

Maddox, R. A., and C. A. Doswell, 1982: Examination of jet stream configurations, 500-mb vorticity advection, and low-level thermal advection patterns during extended periods of intense convection. *Mon. Wea. Rev.*, **110**, 184–197.

Maddox, R. A., 1983: Large-scale meteorological conditions associated with midlatitude mesoscale convective complexes. *Mon. Wea. Rev.*, **111**, 1475–1493.

Means, L. L., 1952: On thunderstorm forecasting in the central United States. *Mon. Wea. Rev.*, **80**, 165–189.

Moncrieff, M. W., 1992: Organized convective systems: Archetypal dynamical models, mass and momentum flux theory, and parameterization. *Q. J. R. Meteor. Soc.*, **118**, 819–850.

Moncrieff, M. W., and C. Liu, 1999: Convection initiation by density currents: Role of convergence, shear, and dynamical organization. *Mon. Wea. Rev.*, **127**, 2455–2464.

Nachamkin, J. E., R. L. McAnelly, W. R. Cotton, 1994: An observational analysis of a developing mesoscale convective complex. *Mon. Wea. Rev.*, **122**, 1168–1188.

Neiman, P. J., M. A. Shapiro, and L. S. Fedor, 1993: The life cycle of an extratropical marine cyclone. Part II: Mesoscale structure and diagnostics. *Mon. Wea. Rev.*, **121**, 2177–2199.

O'Brien, J. J., 1970: Alternative solutions to the classical vertical velocity problem. *J. Appl. Meteor.*, **9**, 197–203.

Parker, M.D., and R.H. Johnson, 2000: Organizational modes of midlatitude mesoscale convective systems. *Mon. Wea. Rev.*, **128**, 3413-3436.

Pedgley, D. E., 1962: A meso-synoptic analysis of the thunderstorms on 28 August 1958. *Brit. Meteor. Off. Geophys. Mem. No. 106*, 74 pp.

Ralph, R. M., M. Crochet, and S. V. Venkateswaran, 1993: Observations of a mesoscale ducted gravity wave. *J. Atmos. Sci.*, **50**, 3277–3291.

Rotunno, R., J. B. Klemp, and M. L. Weisman, 1988: A theory for strong, long-lived squall lines. *J. Atmos. Sci.*, **45**, 463–485.

Rutledge, S. A. and R.A. Houze, Jr., 1987: A diagnostic modeling study of the trailing stratiform region of a midlatitude squall line. *J. Atmos. Sci.*, **44**, 2640-2656.

Rutledge, S. A., R. A. Houze, and M. I. Biggerstaff, 1988: The Oklahoma-Kansas mesoscale convective system of 10–11 June 1985: Precipitation structure and single-Doppler

radar analysis. *Mon. Wea. Rev.*, **116**, 1409–1430.

Schiesser, H. H., R. A. Houze Jr., and H. Huntrieser, 1995: The mesoscale structure of severe precipitation systems in Switzerland. *Mon. Wea. Rev.*, **123**, 2070–2097.

Schmidt, J. M., and W. R. Cotton, 1990: Interactions between upper and lower tropospheric gravity waves on squall line structure and maintenance. *J. Atmos. Sci.*, **47**, 1205–1222.

Schultz, D. M., and P. Schumacher, 1999: Review: The use and misuse of conditional symmetric instability. *Mon. Wea. Rev.*, **127**, 2709–2732.

Smull, B. F., and R. A. Houze, Jr., 1985: A midlatitude squall line with a trailing stratiform rain: Radar and satellite observations. *Mon. Wea. Rev.*, **113**, 117-133.

Smull, B. F. and R. A. Houze, Jr., 1987: Rear inflow in squall lines with trailing stratiform precipitation. *Mon. Wea. Rev.*, **115**, 2869–2889.

Stensrud, D. J., R. A. Maddox, and C. L. Ziegler, 1991: A sublimation-initiated mesoscale downdraft and its relation to the wind field below a precipitating anvil cloud. *Mon. Wea. Rev.*, **119**, 2124–2139.

Stumpf, G. J., R. H. Johnson, B. F. Smull, 1991: The wake low in a midlatitude mesoscale convective system having complex convective organization. *Mon. Wea. Rev.*, **119**, 134–158.

Trier, S. B., and D. B. Parsons, 1993: Evolution of environmental conditions preceding the development of a nocturnal mesoscale convective complex. *Mon. Wea. Rev.*, **121**, 1078–1098.

Wakimoto, R. M., and B. L. Bosart, 2001: Airborne radar observations of a warm front during FASTEX. *Mon. Wea. Rev.*, **129**, 254–274.

Wallace, J. M., 1975: Diurnal variations in precipitation and thunderstorm frequency over the conterminous United States. *Mon. Wea. Rev.*, **103**, 406–419.

Weber, B. L., D. B. Wuertz, D. C. Welsh, and R. McPeek, 1993: Quality controls for profiler measurements of winds and RASS temperatures. *J. Atmos. Oceanic Technol.*,

10, 452–464.

Weisman, M. L., 1992: The role of convectively generated rear-inflow jets in the evolution of long-lived mesoconvective systems. *J. Atmos. Sci.*, **49**, 1826–1847.

Zhang, D.-L., and K. Gao, 1989: Numerical simulation of an intense squall line during 10-11 June 1985 PRE-STORM. Part II: Rear inflow, surface pressure perturbations and stratiform precipitation. *Mon. Wea. Rev.*, **117**, 2067–2094.

Zipser, E. J., 1977: Mesoscale and convective-scale downdrafts as distinct components of squall-line circulation. *Mon. Wea. Rev.*, **105**, 1568–1589.

Zipser, E. J., 1982: Use of a conceptual model of the life cycle of mesoscale convective systems to improve very-short-range forecasts. *Nowcasting*, K. Browning, Ed., Academic Press, 191–204.